6-2004

Utilizing Near-Field Measurements to Characterize Far-Field Radar Signatures

John R. Watkins

AFIT/GE/ENG/04-24

UTILIZING NEAR-FIELD MEASUREMENTS TO CHARACTERIZE FAR-FIELD RADAR SIGNATURES

THESIS

John R. Watkins
Captain, USAF

AFIT/GE/ENG/04-24

DEPARTMENT OF THE AIR FORCE

AIR UNIVERSITY

AIR FORCE INSTITUTE OF TECHNOLOGY

Wright-Patterson Air Force Base, Ohio

AFIT/GE/ENG/04-24

UTILIZING NEAR-FIELD MEASUREMENTS TO CHARACTERIZE FAR-FIELD RADAR SIGNATURES

THESIS

Presented to the Faculty

Graduate School of Engineering and Management

Air Force Institute of Technology

Air University

Air Education and Training Command

In Partial Fulfillment of the Requirements for the

Degree of Master of Science in Electrical Engineering

John R. Watkins, B.S.E.E.

Captain, USAF

June, 2004

AFIT/GE/ENG/04-24

UTILIZING NEAR-FIELD MEASUREMENTS TO CHARACTERIZE FAR-FIELD RADAR SIGNATURES

THESIS

John R. Watkins, B.S.E.E.

Captain, USAF

Approved:

//signed// Posthumously	
Maj. William D. Wood, PhD. Thesis Advisor	Date
//signed//	
Maj. Todd Hale, PhD. Thesis Advisor	Date
//signed//	
Dr. Michael Havrilla Committee Member	Date
//signed//	
Dr. William Baker Committee Member	Date

Acknowledgements

I am thankful to many people for their motivation and inspiration throughout my academic and professional career. But, first and foremost, I must acknowledge my wife and kids whose love and support become my motivation when self motivation begins to fade. Specifically, my wife has done everything within her power to relieve my home responsibilities allowing me to focus on my education and this project. The sacrifices made by my wife and children during the extended hours spent on this project are greatly appreciated.

I would like to also thank my classmates, instructors, and sponsors for their roles in developing and extending my understanding in the subject matter of this document. From our class, I would like to thank Capt Byran Smith and Lt Donny Powers who took the time to perform peer reviews of my work. I would also extend my appreciation to Maj Todd Hale for becoming my advisor late in the thesis process. His help and advice were instrumental to this projects completion. Finally, I would like to extend my appreciation to my sponsors Tony Kim, William Bechtel, and Carl Conklin for their investment in exposing me to the ongoing efforts associated with the NFFFT topic beyond the academic environment.

John R. Watkins

Table of Contents

Page

List of Figures

Abstract

The increased need for stealth aircraft requires an on-site Far-Field (FF) Radar Cross-Section (RCS) measurement process. Conducting these measurements in on-site Near-Field (NF) monostatic facilities results in significant savings for manufacturers and acquisition programs. However, NF measurements are not directly extended to a FF RCS. Therefore, a large target Near-Field to Far-Field Transformation (NFFFT) is needed for RCS measurements. One approach requires an Inverse Synthetic Aperture Radar (ISAR) process to create accurate scattering maps.

The focus of this work is the development of accurate NF scattering maps generated by a monostatic ISAR process. As a first look, the process is isolated to a simulated environment to avoid the uncontrollable effects of real measurement environments. The simulation begins with a NF Synthetic Target Generator (STG) which approximates a target using scattering centers illuminated by spherical electromagnetic waves to approximating NF scattering. The resulting NF In-phase and Quadrature (IQ) data is used in a 'Trapezoidal' ISAR process to create spatially distorted images that are accurately corrected within the ISAR process resolution using a newly developed NF correction. The resulting spatially accurate ISAR images do not complete the NFFFT. However, accurate scattering maps are essential for process development.

UTILIZING NEAR-FIELD MEASUREMENTS TO CHARACTERIZE FAR-FIELD RADAR SIGNATURES

I. Introduction

1.1 Background

Radar Cross-Section (RCS) is paramount for aircraft survivability in air defense penetration missions. Therefore, aircraft used in these missions must satisfy Far-Field (FF) RCS acceptance requirements during production. The introduction of these requirements increase production cost significantly through FF range time and aircraft transportation to these facilities. However, these manufacturing costs are significantly reduced by having an inexpensive on-site RCS measurement process.

This chapter introduces the background motivation for development of an on-site RCS measurement process. The background establishes and outlines the problem, assumptions, and scope of work provided in this document. Even though the entire RCS measurement process is not covered in this document, a conceptual process outline is provided for characterizing FF RCS using Near-Field (NF) measurements.

The problem associated with this process is RCS and measurement requirements satisfying FF RCS. RCS is an object's characteristic defining its radar detectability. This definition is based on radar and target separation large enough that electromagnetic field propagation is predictable [13]. RCS satisfying this assumption is considered FF RCS. However, satisfying FF RCS requirements make large target FF RCS measurements impractical in compact facilities without illuminating beam correction. Therefore, NF Inverse Synthetic Aperture Radar (ISAR) measurements are necessary for production aircraft. Utilizing these NF measurements a Near-Field to Far-Field Transformation (NFFFT) is used to characterize FF RCS using NF measurements.

Determining full-scale aircraft Far-Field (FF) RCS requires a distance on the order of miles between the radar and target. This requirement alone makes FF facility availability extremely limited and impractical for aircraft manufacturing companies to build. Therefore, production aircraft must be transported to available measurement facilities. Transportation and range time are very costly for manufacturing companies and government acquisition programs. However, Near-Field (NF) measurement exploitation allows for FF RCS characterization in an over-sized warehouse or hangar. When utilizing smaller on-site facilities, aircraft are towed directly from the production line to the measurement facility, significantly decreasing measurement cost.

Inverse Synthetic Aperture Radar (ISAR) is a common method for NFFFT [16, 17]. The ISAR process creates a scattering map and is implemented using different configurations [12, 21]. However, ISAR is usually dependent upon data collected through frequency sweeps along target rotational increments producing a spatial reflective scattering point map [6]. These isolated point scatterers have a combined coherent RCS approximating a larger, more complex, target [13].

ISAR applications for target RCS are defined relative to range type, measurement process, antenna configuration, or any combination thereof. FF measurements provide a direct means for FF RCS determination. These measurements are made satisfying FF distance separation requirements or in compact ranges using an electromagnetic field collimating lens or reflector. However, NF measurements do not directly represent FF RCS. The NF measurements have incomplete electromagnetic field interactions. Therefore, many NF measurement techniques usually involve bistatic or multistatic probe correction. These probes provide complex weights which correct NF measurement electromagnetic field interactions for FF RCS characterization [15, 23]. These methods claim success in different limited applications. However, these methods require additional equipment cost beyond radar and target turntable. Therefore, monostatic ISAR NF measurements in a compact range, the goal of this work, results in significant cost savings for aircraft companies and government acquisition programs.

In order to meet aircraft RCS acceptance, the F/A-22 program office is sponsoring devel-

opment of a technique to compare results with the manufacturer. This contractor currently uses monostatic NF RCS measurements and a noncoherent NFFFT to characterize FF radar signatures utilizing sector averaging. The contractor is reporting success, within a small tolerance, by comparing true FF RCS to NF corrected RCS through sector averaging. Sector averaging is considered risky, since these averaged RCS measurements, taken over a given angular sector, neglect further constructive and destructive interference in FF propagation. Additionally, over an aircraft's angular rotation, RCS may remain relatively consistent or vary greatly within a few sampling degrees. RCS sector averaging accounts for the total energy spread out over an azimuthal sector. However, a spike spread over a few samples and averaged over many samples results in a sector average much lower than the spike. If this spike is not identified, an aircraft's aspect dependent detection range and vulnerability significantly increases. Therefore, a method is needed to coherently predict azimuthal dependent FF RCS using monostatic NF measurements, which would improve FF RCS fidelity. This improvement would account for target aspect dependent RCS by identifying spikes and nulls within the target rotational fidelity.

1.2 Problem Statement

The goal is to develop a monostatic ISAR image using NF measurements which accurately maps scattering center locations and provides the basis for scattering center synthesis and FF RCS characterization. Process success allows manufacturers to measure aircraft FF RCS locally, streamlining acceptance and significantly reducing government and contractor measurement costs. Therefore, The F/A-22 program office is sponsoring the coherent monostatic NFFFT development applicable to this program and possibly other programs having RCS acceptance requirements. A concept for the complete NFFFT process is depicted in Fig. 1.1. However, this document's focus is limited to a spatially accurate NF corrected ISAR image. This process is outlined by the NF STG and NF ISAR components contained in the dark box of Fig. 1.1.

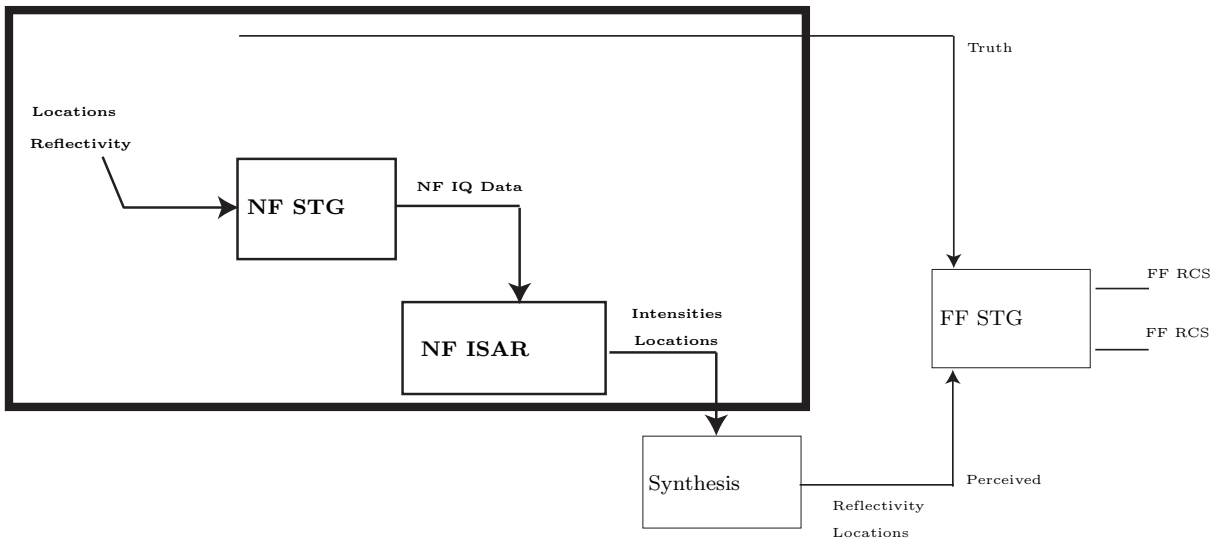

Figure 1.1: The primary focus in this Near-Field to Far-Field Transformation is on developing a spatially accurate NF ISAR image. Therefore, the focus is on the NF STG and ISAR process. The entire process starts with the two ISAR Synthetic Target Generators (STGs) that take real scattering center locations and reflectivities and create FF and NF IQ Data. The FF IQ data is considered truth data. The NF IQ Data is imaged by an ISAR code, mapping maximum intensity spatial locations. These complex intensities extracted by scattering center synthesis provide spatial locations and relative phases. These locations and complex amplitudes are passed through a FF STG producing a FF RCS. This FF RCS is compared to the true FF RCS generated from the real locations.

1.3 Assumptions

The following assumptions are made:

1. A complex target's FF RCS is equivalent to a scattering center group's FF RCS.
2. The illuminating source is a linearly polarized perfect horn radiator and receiver whose line-of-sight (LOS) is aligned with the target's rotation center.
3. The scattering centers are isotropic point scatterers in the horn's FF that do not induce polarization loss.

4. Scattering center shadowing does not occur during target rotation due to a high frequency, Geometric Optics (GO), model.

5. The target is a rigid body excluding scattering center oscillation due to target rotation.

1.4 Scope

The research scope is depicted in Fig. 1.1 and focuses on the following:

1. Design and code a NF synthetic target generator producing NF ISAR IQ data.

2. Design and code a NF corrected ISAR processing routine producing spatially accurate imaging data from the NF IQ data.

1.5 Overview

Implementation of the ISAR process is dependent upon the conceptual background that is presented in the following chapter. In Chapter III these concepts are used to develop simulated measurement and processing environments. The environments and concepts of Chapters II and III are used to establish the monostatic NF ISAR data collection process of Chapter IV using a simulated NF STG that creates IQ data dependent upon the target's rotation, frequency bandwidth, and scattering properties of isotropic point scatterers. The simulation continues in Chapter V where the resulting IQ data is used in a rectangularly based two-dimensional ISAR process to create a scattering center image. The resulting image is spatially distorted due to the NF effects which are approximated by spherical scattering. Therefore, the spatially distorted image is resampled based on a new spherical NF correction technique that resamples image locations to within the ISAR process resolution. This technique results in a spatially accurate image of target reflective points and is the basis for the full NFFFT to characterize FF RCS using NF measurements.

II. Literature Review

An inexpensive Far-Field (FF) Radar Cross Section (RCS) method utilizes monostatic Inverse Synthetic Aperture Radar (ISAR) measurements. In the Near-Field (NF), this process produces an image defining spatially dependent target scattering points. This scattering map is used to predict large target FF RCS through the scattering group's synthetic FF illumination. This FF technique's exploitation in a NF measurement environment eliminates unnecessary radar beam collimators, probes, or multiple antennas providing field correction. Avoiding additional cost for hardware or target transportation to a FF facility results in significant savings for manufacturers and acquisition programs. Therefore, an RCS and ISAR foundation is needed to create an accurate synthetic NF scattering center map.

This chapter provides the foundation for RCS and ISAR by reviewing previously published works in these two areas. The review begins with a description of RCS, RCS measurement, and defining FF RCS. Additionally, this chapter outlines the ISAR process in terms of downrange and cross-range imaging and image focusing. RCS and ISAR comprise this chapter's focus. However, a brief introduction to scattering center extraction is also provided to justify this approach and the use of scattering centers for target approximation.

2.1 Radar Cross-Section

RCS is paramount in determining an aircraft's survivability against air defense systems. RCS describes scattered energy from an object illuminated by an incident electromagnetic wave. This energy is responsible for determining an aircraft's detection distance. Therefore, aircraft having air defense penetration roles require RCS production acceptance parameters. This section provides a brief introduction to RCS, RCS measurement, and FF RCS.

RCS is defined by a known metal object's projected area reflecting an equivalent amount of energy [13]. A formal definition of RCS describes the radar signature at the target's location.

Therefore, the scattered field propagation decay is not considered. This definition is given as [13]

$$\sigma = \lim_{r\to\infty} 4\pi r^2 \frac{\left|\vec{p}_r \cdot \vec{E}^s\right|^2}{\left|\vec{E}^i\right|^2}, \tag{2.1}$$

where r is radar to target distance and is academically corrected by letting the range approach infinity to eliminate the range dependence of RCS [13]. Additionally, $\vec{p}_r$ is the receiving antenna polarization, and scattered and incident electric fields are, $\vec{E}^s$ and $\vec{E}^i$, respectively. Since electric fields are measured in units proportional to $\frac{V}{m}$, RCS is proportional to the scattered and incident field's power density ratio. Propagation loss, $\frac{1}{4\pi r^2}$, is based upon conservation of energy and the FF approximation described in Appendix B. This decay describes the electromagnetic field's uniform power density distribution over a spherical wave front, decaying as propagation radius increases. However, if propagated energy described by Eqn. (2.1) had no polarization mismatches between antenna and scattered wave then RCS is represented by

$$\sigma = \lim_{r\to\infty} 4\pi r^2 \frac{\left|\vec{E}^s\right|^2}{\left|\vec{E}^i\right|^2} . \tag{2.2}$$

This equation implies RCS measurement is dependent upon knowing the radar to target range, incident field strength on the target, and the received scattered field strength. However, unless probes are used the incident field strength on the target is unknown and the return signal must be processed to extract the RCS. Therefore, the next section provides background on radar signal processing, RCS measurement, and what is meant by FF.

2.1.1 Radar Mixing and Filtering Process. The signal reflected from a target is a scaled and delayed transmitted signal's replica. The signal scaling results from many factors, such as propagation decay, target reflectivity, and antenna gain. The signal delay is based on a zero phase reference established at the target's rotation center. The signal's mixing and filtering process is

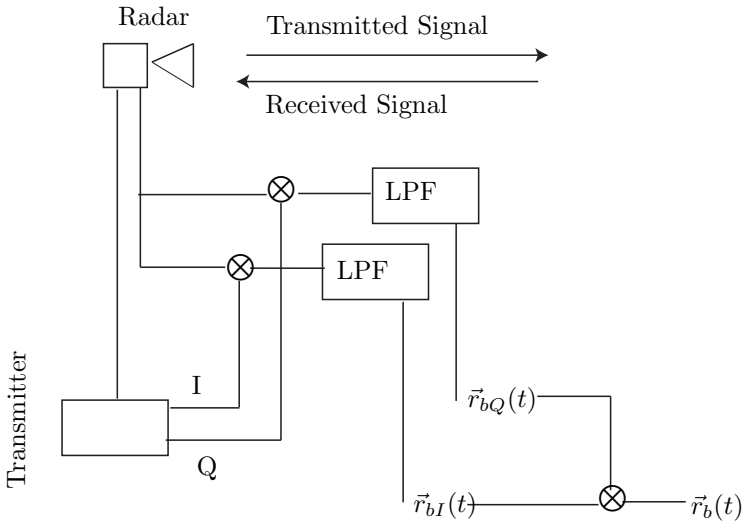

Figure 2.1: A radar transmits a signal and receives that signal reflected from a target. The transmitter also separately transmits In-phase and Quadrature, (IQ), reference signals to separate mixers and are mixed with the return signal. This results in a component at The twice the carrier frequency and one at baseband. To analyze the baseband signal, the baseband signal is retrieved by low pass filtering. The return IQ signals are then recombined to form the full return signal.

detailed in Appendix D. This process is summed up by Fig. 2.1, where the received signal is mixed with the transmitted signal's In-phase and Quadrature, (IQ), terms separately. However, mixing results in sum and difference terms, where sum terms are centered on twice the carrier frequency. Therefore, when these signals are low pass filtered, only the scaled IQ terms with the propagation delay relative to the phase reference remain. These signals are then recombined to form IQ data which is processed to provide RCS. However, the IQ data collection method determines how this data is processed to establish an RCS.

2.1.2 RCS Measurement. There are many ways to measure RCS [13, 15, 23], but most measurements employ a calibration method. RCS measurement in a monostatic indoor compact range uses a single antenna for transmitting and receiving radar signals. A target's RCS is referenced to a specific frequency and target aspect. Therefore, if the radar is stationary, measurement

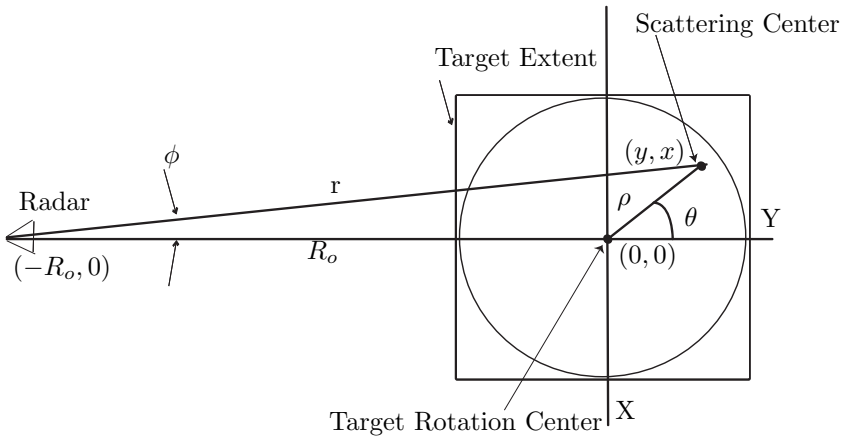

Figure 2.2: A simple target/radar relationship within a measurement facility. The target's rotation center is located downrange from the radar and is the measurement spatial center. When the target is rotated, its largest dimension determines its crossrange extent X and its downrange extent Y. A target's reflective point (scattering center) is a distance from rotation center ρ and is the scattering center's rotation radius. The scattering center's azimuthal rotation is described by θ and its aspect to the radar is described by ϕ.

facilities have a target mounting system that allows for target rotation. This geometry is depicted in Fig. 2.2, where the antenna to mount and target scattering center (reflection point) distances are R_o and r. This scattering center range is dependent upon its spatial location and aspect angle ϕ, referenced to the radar. Target rotation center is the spatial domain center, radar alignment center, and propagation phase reference described in Appendix A. This reference is established through calibration measurement techniques.

Background subtraction is a calibration method used to establish a propagation phase reference, normalize RCS, and decrease extraneous background RCS contributions. A calibration

target, with known RCS, is measured at a radar to mount distance R_o providing a phase reference and normalizing RCS. This process is described by modifying Eqn. (2.2),

$$\sigma_{tgt} = \frac{\left|\vec{E}^s_{tgt}\right|^2}{\left|\vec{E}^s_{cal}\right|^2}\sigma_{cal} \ , \tag{2.3}$$

where $\vec{E}^s_{tgt}$ and $\vec{E}^s_{cal}$ are target and calibration object's electric fields, respectively, and σ_{cal} is a known calibration target RCS. However, these measurements include contributions from mounting hardware. These contributions are minimized by measuring the mounting structure and background RCS contributions and subtracting them from the measured target RCS,

$$\sigma_{tgt} = \frac{\left|\vec{E}^s_{tgt} - \vec{E}^s_{bkg}\right|^2}{\left|\vec{E}^s_{cal} - \vec{E}^s_{cbk}\right|^2}\sigma_{cal} \ , \tag{2.4}$$

where $\vec{E}^s_{tgt}$, $\vec{E}^s_{bkg}$, $\vec{E}^s_{cal}$, $\vec{E}^s_{cbk}$, are target, target's background, calibration target, and calibration target's background scattered electric fields, respectively. *This process requires two separate background measurements because target and calibration target mounting structures may be different.* Equation (2.4) appears to eliminate all structural contributions associated with the measurement environment and provide a target only measurement. Unfortunately, the interactions between these structures are not removed and still provide contributions. These contribution in most cases are considered minimal, however, work continues in this area to eliminate or characterize these interactions and their contribution in RCS measurements.

Measurement structural interactions are unwanted phenomena in RCS measurements. However, target structural interactions are necessary to determine RCS. Since RCS is an essential part of radar detection and detection is conducted at distances on the order of miles, the scattered fields must propagate a distance which allows for complete interaction. The distance for this propagation characteristic to exist is called the FF. Since compact NF ranges do not satisfy the FF

requirement, the data is not directly processed into a FF RCS and needs a Near-Field to Far-Field Transformation (NFFFT) [7, 14].

2.1.3 Far-Field RCS Requirement. The development for Eqn. (2.4) is based on FF approximations. However, compact ranges are too small to accommodate the FF distances required to measure large target RCS. Large target implies RCS measurement distance r and largest target dimension d do not satisfy the minimum FF conditions of Appendix B described by

$$r = 2\frac{d^2}{\lambda}, \tag{2.5}$$

where λ is wavelength and Eqn. (2.5) is derived based upon a $\frac{\pi}{8}$ cross-range extent phase tolerance. For example, a 15 m target illuminated by a radar operating at 6 GHz frequency, requires a FF RCS measurement distance, Eqn. (2.5), $r = 9000$ m. Therefore, large targets are measured in outdoor FF ranges or indoor ranges with NF correction such as collimators or multistatic antenna arrangements [4, 13, 19]. However, FF measurement facilities are becoming cheaper and more available through continuing effort focused on monostatic FF RCS approximations using NF ISAR measurement and imaging techniques [8, 10, 20].

This section provided a review of RCS, RCS measurements, and identified FF criteria. RCS is referenced to a specific frequency and azimuth. However, ISAR imaging uses impulse responses dependent upon the doppler shifts in both frequency and azimuth. Therefore, ISAR techniques depend upon multiple iterations of RCS measurements.

2.2 Inverse Synthetic Aperture Radar

This section identifies how the ISAR process utilizes RCS measurements to create spatial images. As an introduction to ISAR, this section defines the ISAR process, identifies its use in downrange and cross-range imaging, and explains how a rectangular DFT is used in image focusing.

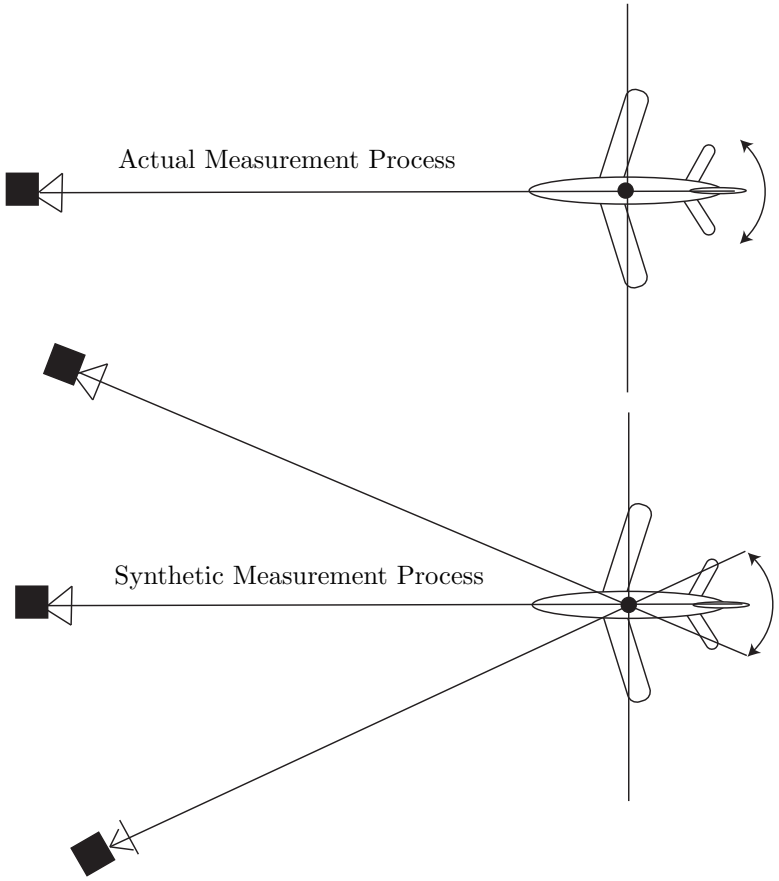

Figure 2.3: The ISAR process uses frequency sweeps along azimuthal increments of target rotation. However, a signal processing equivalent results from frequency sweeps along azimuthal increments in radar rotation around the target. This process synthetically produces an aperture equivalent to the radar's synthetic azimuthal translation. The incremental steps synthesize array elements which are aligned with target rotation center.

The images created are dependent upon the two-dimensional impulse response of multiple iterations of frequency/azimuth RCS measurements.

2.2.1 Synthesizing an Array. ISAR techniques are similar to Synthetic Aperture Radar (SAR) techniques that depend upon radar motion to synthesize an array [12, 21]. ISAR has a static radar and utilizes target rotation to generate an equivalent synthetic array. Therefore, a monostatic radar is visualized as an array element. Figure 2.3 shows that the ISAR process synthetically generates an array through frequency sweeps at incremental target rotations. Each

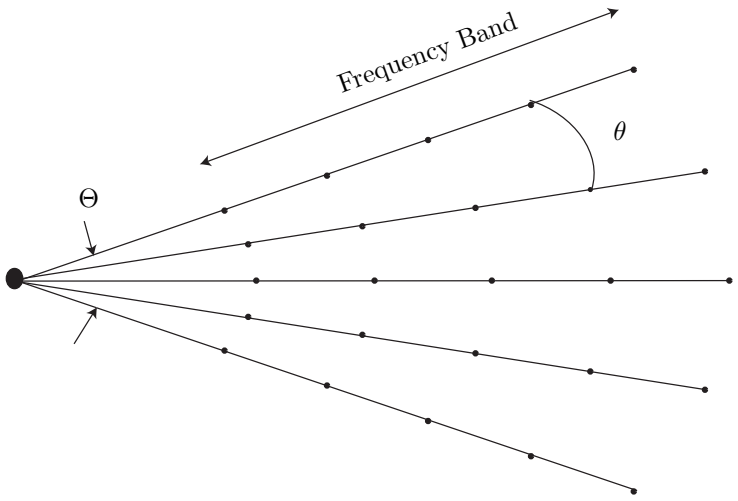

Figure 2.4: ISAR data is collected by recording energy returns from frequency sweeps over a target's azimuthal rotation Θ in azimuthal increments θ. This rotation creates polar formatted data referenced to the target's rotation center.

azimuthal 'snapshot' is, synthetically, a separate array element separated on an arc by a target's rotational increment. The collection process results in the two-dimensional polar formatted data defined by azimuth and frequency shown in Fig 2.4.

2.2.2 Downrange Imaging. Downrange imaging refers to radar alignment with the target's rotation center aligned along the Y axis as shown in Fig. 2.5. The downrange imaging goal is to distinguish between multiple targets or multiple target features separated in this direction. A target's or its features' range is determined temporally by

$$r = \frac{ct}{2}, \tag{2.6}$$

where c is the speed of light and t accounts for round trip propagation time. Appendix A shows that the minimum resolvable scatterer separation distance is determined by the return signal's Fourier transform,

$$s_b(t) = Ab[t - \tau_o - \tau(y)]\,\mathbf{Re}\left\{g(y)\,e^{j\omega_o[t-\tau_o-\tau(y)]}\right\}, \tag{2.7}$$

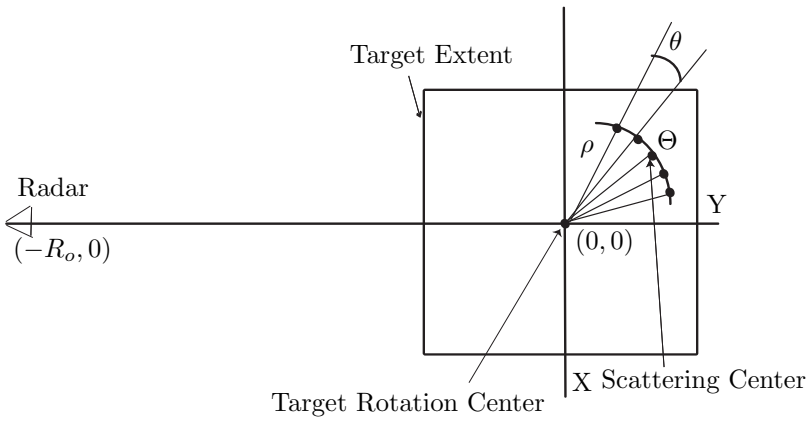

Figure 2.5: The target's rotational geometry is described by isolating a single target reflection point, scattering center. This point rotates through an azimuth Θ at azimuthal increments θ. Its rotation radius is determined by its spatial distance from the target's rotation center.

where A is a scaling factor, **Re** represents the real signal component, and ω_o is carrier frequency. Additionally, the geometry of Fig. 2.6 shows that the propagation time to the target rotation center and downrange locations are τ_o and $\tau\left(y\right) = \frac{2y}{c}$, respectively. These times are used to define the signals burst function $b\left[t - \tau_o - \tau\left(y\right)\right]$. The target reflectivity $g(y)$ is a real or complex value whose magnitude and phase range from $0 - 1$ and $0° - 180°$, respectively. This function's impulse response identifies scattering center downrange location within resolution limits. Since multiplication in time domain results in convolution in frequency domain [5], the burst function effective pulse width τ_e convolved with the signal determines minimum resolvable temporal separation between targets. Therefore, targets separated by the effective pulse width are separable in a downrange distance

$$\Delta y = \frac{c\tau_e}{2}\,, \tag{2.8}$$

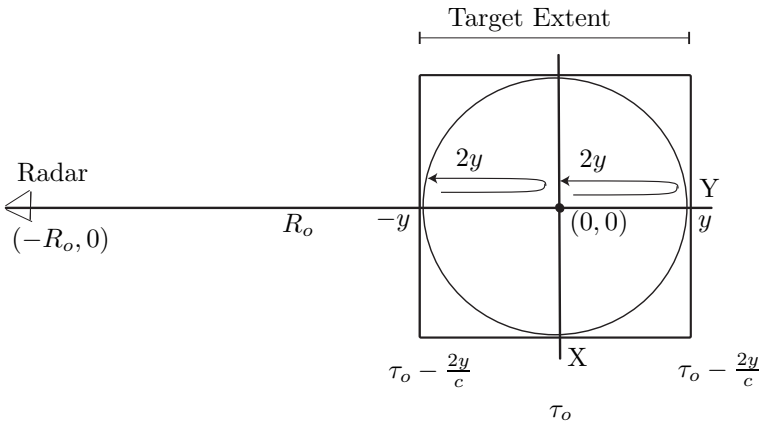

Figure 2.6: Downrange spatial extent is referenced to measurement area center. Since the radar is monstatic, signals must traverse radar to target path twice. Therefore, downrange extents are defined based on round trip propagation referenced to measurement area center.

or in terms of effective bandwidth B_{eff},

$$\Delta y = \frac{c}{2B_e} , \tag{2.9}$$

where Δy is the downrange resolution [24]. If targets meeting these requirements are separable in the frequency sweep's Fourier transform, where azimuth is held constant, the one-dimensional impulse response compresses energy spread across bandwidth into a signal whose main response width is equivalent to down range resolution defined by Eqn. (2.9). Therefore, targets separated by this spatial resolution are dimensionally imaged separately in the downrange dimension. Separation requirements also limit cross-range resolution. However, cross-range imaging depends upon doppler change associated with target azimuthal rotation.

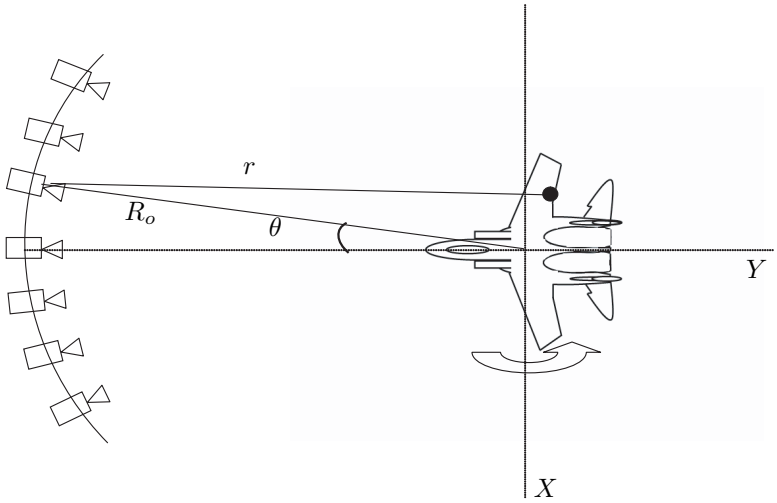

Figure 2.7: A target's scattering point is imaged as if the radar was rotating around the target. Therefore, a frequency sweep at each target aspect increment, θ, has a different relative phase due to change in propagation distance, r. Therefore, different phases, relative to each aspect increment, are equivalent to doppler changes.

2.2.3 Cross-range Imaging. There are two benefits for sampling over azimuthal increments. First, Appendix E shows that synthetically increasing the array size results in increased radar gain. Additionally, azimuthal sampling establishes a doppler basis for cross-range imaging by rotating the target through an azimuth Θ and sampling frequency for the same reflection point in different locations. The received signal has a different phase for each target azimuthal sample, which is equivalent to doppler changes. Figure 2.7 shows the geometry for the DFT. The azimuthal sampling during target rotation results in doppler changes proportional to the temporal difference in propagation distance. Cross-range imaging is accomplished by transforming this time domain data into frequency doppler data as shown in Section 2.2.1. One method utilizes a Discrete Fourier Transform (DFT), which coherently sums all target scatterers [21]. Since the radar's beam

is focused on target rotation center and imaged over its surface, a function is required determining phase corrections for coherent signal summation. This function is determined by fixing a center frequency f_o and rotating the target through a range $\frac{-\Theta}{2} \leq 0 \leq \frac{\Theta}{2}$ where Θ is the synthetic aperture extent. A scattered field $E^s(\theta, f)$ summation, where θ represents individual sampling steps in Θ, results in

$$G(x,y) = \sum_{\theta} E^s(\theta)\, e^{j2kr(\theta,x,y)} . \tag{2.10}$$

Equation (2.10) describes coherent field summation, where $2r$ represents round trip distance between the radar and scatterer. This distance r is dependent upon the scatterer's location (x, y) at each azimuthal increment θ through the target's rotation. The wave number k describes propagation and is related to wavelength by $k = \frac{2\pi}{\lambda}$. Equation (2.10) is referred to as a beam steering function because it represents electric field sampling at arbitrary target points, while maintaining radar alignment with target rotation center [21]. Therefore, the geometry of Fig. 2.5 shows the target scattering center positions are described by

$$r(\theta,x,y) = R_o\sqrt{1+\frac{2(y\cos\theta - x\sin\theta)}{R_o}+\frac{x^2+y^2}{R_o^2}} , \tag{2.11}$$

where x and y represent scattering center spatial coordinates referenced to the target rotation center and R_o is the radar to target rotation center distance. Inserting Eqn. (2.11) into Eqn. (2.10), the steered synthetic aperture response function becomes

$$G(x,y) = \sum_{\theta} E^s(\theta)\, e^{j\frac{4\pi}{\lambda}R_o\sqrt{1+\frac{2(ycos\theta - xsin\theta)}{R_o}+\frac{x^2+y^2}{R_o^2}}} , \tag{2.12}$$

which is the focused beam steer equation. Some approximations are made to Eqn. (2.12) which simplify computational analysis. Assuming imaging distance $R_o \gg d$ where d is the largest target dimension, then small angle approximations can be made where $\sin\theta = \theta$ and $\cos\theta = 1$.

Additionally, the FF assumption $R_o \gg (x \text{ or } y)$ implies higher order terms $\propto \frac{1}{R_o^n}$ approach 0 for $n > 1$, resulting in

$$G(x,y) = \sum_{\theta} E^s(\theta) e^{j\frac{4\pi}{\lambda}R_o\sqrt{1+\frac{2(y-x\theta)}{R_o}}} . \tag{2.13}$$

Further reduction is made by recognizing the exponential square root term is approximated by a binomial expansion[1]. Applying far-field approximations reduces the exponent to $R_o + y - x\theta$. Removing terms not a function of θ from the summation, Eqn. (2.13) is simplified to

$$G(x,y) = e^{j\frac{4\pi}{\lambda}(R_o+y)}\sum_{\theta} E^s(\theta) e^{-j\frac{4\pi}{\lambda}x\theta} . \tag{2.14}$$

Since cross-range location is dependent on phase shift or doppler variation in the transform, the exponent preceding the sum is dropped and magnitude is expressed as

$$G(x,y) = \sum_{\theta} E^s(\theta) e^{-j\frac{4\pi}{\lambda}x\theta} . \tag{2.15}$$

If the function is sampled over N equally distributed angles in the interval $-\frac{\Theta}{2} \leq 0 \leq \frac{\Theta}{2}$, then $\theta_n = -\frac{\Theta}{2} + n\theta$, where $\theta = \frac{\Theta}{N-1}$, $n = 0, ..., N-1$, and Eqn. (2.15) becomes

$$G(x,y) = \sum_{n=0}^{N-1} E^s(\theta) e^{-j\frac{4\pi}{\lambda}x\theta} . \tag{2.16}$$

The cross-range resolution is established by recalling the DFT pair for sampled signals[2], where sampling intervals are given by $\Omega = \frac{2\pi}{NT}$ and T in the representative domains [22]. Letting $T = \theta$ and $\Omega = 2k_x$, then Eqn. (2.16) is in DFT form. Therefore, over this function's sampling interval

$$2k_x = n\Omega \tag{2.17}$$

[1] $(1+x)^m = 1 + mx + m(m-1)\frac{x^2}{2!} + m(m-1)(m-2)\frac{x^3}{3!} + ...$

[2] $F(n\Omega) = \sum_{m=0}^{N-1} f(mT) e^{-jTmn\Omega}$ and $f(mT) = \frac{1}{N}\sum_{n=0}^{N-1} f(nT) e^{+jTmn\Omega}$

cross-range resolution is defined as

$$x_n = \frac{\lambda}{2\Theta} , \tag{2.18}$$

where $\Theta = N\theta$ is the total aperture size. Therefore, an increase in resolution requires a decrease in center frequency or an increase in azimuth for data collection. *Frequency referenced in cross-range resolution through λ is the center frequency.*

The previous sections establish the concepts for establishing a synthetic array and its use in downrange and cross-range imaging. However, the direct rectangular DFT application to polar formatted frequency/azimuth data results in an unfocused image. Figure 2.8 shows that the polar formatted data represents the data collected with a focused beam. However, in order to use a rectangular DFT on polar formatted data, the measurement distance must approach infinity to make the small angle and plane wave approximations. These approximations are necessary to accurately form the rectangular sample grid of Fig. 2.8. Therefore, rectangular DFT application requires the polar formatted data to be uniformly resampled onto a rectangular grid.

2.3 Trapezoidal or "Keystone": Image Focusing Method [12, 21]

The previous section outlines the basic ISAR concepts. This section provides the Trapezoidal method of image focusing. Image focusing is shown to have great impact on determining scattering center spatial locations within an image.

As discussed in Section 2.2.3, radar data is collected and processed in frequency vs. azimuth polar format and image data is desired in a downrange vs. cross-range rectangular format. A desired DFT transform pair from frequency/azimuth to a rectangular equivalent domain, k-space, is based on the kernel,

$$\vec{r}(\theta, x, y) = \vec{k}_x + \vec{k}_y . \tag{2.19}$$

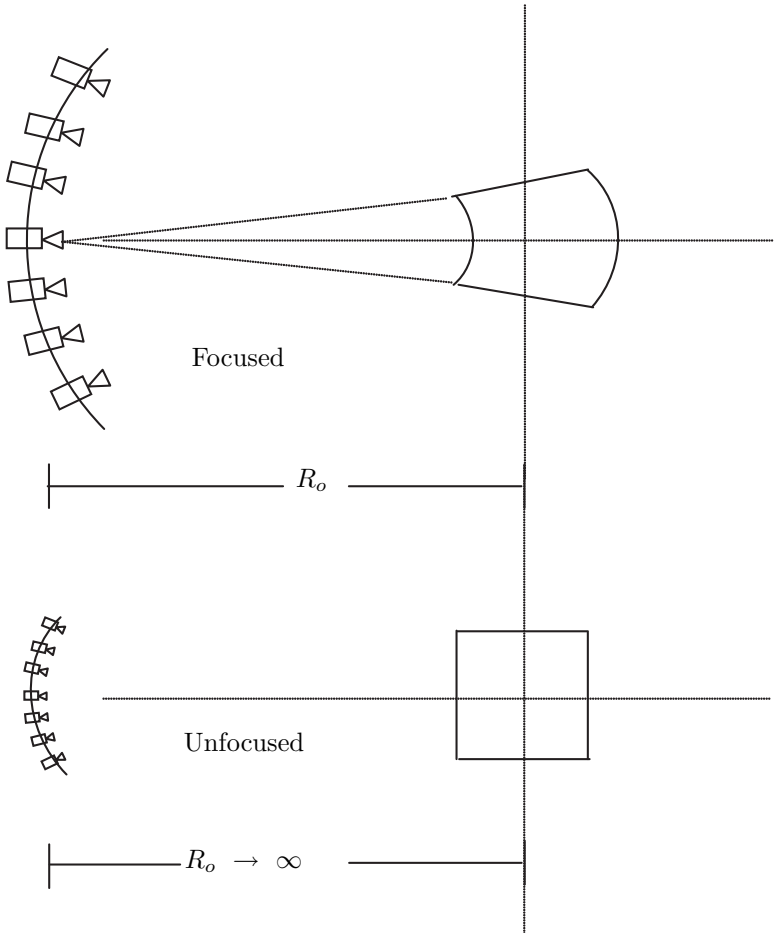

Figure 2.8: The polar formatted ISAR data represents a focused beam. However, rectangular DFT application to polar formatted data requires an infinite radar to target distance where a plane wave and small angle approximation are accurate. This application would result in an unfocused image. Therefore, polar formatted data requires interpolation onto a uniformly sampled rectangular grid.

• *Raw*

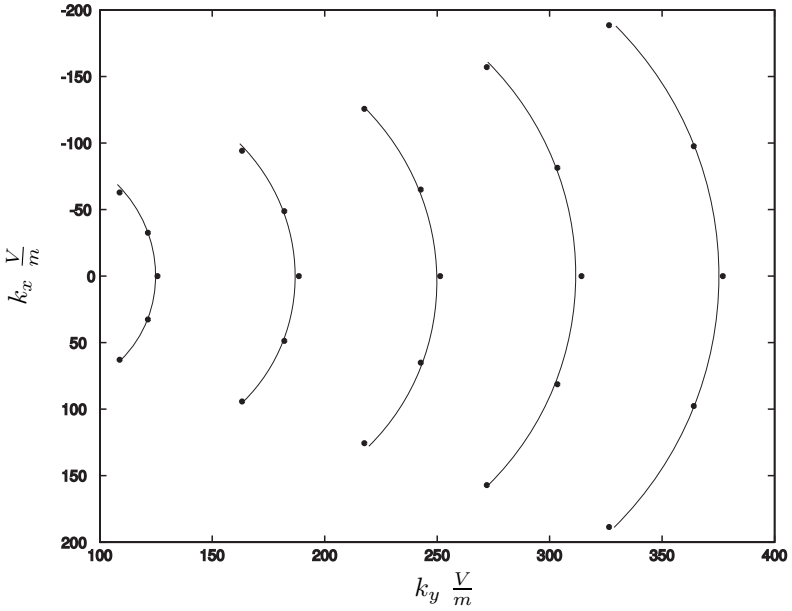

Figure 2.9: The cartesian converted frequency/azimuth data forms a 'keystone' shape, where the curved lines represent lines of constant frequency through a rotational azimuth. The polar to cartesian conversion to k_x and k_y values results in nonuniformly sampled data in both dimensions. The rectangular DFT requires uniform rectangular sampling in both dimensions.

Equation (2.19) describes a relationship between frequency/azimuth measurement space and its propagation equivalent components. The propagation vectors are rewritten as $\vec{k}x = k_x\hat{x}$ and $\vec{k}_y = k_y\hat{y}$, where k_x and k_y represent propagation magnitudes in cartesian directions $\hat{x}$ and $\hat{y}$, respectively. Additionally, wave number is related to frequency f by $k = \frac{2\pi f}{c}$ and frequency is related to wavelength λ by $f = \frac{c}{\lambda}$. Using these relationships, Eqn. (2.19) is rewritten as

$$\vec{r} = \frac{2\pi f}{c}\sin(\theta)\,\vec{x} + \frac{2\pi f}{c}\cos(\theta)\,\vec{y}\,. \tag{2.20}$$

Polar formatted frequency and azimuth data is converted to cartesian coordinates using Eqn. (2.20). Plotting this raw data in Fig. 2.9 shows it has a keystone shape. Applying the rectangular DFT of Eqn. (2.10) directly to polar formatted data results in an unfocused image as shown in Fig. 2.10. Therefore, polar data must be interpolated onto a uniformly sampled rectan-

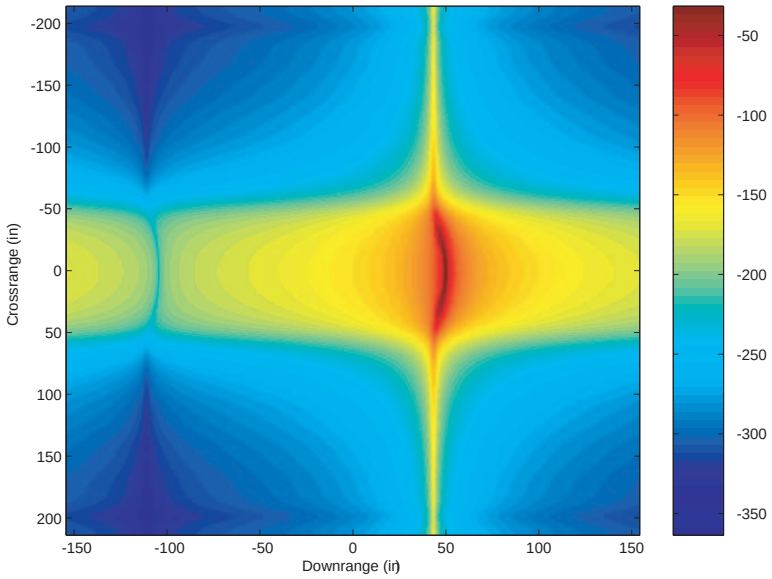

Figure 2.10: Direct rectangular DFT application to polar formatted data results in an unfocused image. A single isotropic point scatterer's location, 40" downrange, is smeared in cross-range. This smear has significant impact in determining scattering center location.

gular grid.

This interpolation is accomplished in two steps. The raw data is interpolated in the k_y dimension onto a trapezoidal grid representing uniformly sampled data in the k_y dimension and nonuniformly sampled data in the k_x dimension as seen in Fig. 2.11. This uniformly sampled k_y trapezoidal data is then interpolated onto a rectangular grid which is uniformly sampled in k_y and k_x as seen in Fig. 2.12. This uniformly sampled rectangular grid defines a raw data subset and DFT application to this data results in a focused image. Figure 2.13 shows a single isotropic scattering center located 40" downrange whose image is focused compared to Fig. 2.10. This comparison illustrates beam focusing and its significance in deciphering scattering center locations.

Section 2.1 through Section 2.3 established the basic concepts relative to ISAR imaging and the impact of a spatially accurate image in determining scattering point locations. This spatially accurate image is the foundation for scattering center mapping and its use in a NFFFT to characterize FF signatures.

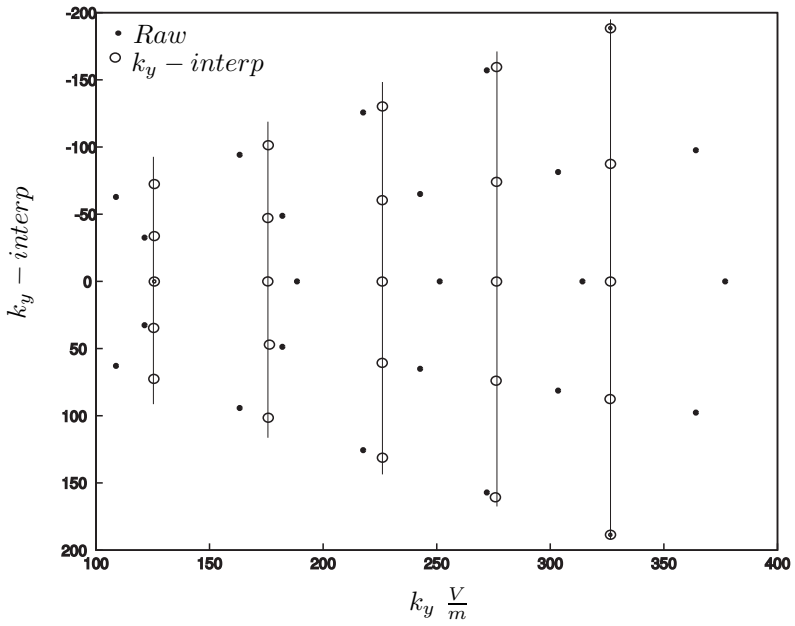

Figure 2.11: The 'keystone' cartesian converted frequency/azimuth data is interpolated onto a trapezoidal grid, uniformly sampled in k_y. However, the data is nonuniformly sampled in k_x. The rectangular DFT requires uniform rectangular sampling in both dimensions.

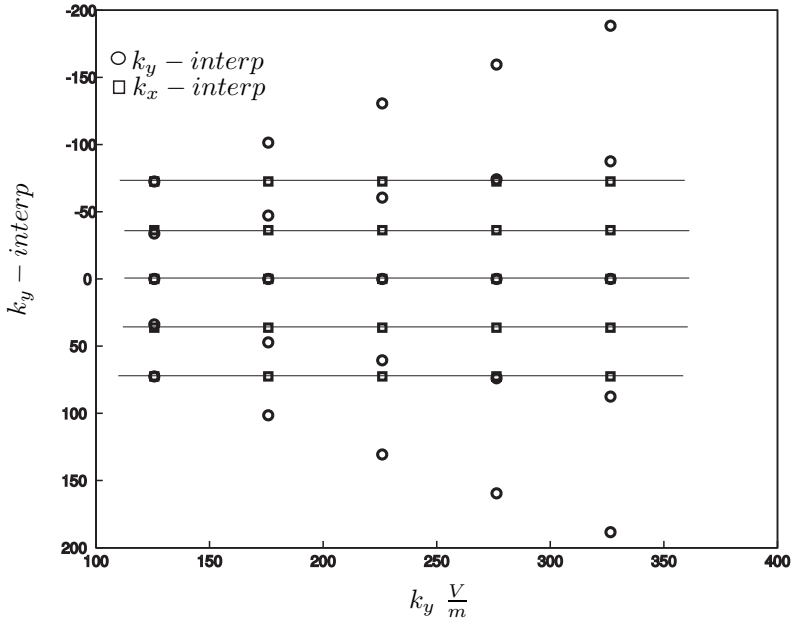

Figure 2.12: The k_y uniformly sampled trapezoidal data is interpolated onto a rectangular grid, uniformly sampled in k_x. This interpolation results in a uniformly sampled rectangular grid completely inscribed in the original keystone data. This uniformly sampled rectangular grid satisfies the rectangular DFT requirement.

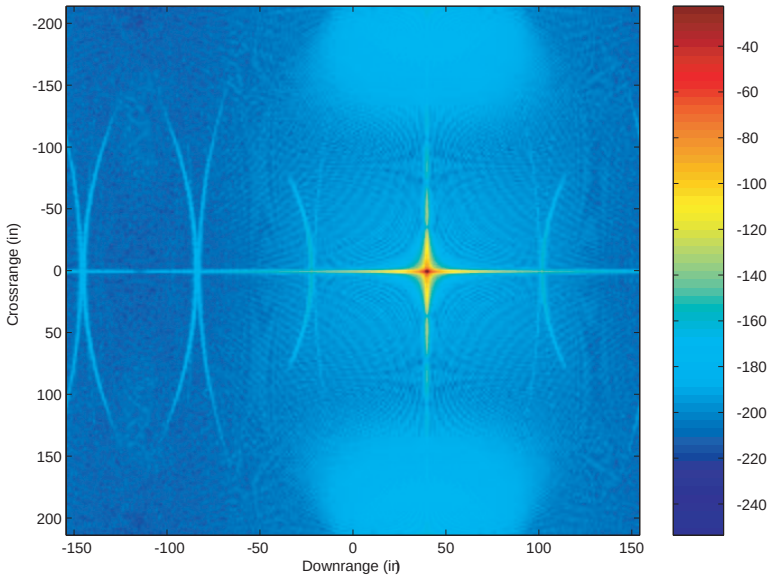

Figure 2.13: Interpolating 'keystone' data to a uniformly sampled rectangular grid before DFT application results in a focused beam. A single isotropic point scatterer's location, 40" downrange, is easily determined within image resolution limits.

2.4 Scattering Center Extraction

Even though scattering center extraction is not performed in this work, its role in the NFFFT of Fig. 1.1 provides the motivation for developing a spatially accurate ISAR image. Utilizing a target's scattering characteristics from an ISAR image establishes an environment to characterize FF RCS using NF measurements. This section utilizes the characteristics associated with ISAR imaging to identify the necessity for accurate scattering center images.

The ISAR image has many applications in Automatic Target Recognition (ATR), RCS prediction, and RCS reduction [9, 12, 21]. A key feature for these applications is ISAR's capability to identify target reflective features. When utilizing high frequency measurements, where high frequency implies wavelength is much smaller than target scattering points, Fig. 2.14 shows that these points or scattering centers represent target reflective features contributing to the measured signal return [13, 26]. Therefore, target total returned power is the scattering center's reflected

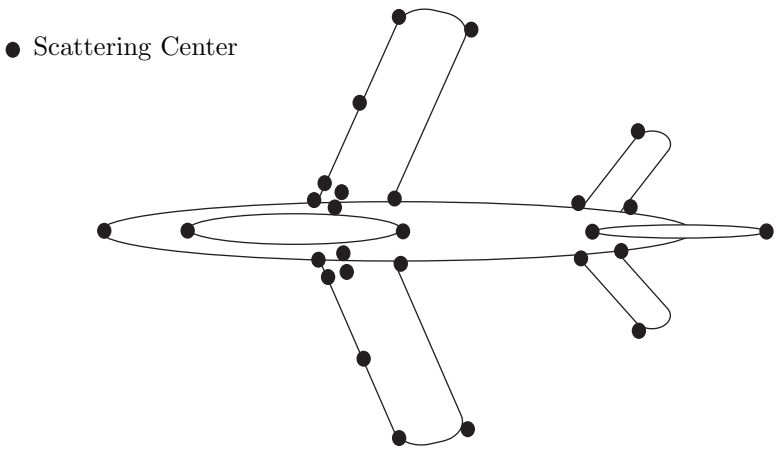

Figure 2.14: A complex target such as an aircraft, tank, or ship can be approximated by a scattering center group when the combined scattering center RCS is equivalent to the complex target RCS at all representative aspects.

power sum,

$$\sigma_{tgt} = \lim_{r\to\infty} 4\pi r^2 \sum_{j=1}^{n} \frac{\left|\vec{E}_j^s\right|^2}{\left|\vec{E}_j^i\right|^2}, \tag{2.21}$$

where r is radar to the scattering center distance, n is the scattering center quantity, and $\vec{E}_j^s$ and $\vec{E}_j^i$ are scattering center scattered and incident electric fields, respectively.

It is scattering center extraction that makes ISAR useful in many applications. These points represent DFT transformed peak impulse response magnitudes. However, since these impulses result from a DFT transform applied to a finite data set, sidelobes are created resulting from the transform's sinc function. These sidelobes are typically below local maxima defined by scattering centers producing the sidelobes. However, depending upon phase variations between multiple scatterers these sidelobes add constructively or destructively with other sidelobes or scattering centers.

These interactions can cause speckle, a false scattering center, or scattering center degradation. Speckle results from interactions between scattering center mainlobes and sidelobes. When a sidelobe is phase shifted with respect to the scattering center peak, it degrades the peak magnitude and adds to its sidelobes creating an image divided into multiple smaller scatterers that are one

large scatterer. Speckle is different from a false target in that a false target is caused from a multiple in phase sidelobe summation, resulting in a magnitude on the same order as scattering centers. Also, multiple sidelobe phase alignment interferes destructively with actual scattering centers and degrades response magnitudes toward the noise floor, eliminating the scattering center image. Depending upon target complexity, an ISAR image's scattering center mapping is the combination of sidelobe and scattering center interactions and rarely are magnitudes purely resultant from an individual scatterer. Therefore, in order to remove scattering centers, sidelobe effects must also be eliminated or targets are falsely represented by these interactions.

Many scattering center extraction techniques are used to predict RCS from ISAR images [11, 17, 18]. These methods are based on establishing scattering center spatial and/or temporal distributions and projecting them from a reference point out in the original propagation direction to acquire a Far-Field RCS. One method, 'CLEAN', eliminates false targets by extracting scattering centers one at a time starting with the maximum contributor [3,25]. This process is used to improve imaging by eliminating speckle in ISAR images. The primary assumption is that maximum contributors are never purely sidelobe interactions. Then the maximum contributor is removed from the image along with its sidelobes, leaving the next strongest scatterer. This process is repeated until the resulting image has a maximum magnitude equal to or below a user defined threshold. The relative scattering center locations are retained upon removal and a scattering center mapping is created. The image is then regenerated by only contributions from scattering centers and removing sidelobes and interactions. Isolating these scattering centers and identifying appropriate weights establishes necessary relationships to perform a FF planar illumination on a specified group and determining FF RCS from the NF scattering. Therefore, synthesis provides a process to extract scattering centers from an accurately corrected NF scattering ISAR image.

2.5 Summary

This Chapter provides the conceptual foundation defining RCS and its dependence on FF measurements. Since the measurements are not practical in a compact facility a NFFFT is needed to characterize FF RCS using NF measurements. Even though the entire NFFFT process is not covered in this document, the conceptual layout of Fig. 1.1 defines the necessity for a spatially accurate ISAR image and its role in characterizing FF RCS.

The concepts presented in this chapter establish the basis for understanding RCS and ISAR to establish the measurement geometry of Chapter III. This geometry is used in the NF ISAR Synthetic Target Generator and NF ISAR process of Chapters IV and V, respectively, to generate spatially accurate images.

III. Near-Field Radar Environment

Inverse Synthetic Aperture Radar (ISAR) monostatic Near-Field (NF) measurement application is the basis for approximating a large target's Radar Cross-Section (RCS) using a scattering center group. In a real measurement environment, limiting the ISAR measurement to a monostatic NF environment eliminates unnecessary collimators, probes, and additional antennas. Synthetically, this process uses a NF ISAR Synthetic Target Generator (STG) to create NF ISAR In-phase and Quadrature (IQ) data. The NF ISAR environment is defined by the physical ISAR measurement geometry and the electromagnetic characteristics. Using a synthetic environment simplifies the problem by minimizing or eliminating undesired signal contributions.

This chapter establishes the specific measurement geometry supporting the NF STG and NF ISAR process of Chapters IV and V. This measurement geometry is dependent upon the physical limitations defined by the measurement process' aperture, desired resolution, and target size. Additionally, these physical parameters invoke limitations on the ISAR environment defined by approximations in the target and scattering characteristics. As a first look, these geometries are developed in a simulated environment that allows for the exclusion of uncontrollable effects associated with a real measurement environment.

3.1 Synthetic Process

This section is a brief introduction to identify the simulated environment. Real ISAR measurement environments have noise contributions from multipath propagation and hardware. To avoid extraneous contributions, simplify the problem, and as a first step in creating the synthesis environment, a purely synthetic approach is taken. This approach focuses on the NF STG and the NF ISAR process of Fig. 3.1.

The measurement geometry is established by the NF ISAR STG. This simulation includes physical parameters, target definition, and a NF ISAR radar simulation to generate the complex

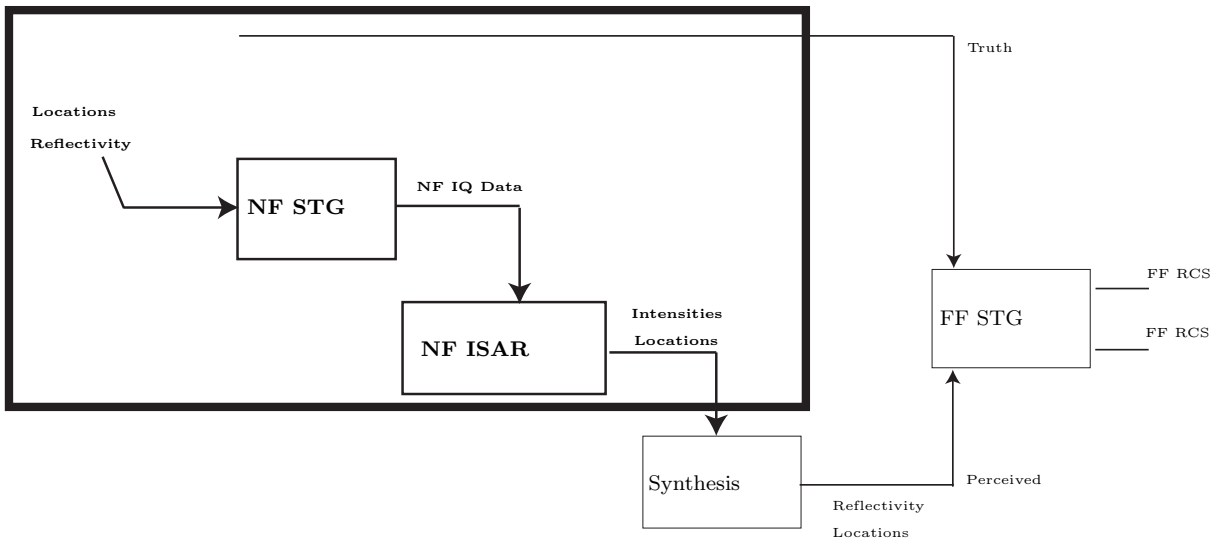

Figure 3.1: The primary focus in this Near-Field to Far-Field Transformation is on developing a spatially accurate NF ISAR image. This focuses on the NF STG and ISAR process. The entire process is describe by starting with the two ISAR Synthetic Target Generators (STGs) that take real scattering center locations and reflectivities and create FF and NF IQ Data. The FF IQ data is considered truth data. The NF IQ Data is imaged by an ISAR code, mapping maximum intensity spatial locations. These complex intensities extracted by scattering center synthesis provide spatial locations and relative phases. These locations and complex amplitudes are passed through a FF STG producing a FF RCS. This FF RCS is compared to the true FF RCS generated from the real locations.

IQ data. ISAR processing interpolates real or simulated polar formatted NF frequency and azimuth dependent data to cartesian k-space. K-space data is transformed into spatial data through a rectangular Discrete Fourier Transform (DFT). This spatially distorted data is corrected for NF effects producing spatial imaging data necessary for RCS characterization with NF measurements. However, the physical measurement parameter limitations and desires are considered before the imaging process is implemented.

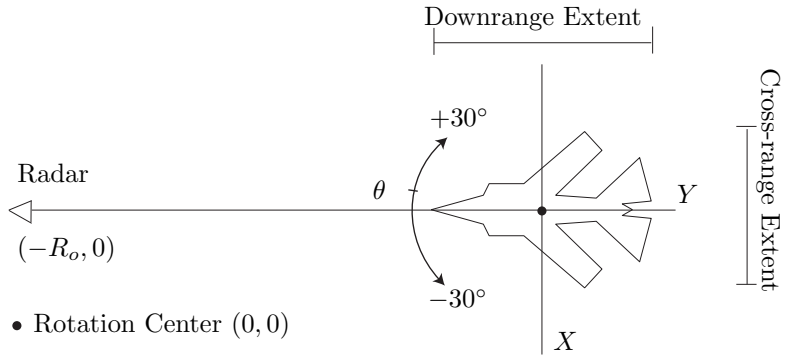

Figure 3.2: A generic aircraft measured at radar to target rotation center distance, $R_o = 155'$, has downrange and cross-range extents $60'$ and $45'$, respectively. The aircraft is rotated through a 60° azimuth in 1° increments.

3.2 Measurement Design

There are several parameters considered before beginning ISAR measurements. Some parameters are limited by target extent, measurement facility, equipment, or processing techniques. Some requirements induce cyclic effects needing multiple refinements throughout the process.

This section defines the physical and desired measurement limitations. These limitations are then used to design the measurement parameters used in the simulation. The layout of Fig. 3.2 establishes some existing physical limitations. These parameters include:

- The target's cross-range extent is $45'$.
- The target's rotation is limited to an azimuthal range up to $\Theta = 60°$.
- The target's rotational increment θ is limited to a 1.0° minimum.
- The target's downrange extent is $60'$.
- The desired downrange and cross-range resolutions are both less than or equal to 0.5".
- The distance from the radar to target rotation center is $R_o = 155'$.
- The radar's frequency range is limited to 6 GHz $\leq f \leq$ 18 GHz.
- The illumination geometry is limited to a monostatic NF environment.

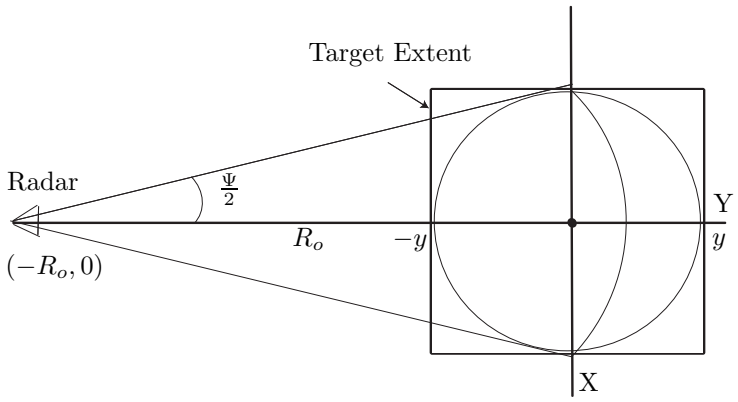

Figure 3.3: Geometry for RCS measurement radar aperture design: For large target RCS measurements, a half power beam width, subtending a target's extent, requires a very wide fan beam.

This chapter uses these parameters to identify the apertures role in target illumination and the effects target size has on aperture size. Additionally, this section shows the dependence resolution has on frequency and azimuth. However, it is the sampling of frequency/azimuth data that determines the imaging extents.

3.2.1 Aperture. Aperture size is dependent upon the target extents, frequency, and the illumination distance. The horn size is determined by an accepted illuminating beam pattern's power loss across the target's extent. In many applications, this power loss is minimized to less than or equal to half the peak beam power. Utilizing the measurement geometry of Fig. 3.3, an angle $\Psi \approx 21^\circ$ subtends the target's largest dimension $d = 60'$ when rotated into the cross-range extent. At a measurement distance $R_o = 155'$, this angle should equal the Half Power Beam

Width (HPBW)

$$\Psi \quad = \quad 0.88\frac{\lambda}{d} \text{ rad}, \tag{3.1}$$

where d is the horn's horizontal width and λ is wavelength. Solving Eqn (3.1) for d, results in a radar horn horizontal width approximately equal to 2" at a *maximum* frequency $f = 18$ GHz. Maximum frequency is used because HPBW is proportional to wavelength. Therefore, as the frequency decreases the HPBW broadens and decreases the power loss across the target's extent.

In addition to horizontal illumination, vertical illumination and aperture gain determine compromises required for acceptable horn dimensions. Pyramidal horns used for RCS measurements of large targets, whose vertical extent is much smaller than length or width, are not dimensionally square. Therefore, a smaller vertical HPBW subtends the target's vertical extent and minimizes floor and ceiling illumination. Equation (3.1) shows that increasing the aperture's vertical dimension decreases the vertical HPBW. This decrease aids in minimizing these extraneous returns and decreases undesirable signal contributions. An increase in the horn's vertical dimension is also beneficial for increasing radar gain.

Gain for a rectangular aperture is dependent upon effective horn dimensions and wavelength, where effective aperture dimensions are determined by the aperture's losses [2]. This gain is determined by

$$G \quad = \quad 4\pi\frac{A_{eff}}{\lambda^2} \ , \tag{3.2}$$

where A_{eff} is the horn's effective area [13]. Therefore, a balance between horn dimensions and wavelength must be obtained to acquire acceptable target illumination with maximum gain.

The target's complete illumination depicted in Fig. 3.3, accounts for all scattering point contributions and interactions necessary for RCS characterization through a Near-Field to Far-Field Transformation (NFFFT). Additionally, the HPBW of Eqn. (3.1) used to established the required

horizontal illumination is also used for vertical illumination. If HPBW is too wide, then contributions from facility boundaries are acquired. These contributions are usually attenuated to negligible levels using absorber material outlining facility walls, floor, and ceiling. However, these materials are very costly and in some cases absorber use is minimized by hardware gating, limiting rotation azimuth, or increasing vertical horn dimensions. These methods are used to decrease facility boundary multibounce effects. However, this *simulated* environment assumes only horizontal illumination. Therefore, the vertical horn extent is used only for determining the aperture gain.

For real measurement environments, the vertical horn's HPBW is calculated similar to horizontal HPBW and is equated to a vertical replica of Fig. 3.2. Using a target's vertical extent approximately equal to $16'$ and radar to target separation $R_o = 155'$, the required vertical HPBW is $\Psi \approx 6^\circ$. Using Eqn. (3.1), this HPBW results in a minimum vertical horn dimension, $d \approx 6$". Assuming no losses in aperture gain, effective area A_{eff} is equal to physical area A. Using this assumption and a *minimum* frequency $f = 6$ GHz, Equation (3.2) results in a minimum approximated square aperture gain $G \approx 39$.

In real applications, return signal strength must be above system noise levels. Therefore, allowing for sufficient target illumination in both extent and power requires a balance between horn dimensions and gain. Increasing the horn's effective area increases radar gain and decreases overall illumination area. Additionally, a significant decrease in vertical horn extent results in a very narrow radar beam. This narrow beam, if too small, neglects vertical contributions toward total target signature. In this simulation, the illumination and imaging is limited to the two-dimensional horizontal plane of Fig. 3.2. Therefore, the horizontal aperture dimension is $d = 2$" and the vertical dimension is adjusted to establish a desired simulation gain.

This section showed that the radar's aperture size is driven by its application. In this case, a large target is illuminated at short distances. However, its was also shown that aperture size and gain is dependent upon frequency. This frequency can be limited by the radar capability or the

desired threat illuminating frequency range. However, the next section identifies that the desired resolution for radar application is also a factor.

3.2.2 Resolution. Resolution is frequency dependent. Sections 2.2.2 and 2.2.3 illustrated that downrange resolution depends upon illuminating bandwidth and cross-range resolution depends upon illuminating center frequency and aperture extent. Since radars are not designed to operate at all frequencies, bandwidth limits are established by radar application and operational limits. Downrange resolution has variability only in bandwidth. Therefore, downrange resolution is limited by the radar's frequency range limitations. This section establishes the relationship between frequency and azimuth in establishing downrange and cross-range resolutions.

Section 2.2.2 showed that downrange resolution is proportional to bandwidth $\frac{1}{2B}$ and is determined using

$$\Delta y = \frac{c}{2B} . \tag{3.3}$$

Using Eqn. (3.3), a downrange resolution $\Delta\, y = 0.5$", defined in Section 3.2, requires an approximate bandwidth of $B \approx 12$ GHz. However, Section 2.2.3 showed that fixing the center frequency of this bandwidth establishes azimuthal rotation dependence of cross-range resolution. Cross-range resolution is determined using

$$\Delta x = \frac{\lambda}{2\Theta} . \tag{3.4}$$

However, Section 3.2 showed that for this application, target azimuthal rotation is limited to $\Theta \leq 60°$. Therefore, the best possible resolution is for a full 60° rotation. Utilizing a full azimuthal rotation, either a desired center frequency establishes cross-range resolution or desired cross-range resolution establishes a required center frequency. The decision is based on whether application drives radar purchase or an existing radar limits application. Using Eqn. (3.4) and

a desired cross-range resolution less than or equal to 0.5" results in a required center frequency greater than 11 GHz. Therefore, a 12 GHz bandwidth centered on a 12 GHz frequency results in a 6 GHz - 18 GHz frequency range. The selected bandwidth and center frequency either limits or is limited by radar, aperture, and resolution. Downrange and cross-range resolutions are determined from azimuth and frequency ranges. However, the corresponding range sampling rates determine imageable spatial extents.

3.2.3 Extents. Both azimuth and frequency sampling rates determine ISAR imageable cross-range and downrange extents, respectively. However, computational burden increases with higher sampling rates. Additionally, large target rotational hardware is limited to 1° azimuthal increments. Appendix G illustrates how these increments result in large targets being well under sampled. Therefore, a significant increase in hardware rotational fidelity is necessary to image large targets in compact ranges. However, if scattering center response, magnitude, and phase are predictable throughout rotation, interpolation techniques can be applied to synthetically enhance rotational fidelity [12].

Appendix G shows that limiting cross-range and downrange extents to 100" × 100" also relieves computational burden by reducing the required sampling rates necessary to satisfy the Nyquist criteria. Limiting downrange and cross-range extents and following the phase study of Appendix G results in minimum frequency and azimuth sampling of 600 and 1000 samples, respectively. This reduced sampling relieves computational burden and provides a spatial environment still satisfying the NF criteria necessary for large target illumination.

This section showed that the target's size effects many measurement process parameters. The horn's illuminating extent, gain, and extents are all directly or indirectly affected by target size. Additionally, the sampling rates increase computational burden with increasing target extents. One method for reducing this computation burden in a simulated environment is to reduce the target's model fidelity. Target model fidelity can be reduced by approximating ISAR targets with scattering

centers. These scattering centers represent reflective points on a target's surface. This model is developed in the next section by approximating a target using isotropic point scatterer groups.

3.3 Scattering Centers

Approximating a target using scattering centers provides a basis for using ISAR images or scattering maps to characterize large target FF RCS. Therefore, this section discusses the scattering model, assumptions, and the scattering role in target approximation within the simulation.

This target approximation requires a high frequency model, where high frequency implies target scattering sources are small relative to wavelength. Therefore, using high frequency Geometric Optics (GO) approximations for this model establishes justification for approximating scattering points as isotropic radiators [1, 13]. An isotropic radiator's electric field is described by [1]

$$\vec{E} = \vec{p}\frac{1}{4\pi r^2}e^{(-jkr)} , \tag{3.5}$$

where $\vec{p}$ is the polarization vector, $\frac{1}{4\pi r^2}$ is propagation amplitude decay, and kr is propagation phase, dependent upon wavenumber $k = \frac{2\pi}{\lambda}$ and observation distance r. The isotropic radiator's scattered electromagnetic field is dependent upon the electromagnetic field incident upon its surface

$$\vec{E^i} = \vec{p_i}Ae^{(-jkr)} , \tag{3.6}$$

where A is the transmitted field strength, $\vec{p_i}$ is the incident field polarization vector, and r is the radar to scattering center propagation distance. This incident field induces currents on the scattering center and the scattering center radiates the energy back to the radar. Additionally, incident energy reflected is dependent upon material parameters and is summed up in the reflection coefficient. The reflection coefficient is complex and has a magnitude and phase ranging from 0 - 1 and $0^\circ - 180^\circ$, respectively [13]. Therefore, the received monostatic scattered electromagnetic

field is

$$\vec{E^s} \quad = \quad (\vec{p} \cdot \vec{p_i}) \, \frac{Ag}{(4\pi r^2)^2} e^{(-j2kr)} \ , \tag{3.7}$$

where g is the reflection coefficient, the dot product identifies polarization mismatches, and two-way propagation is satisfied by squaring the propagation decay and doubling the phase [2]. Polarization mismatches between incident field and scattering center or scattered field and receiving aperture result in a Polarization Loss Factor (PLF). This PLF ranges from $0 - 1$ and adjusts the received magnitude through the dot product based on these mismatches. However, in the synthetic process the polarization mismatches, if present, are assumed negligible or accountable using the reflection coefficient. Therefore, the scattered electromagnetic field is represented as

$$\vec{E^s} \quad = \quad \frac{gA}{(4\pi r^2)^2} e^{(-j2kr)} \ . \tag{3.8}$$

A reflection coefficient, whose magnitude is less than one, accounts for reflected energy lost through absorption, transmission, and, in this assumption, mismatched polarization. If phase components are not equal to zero, phase changes are induced by a surface's scattering nature. Surface induced phase changes add an additional phase shift measured at the radar. This phase shift alters true scattering center phase and induces more constructive or destructive interference between scatterers. These interactions result in either larger or smaller coherently summed RCS. Therefore, synthetic scattering centers are defined by location and complex reflection coefficient accounting for amplitude losses and phase shifts in the original signal. Accurate representation of scattering center characteristics is necessary for generating a physical target approximation with scattering maps. *However, as shown in Section 2.2.3, if the reflection coefficient assumed independent of azimuth or frequency its induced phase change is constant for all samples. Therefore, it is taken outside the DFT of Eqn.* (2.14) *and has not effect on downrange or cross-range imaging.*

Sections 3.2 and 3.3 established the NF measurement and target models. The target is

approximated as a group of isotropic scattering centers, whose scattering is spherical. The spherical scattering is used to model amplitude decay and resulting phase. The amplitude and phase are also dependent upon a complex reflection coefficient, which is assumed constant in all samples. However, there are other scattering wave effects. These effects are covered in the next section by defining what is meant by NF measurement and how this environment is related to target and aperture size.

3.4 Near-Field Range

A facility's NF environment is determined by aperture size, target size, radar/target separation distance, wavelength, and radar parameters. Limiting the radar to one antenna, without beam correction, creates a monostatic measurement environment. This environment eliminates the cost of unnecessary beam correction equipment. However, it also limits its direct application to FF measurements. FF RCS measurements require target planar radar illumination, where all scattering points at equivalent downrange distances are in phase. Approximating electromagnetic propagation using spherical Geometric Optics (GO) results in an equiphase wavefront existing only at infinity [1]. Therefore, planar RCS measurements are not physically realizable. However a user specified target extent propagation phase tolerance is used to approximate FF illumination conditions [13]. Figure 3.4 shows the propagation phase difference kh, where k is the wave number and h is the spatial difference, across a target's extent decreases as the propagation distance increases. Therefore, defining an acceptable phase difference for a target's extent establishes a minimum approximated FF range.

This section shows that FF range is dependent upon the source's maximum extent. The source is defined by the electromagnetic waves origination. The initial source is the radar's transmission through the horn aperture illuminating the target. However, the currents induced on the target surface produce an additional electromagnetic wave whose source is the target. Therefore, the FF criteria is dependent upon the radar aperture and the target. Furthermore, since the target

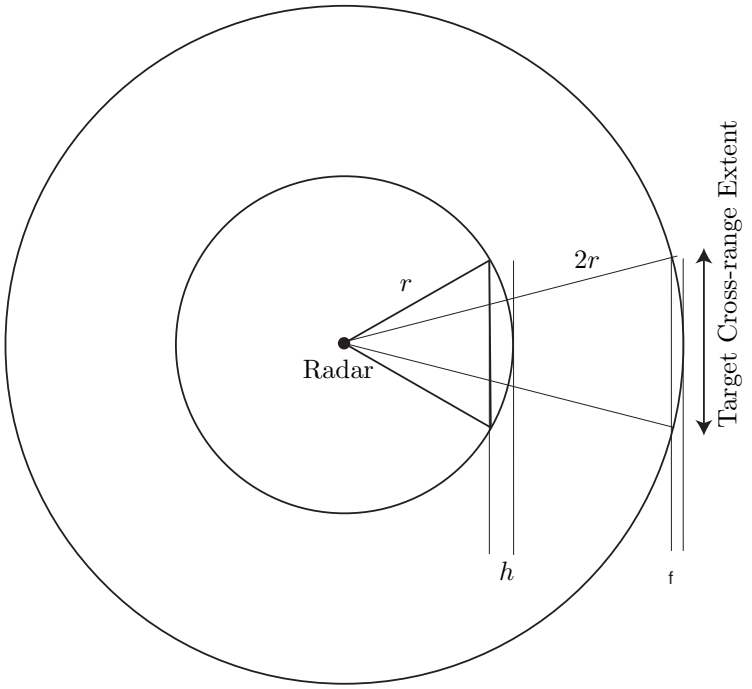

Figure 3.4: The far-field approximation is arbitrary and dependent upon the radar measurement phase difference tolerable for a specific application. As an electromagnetic wave propagates, the phase variance kh (where k is the wavenumber) across the target extent decreases as the propagation radius r increases.

is larger than the radar aperture it is shown that the target requires a much larger measurement distance.

3.4.1 Target's Near-Field Scattering. The target extent, illumination range, wavelength, and acceptable phase tolerance are used to approximate FF required range. This relationship and a typical phase tolerance $\frac{\pi}{8}$ result in a FF required range derived in Appendix B by

$$r = 2\frac{d^2}{\lambda} , \tag{3.9}$$

where d is the target's largest dimension and λ is wavelength. Since r is proportional to $\frac{1}{\lambda}$, shorter wavelengths or higher frequencies are the most range limiting and require longer propagation ranges. As an example a target's largest extent $d = 60'$ is illuminated by a *maximum*

frequency $f = 18$ GHz having a wavelength $\lambda = \frac{c}{f}$ results in a target's FF *scattering* distance $r \approx 40$ km. Therefore, a facility not satisfying this FF requirement is considered a NF range. Facilities satisfying this constraint are impractical to construct. Subsequently, a compact range requires hardware and/or software field correction.

This section established that the radar aperture is receiving NF scattering due to the target's size and its distance from the radar. However, radar antenna illuminating characteristics must also be considered. As shown in the next section, in monostatic NF measurement environments the target size is the limiting factor for illumination characteristics. Since the target is much larger than the radar horn dimensions, the target is actually FF illuminated.

3.4.2 Radar's Far-Field Illumination. It is not a good idea to operate within an aperture's illuminating NF range. Since the radar aperture is much smaller than the target, its NF maximum distance is much lower than a large target. Therefore, large target scattering at the illuminating NF range is improbable to predict. This unpredictability makes NF measurements a difficult extension to FF RCS characterization [13]. However, extending the illumination and scattering further from the source, the waves can be approximated by either cylindrical or spherical wave propagation. Additionally, operating at ranges satisfying the FF range allows a propagating wave approximation using planar waves [1]. The horn's largest dimension and the relationship described in Eqn. (3.9) determine *illuminating* FF requirements.

As an example, utilize the horizontal horn width dimension of 2", a $\frac{\pi}{8}$ phase tolerance, and *maximum* frequency $f = 18$ GHz. Equation. (3.9) shows an *illumination* range of 155' satisfies the radar horn's minimum FF *illumination* range of approximately 12". Therefore, the target is illuminated in the radar's FF.

This section showed that based on *illuminating* or *scattering* source size and the FF range requirement of Eqn. (3.9), the target is FF *illuminated* and the horn receives NF *scattering*. Even though the target is in the radar's FF illumination, the illuminating electromagnetic waves are still

modelled as spherical waves. This computational model keeps the electromagnetic wave properties consistent and maintains the illuminating accuracy.

3.4.3 Summary and Scenario Physical Parameters. This chapter established the physical measurement and scattering models necessary for the NF STG and the NF ISAR process components shown in the NFFFT process of Fig. 3.1. Therefore, an input file is developed to provide these parameters to the NF STG. These parameters are used by the ISAR NF STG to generate the simulated measurement geometry in Fig. 3.5. The input file and Fig. 3.5 establishes the measurement parameters which include:

- Desired frequency range is within 6 GHz $\leq$ f $\leq$ 18 GHz.
- Radar to target rotation center distance is set at $155'$.
- Rotational azimuth has 1001 samples.
- Frequency range has 1001 samples.
- Azimuthal rotation range is within -30° $\leq$ θ_r $\leq$ 30°.
- Horn horizontal and vertical dimensions are 2" and 16", respectively.
- Scattering center quantity is scenario dependent.
- Scattering center spatial distribution are limited to two-dimensions to simplify the problem.
- Cross-range and downrange locations are based on individual scattering centers within a scenario.
- Scattering center reflection coefficients are based on individual scattering centers within a scenario.

Other constants and parameters may apply but are not necessarily user adjusted. Those parameters listed with numerical values are held constant unless alteration presents further process understanding. These values exceed or match the minimum values calculated in the previous

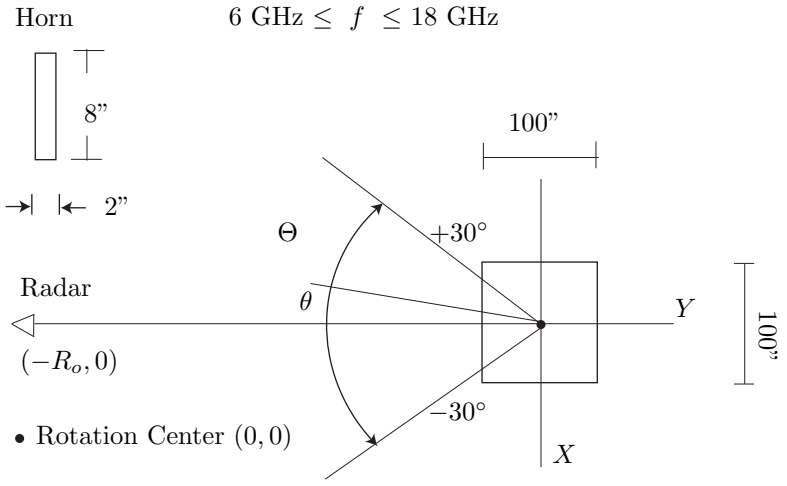

Figure 3.5: A 100” x 100” target extent is measured at a radar to target rotation center distance $R_o = 155'$. The target is rotated through a 60° azimuth in 0.06° increments and scattering centers are illuminated synthetically by the specified bandwidth within this area.

sections. The other parameters, in a real measurement environment, are specifically target dependent and are unknown and embedded in the ISAR data. These parameters are used in the ISAR NF STG of Chapter IV for specific target configurations to generate NF IQ data needed for the ISAR processing routine of Chapter V to create accurately representative ISAR scattering maps.

IV. Radar Near-Field Synthetic Target Generator

The Near-Field (NF) Synthetic Target Generator (STG) establishes the two-dimensional Inverse Synthetic Aperture Radar (ISAR) rotational illumination geometry of Fig. 4.1. This process is simulated to minimize extraneous real world interactions and noise. The STG simulates monostatic continuous wave radar target illumination through azimuthal rotation increments. The result is frequency and azimuth dependent In-phase and Quadrature (IQ) complex data from the coherently summed NF target scattered electromagnetic fields.

This chapter utilizes the parameters developed in Chapter III to define the simulated STG in the Near-Field Far-Field Transformation (NFFFT) process of Fig. 4.2. These parameters include

- Desired frequency range is within 6 GHz $\leq$ f $\leq$ 18 GHz.
- Radar to target rotation center distance is set at $155'$.
- Rotational azimuth has 1001 samples.
- Frequency range has 1001 samples.
- Azimuthal rotation range is within -30° $\leq$ θ_r $\leq$ 30°.
- Horn horizontal and vertical dimensions are 2" and 16", respectively.
- Scattering center quantity is scenario dependent.
- Scattering center spatial distribution are limited to two-dimensions to simplify the problem.
- Cross-range and downrange locations are based on individual scattering centers within a scenario.
- Scattering center reflection coefficients are based on individual scattering centers within a scenario.

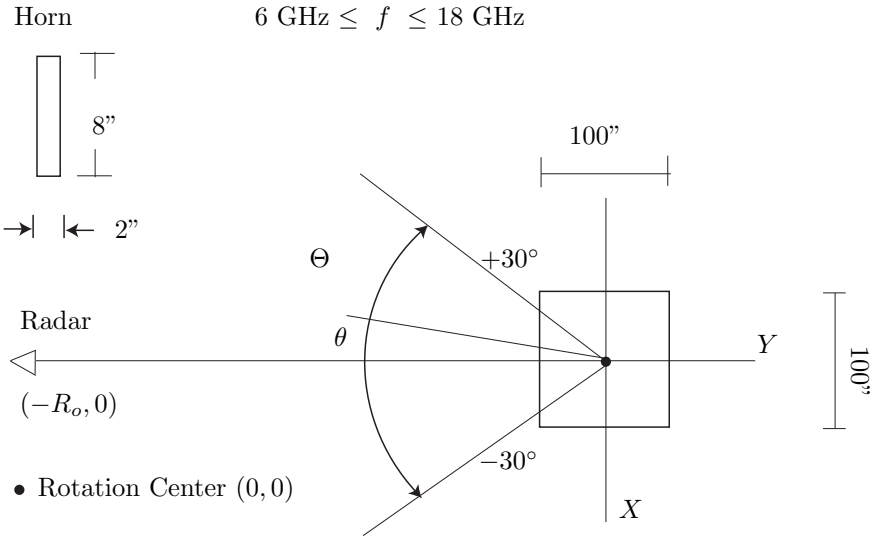

Figure 4.1: A 100” × 100” extent measured at a radar to target rotation center distance $R_o = 155'$. The target is rotated through a 60° azimuth in 0.06° increments and scattering centers are illuminated synthetically by the specified bandwidth within this area.

The STG models the specific effects caused by targets rotation, radar illumination, and the scattered electromagnetic field. The STG goal is to produce a scattered field model using these effects to generate NF IQ data used in ISAR image processing.

4.1 Target Rotation

Utilizing high frequency assumptions, targets are accurately approximated by a scattering center group [13]. Therefore, STG targets are defined by multiple individual scattering center locations and reflection coefficients. This section shows how these locations determine the scattering center rotational geometry needed for ISAR and its effect on propagation distances.

This rotational geometry has two references as shown in Fig. 4.3. The spatial reference is the scattering center's rotational location with respect to the target rotation center and the illumination reference is with respect to the radar. These relationships establish the scattering center range and direction necessary in determining radar pattern effects and propagation decay in returned signals. The illumination relationship is dependent upon scattering center location

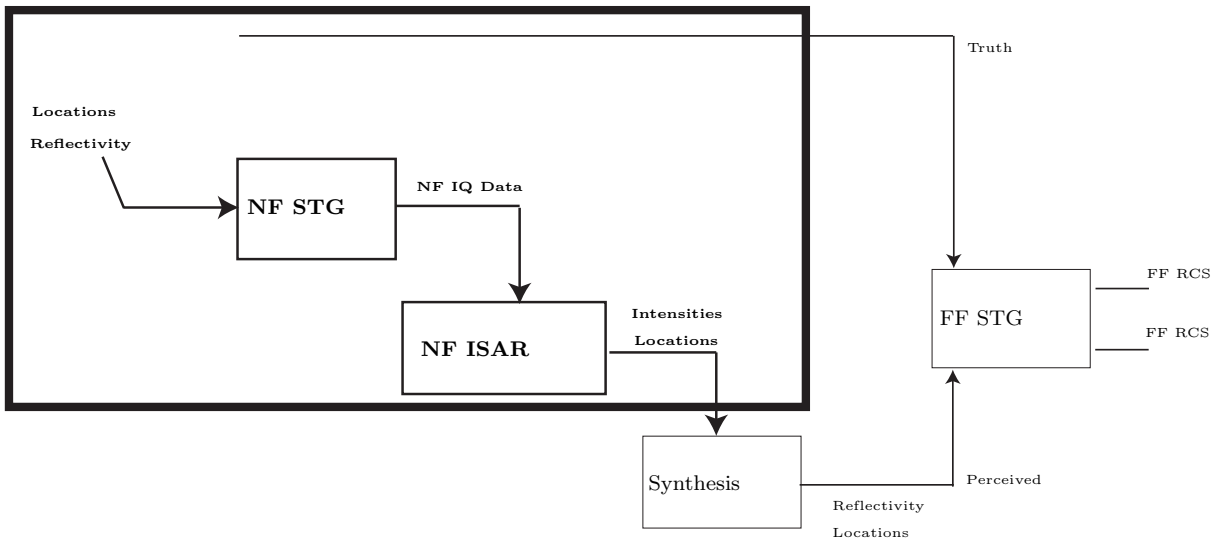

Figure 4.2: The primary focus in this Near-Field to Far-Field Transformation is on developing a spatially accurate NF ISAR image. This focuses on the NF STG and ISAR process. The entire process is describe by starting with the two ISAR Synthetic Target Generators (STGs) that take real scattering center locations and reflectivities and create FF and NF IQ Data. The FF IQ data is considered truth data. The NF IQ Data is imaged by an ISAR code, mapping maximum intensity spatial locations. These complex intensities extracted by scattering center synthesis provide spatial locations and relative phases. These locations and complex amplitudes are passed through a FF STG producing a FF RCS. This FF RCS is compared to the true FF RCS generated from the real locations.

throughout the rotational azimuth.

The trigonometric relationships between scattering center and rotation center establish the initial azimuth $\theta_o = \tan^{-1}\frac{x_o}{y_o}$ and rotation radius $\rho = \sqrt{x_o^2 + y_o^2}$. The scattering center is rotated through an azimuthal range defined by $\theta_o - \frac{\Theta}{2} \leq \theta_o \leq \theta_o + \frac{\Theta}{2}$, where the total azimuth Θ is centered on the initial azimuth. For each incremental rotation angle θ_r in this azimuthal range, scattering center illumination range r is calculated as

$$r = \sqrt{(y_r - R_o)^2 + x_r^2}\,, \tag{4.1}$$

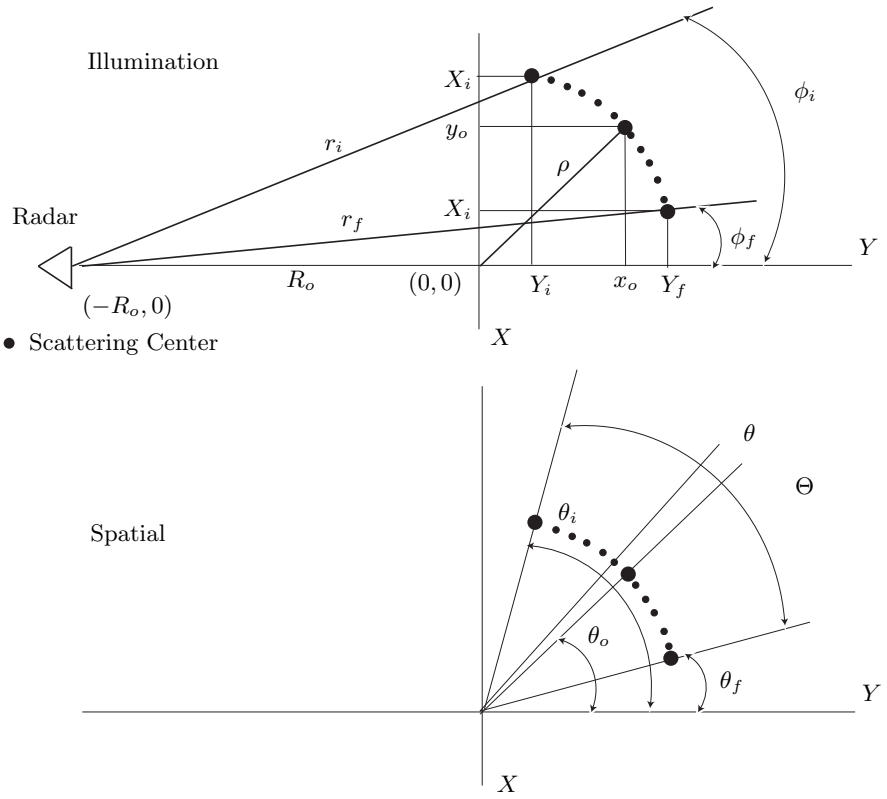

Figure 4.3: Each scattering center has a true location (y_o, x_o) and initial azimuth θ_o defining its distance ρ and direction from target rotation center $(0, 0)$. In ISAR, target scattering centers are rotated incrementally over an azimuth Θ centered on the initial azimuth. Therefore, initial rotation azimuth θ_i is the initial azimuth minus half the rotational azimuth. Each azimuthal step is an additional increment from the initial rotation azimuth to the final rotation azimuth θ_f. These relationships and radar to target rotation center distance R_o determine radar to scattering center rotational direction ϕ and range r through synthetic target generated incremental azimuthal steps θ.

where $y_r = \rho \cos\theta_r$ is the rotational downrange coordinate and $x_r = \rho \sin\theta_r$ is the rotational cross-range coordinate. Illumination range and the rotational cross-range coordinate are used to calculate the radar to scattering center direction $\phi = \sin^{-1} \frac{x_r}{r}$. This propagation direction defines the scattering center's location within the radar's illuminating radiation pattern.

Synthetic radar illumination simplifies the problem by eliminating extraneous signal noise caused by a real measurement environment. The ISAR NF STG simulates a monostatic continuous wave radar illuminating the target utilizing frequency sweeps in azimuthal increments. These frequency/azimuth pairs define the radar's illumination pattern and gain. Illumination pattern and gain are based on the radiating aperture. The rectangular aperture radiation and gain approximations for a pyramidal horn are used to define the scattered energy sampled by the radar.

4.2.1 Radiation Pattern. The radiation pattern defines the radar's illuminating power distribution in space. Since the power distribution is not uniform, the location within this pattern determines the illumination energy on the scattering center. This pattern is dependent upon the illuminating aperture's geometry. The pyramidal horn, a two-dimensional aperture, results in three-dimensional illumination. However, two-dimensional ISAR imaging does not allow for three-dimensional target representation. Therefore, returns from the vertical target extents are assumed to be imaged onto the horizontal plane. The normalized two-dimensional illumination pattern is approximated by

$$E(\phi) = \left[\frac{\sin\left\{\pi\left(\frac{d}{\lambda}\right)\sin\phi\right\}}{\pi\left(\frac{d}{\lambda}\right)\sin\phi}\right]^2, \tag{4.2}$$

where d is the illumination plane's aperture dimension and λ is wavelength [24]. This pattern is a squared sinc function whose mainlobe defines the energy distribution subtending the target extents. Figure 4.4 shows a normalized radiation pattern with a magnitude ranging from $0 - 1$ dependent upon the location within the pattern. However, as mentioned in Section 3.2.1, the desired HPBW coverage in the illumination plane is approximately equal to the target's largest extent. Therefore, the minimum normalized pattern magnitude illuminating the target is approximately equal to 0.5.

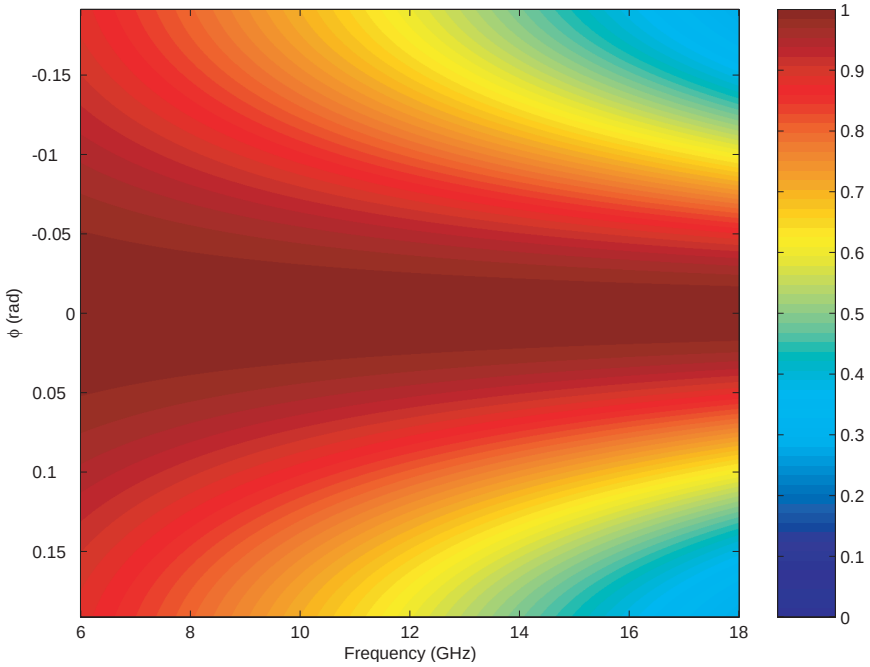

Figure 4.4: This is a normalized radar radiation pattern for a scattering center located 360" downrange from and rotated $\pm 90°$ about the target's rotation center. The mainlobe width narrows as the frequency increases. Additionally, the normalized magnitude decreases as the scattering center moves across the mainlobe with respect to the radar. This figure is representative of a sinc squared function's mainlobe and its dependence upon frequency and location within the beam.

The radiation pattern determines the power distribution within the beam pattern. However, its the radar's gain that determines the peak power within the beam pattern.

4.2.2 Gain. Gain is a transmitting and receiving power multiplier. In the monostatic case, where the transmitter and receiver are the same aperture, the same gain is applied to the transmitted signal and the received signal. A rectangular aperture's gain is approximated by

$$G = 4\pi \frac{A_{eff}}{\lambda^2} , \tag{4.3}$$

where A_{eff} is the aperture's effective capture area. When the aperture area is held constant, the gain is dependent upon frequency, where $f = \frac{c}{\lambda}$ and c is the speed of light. As frequency increases,

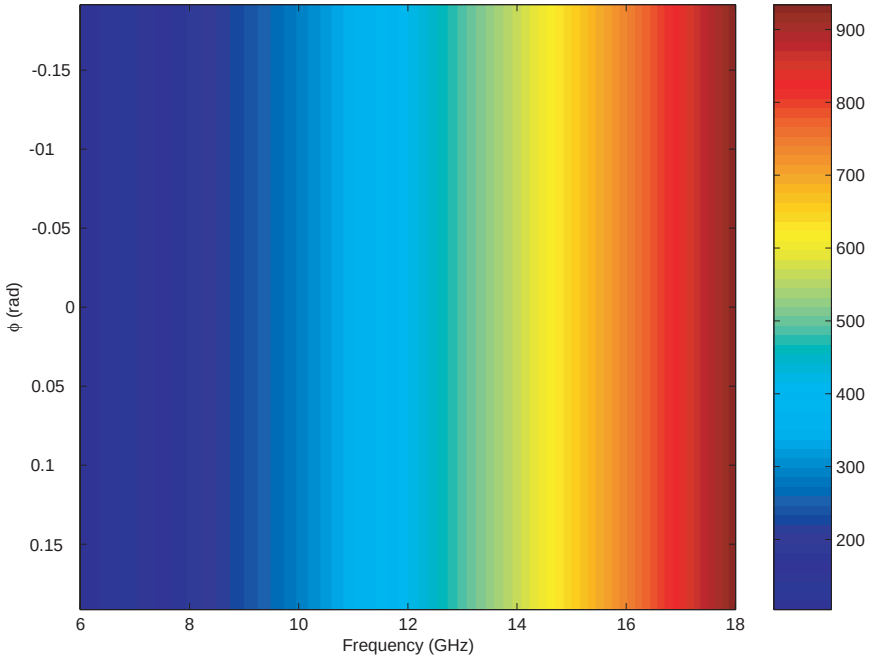

Figure 4.5: The synthetic target generator gain is approximated as a rectangular aperture's gain. Holding the aperture area constant, the gain increases with frequency. Additionally, as a scattering center is rotated through a $\pm 90^\circ$ azimuth, the gain remains constant because it is not dependent upon range or location within the main beam.

λ decreases. Therefore, Fig. 4.5 shows that gain increases with frequency and does not vary with azimuth. However, Eqn. (4.3) does show that gain decreases as aperture area decreases.

Utilizing two-dimensional imaging and limiting the simulated illumination pattern to the horizontal dimension only, the horn's vertical extent is significantly increased, which increases the gain significantly. Since gain is applied to the transmitter and receiver, the total gain for a received monostatic signal is

$$G = \left(4\pi \frac{A_{eff}}{\lambda^2}\right)^2 . \tag{4.4}$$

In the STG, the gain and beam pattern combination

$$E^s = \left[4\pi \frac{A_{eff}}{\lambda^2} \frac{\sin\left\{\pi\left(\frac{d}{\lambda}\right)\sin\phi\right\}}{\pi\left(\frac{d}{\lambda}\right)\sin\phi}\right]^2 \tag{4.5}$$

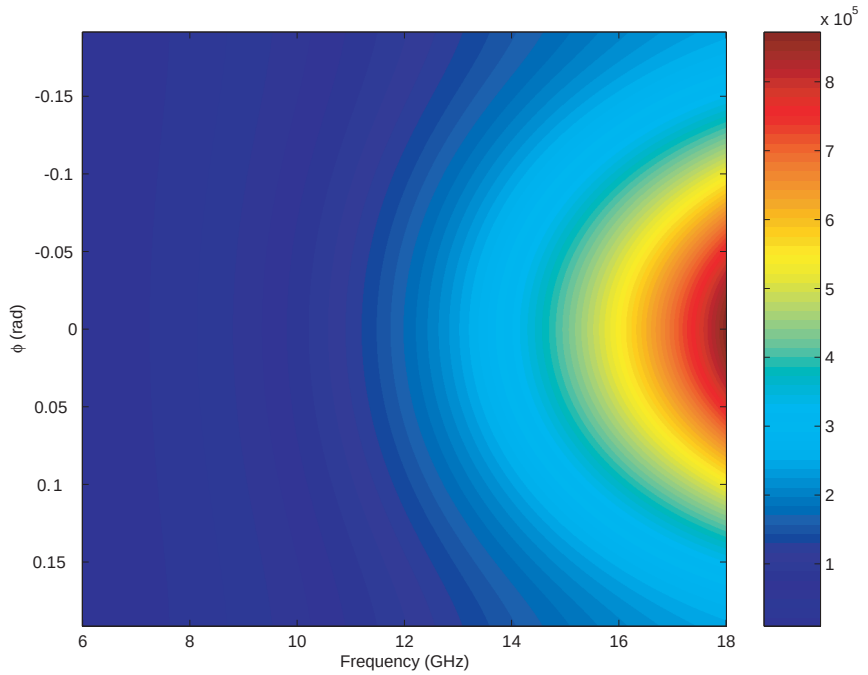

Figure 4.6: Combining the normalized radar radiation pattern with the gain results in a pattern which is more constant at lower frequencies. However, as frequency increases the beam's narrowing overcomes the gain resulting in a pattern whose energy concentration is centered on the mainlobe and is significantly dependent upon location within the mainlobe.

results in the illuminating monostatic scattered electromagnetic field E^s energy distribution of Fig. 4.6.

This section outlined the measurement affects on the energy distribution based on radar and target physical measurement parameters. The following section concentrates on fields generated from isotropic scattering centers and the propagation affects on transmitted energy.

4.3 Scattered Electromagnetic Field

This section uses the results of Sections 4.1 and 4.2 to produce the simulated scattered electromagnetic field used to generate the complex IQ data needed for ISAR processing. The scattered electromagnetic field results from an object's illumination, whose resultant currents reradiate energy back to the radiating source [1]. The ISAR NF STG approximates the isotropic radiator's

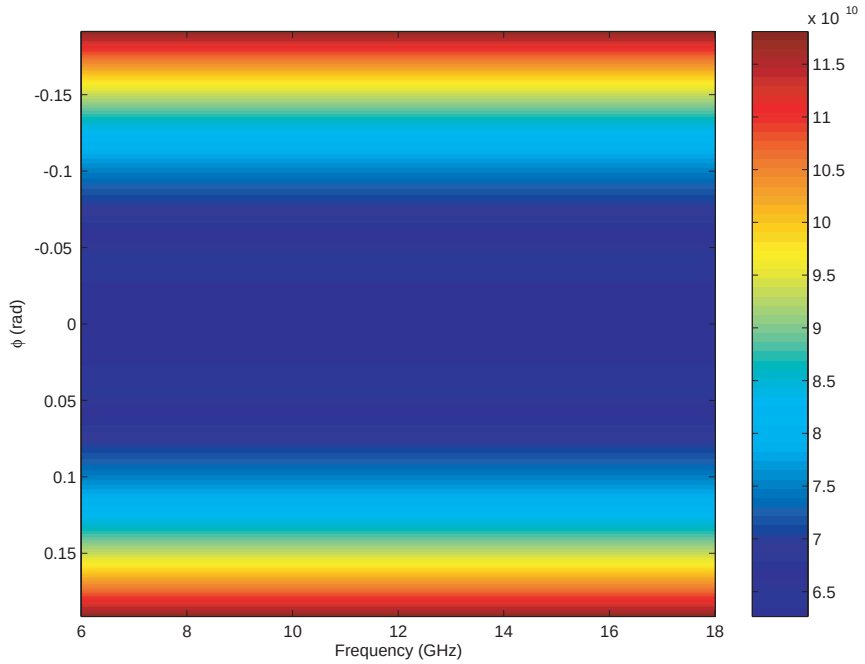

Figure 4.7: A scattering center located 360" downrange from and rotated $\pm 90°$ about the target's rotation center. The decay dependence on propagation distance, r, results in a decreasing decay as it approaches the rotation range extremes. Considering the scattering center's starting location, the propagation distance decreases as it rotates toward the radar.

scattered field utilizing spherical wave propagation. Therefore, the energy received is dependent upon the transmitted and reflected energy decay. Using a monostatic radar and assuming all energy is reflected, the received energy is a product of reflectivity, gain, and the transmitted energy. However, the energy's spherical distribution results in a decay which is dependent upon the propagation radius. Figure 4.7 shows that as scattering location rotates toward or away from the radar, the resultant decay increases or decreases, respectively. Additionally, the electromagnetic field's phase is dependent upon its propagation range. However, the phase is also dependent upon wavelength.

The wavelength defines the number of cycles or periods travelled for a spatial or temporal distance. Therefore, the electromagnetic field's magnitude and phase is approximated by

$$E^s = \frac{gAG^2}{(4\pi r^2)^2} E(\phi) e^{(-j2kr)} , \tag{4.6}$$

where g is the reflectivity and A is the transmitted signal amplitude. The decay term of Eqn. (4.6) $\frac{1}{4\pi r^2}$ is squared applying energy loss due to two-way propagation and the phase term kr is doubled accounting for two-way propagation as shown in Section 3.3. However, initial phase from the radar is not predictable in real measurements. Therefore, the calibration procedure of Section 2.1.2 is used to normalize the RCS and set a phase reference. Since the background and mounts are not a concern in the STG, the STG utilizes the target's rotation center R_o as a phase reference and produces scattered fields resulting in

$$E^s = \frac{gAG^2}{(4\pi r^2)^2} E(\phi)\, e^{[-j2k(r-R_o)]} . \tag{4.7}$$

This scattered field is from one scattering center's contribution. To determine the total electric field, the electromagnetic fields from multiple scattering centers must be coherently summed. The coherent sum accounts for all interactions between scattering contributions adding in and out of phase resulting in a total scattered electromagnetic field

$$E^{tot} = \sum_{j=1}^{\infty} E_j^s , \tag{4.8}$$

where j represents individual scattering centers. Therefore, RCS is the coherent sum of target scattering centers.

This section showed that the ISAR NF STG electromagnetic field simulates a radar with a pyramidal horn, illuminating a large target in the horn's FF. However, the scattered field received by the radar horn is in the target's NF. Therefore, the scattered field is approximated using spherical waves. Even though the horn's FF propagation can be approximated by planar illumination, spherical illumination is used to simplify the process simulation. Additionally, a phase reference is established to simulate the phase reference set through real measurement calibration. This total electromagnetic field and the resulting IQ data are needed for ISAR processing to establish an accurate scattering center map.

4.4 Summary

This chapter develops the simulation process that generates IQ data of Eqn. 4.7 dependent upon the ISAR rotational process, radar illumination characteristics of Eqn.4.2, and scattered electromagnetic field properties. This results in the IQ data for each target reflection point. The coherent summation of each reflection point's contribution results in the total scattered field of Eqn. 4.8. Equation 4.8 represents the frequency/azimuth dependent IQ data for the ISAR measurement process. This STG provides the first step in the NFFFT process of Fig. 4.2. The limited focus outlined in the NF STG and NF ISAR blocks of Fig. 4.2 concludes with Chapter V and the NF ISAR implementation.

V. *Inverse Synthetic Aperture Radar Processing*

Inverse Synthetic Aperture Radar (ISAR) produces radar frequency and azimuth dependent In-phase and Quadrature (IQ) data. This data is processed creating spatially dependent scattering image maps. Accurate scattering maps form the foundation for scattering center synthesis and target Far-Field (FF) Radar Cross-Section (RCS) approximation.

This chapter outlines the process for generating scattering maps using a Trapezoidal ISAR processing technique. This technique uses a two-dimensional rectangular Discrete Fourier Transform (DFT) based method requiring polar to cartesian conversion, rectangular interpolation, to produce scattering maps. In addition a new Near-Field (NF) correction technique is used to correct the scattering map. This correction results in spatially locating scattering centers within the ISAR process resolution.

5.1 Interpolation

This section shows that in order to apply a rectangular DFT, the In-phase and Quadrature (IQ) data must be interpolated onto a uniformly sampled rectangular grid. However, Trapezoidal ISAR of Section 2.3 requires conversion of polar formatted frequency/azimuth data to cartesian propagation space, where k_y and k_x represent two-dimensional cartesian propagation coordinates defining k-space.

The propagation data is dependent upon wavenumber and rotation angle θ_r. Wavenumber $k = \frac{2\pi f}{c}$, where c is the speed of light, is dependent upon frequency f. Therefore, the frequency/azimuth data is overlayed onto the cartesian propagation grid of Fig. 5.1. The cartesian grid's geometry relates cartesian propagation space to polar frequency/azimuth space and is converted using

$$k_y = \frac{2\pi f}{c}\cos\theta_r \tag{5.1}$$

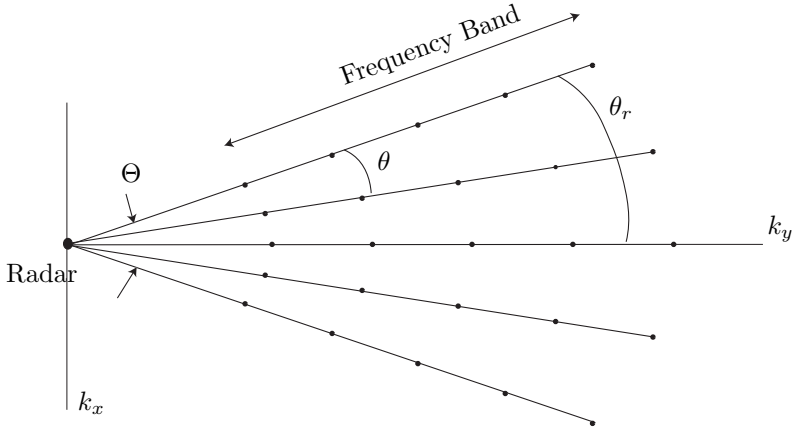

Figure 5.1: ISAR data is collected by recording energy returns from frequency sweeps along target rotation increments θ. This creates polar formatted data with a reference center at the target's rotation center.

and

$$k_x = \frac{2\pi f}{c} \sin\theta_r \ . \tag{5.2}$$

This conversion results in nonuniformly sampled cartesian data and rectangular DFT application to this data results in an unfocused image as shown in Section 2.3. Therefore, this data must be interpolated onto a uniformly sampled rectangular grid.

The interpolation of IQ data onto a rectangular grid is defined through raw data inscription, circumscription, or a combination of both as shown in Fig. 5.2. Utilizing the fully inscribed rectangular interpolation grid of Fig. 5.3 avoids data extrapolation, however sampled data outside this grid is not used in the interpolation. To avoid data extrapolation, interpolation onto a fully inscribed grid is accomplished with two one-dimensional interpolations in k_y and k_x, respectively. Data is first interpolated onto the trapezoidal grid uniformly sampled in k_y whose range is defined by the desired rectangular grid. Using the rectangular grid inscription of Fig. 5.3, the minimum and maximum k_y extents for this rectangular grid are extracted directly from the converted trapezoidal data set. Therefore, the rectangular grid minimum k_y value is the first sample in the row where

• Raw Data

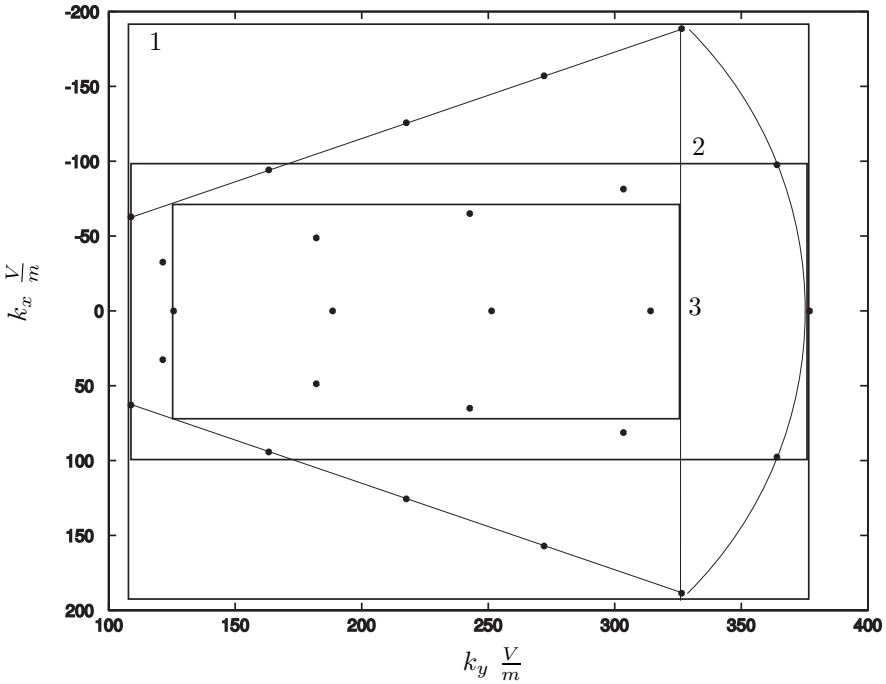

Figure 5.2: Rectangular interpolation boundaries either fully inscribe (1), partially inscribe (2), or are fully circumscribed within (3) the raw data. The grids are not limited to these examples.

$k_x = 0$. The maximum k_y value is the last sample in the row where $k_x = \pm \theta_{\max}$ and $\theta_{\max}$ represents half the full rotation angle. Figure 5.4 shows the resulting data is a trapezoidal grid uniformly sampled in k_y and nonuniformly sampled in k_x. However, the rectangular DFT needs a rectangular grid uniformly sampled in both k_y and k_x.

To complete the two-dimensional interpolation, the trapezoidal grid requires a one-dimensional interpolation uniformly sampling k_x into the rectangular grid overlayed onto the trapezoidal interpolation grid as seen in Fig. 5.3. The range for k_x is determined from the interpolated k_y values. The interpolated data points represent incremental k_y values in constant azimuthal rows. Since k_x values are symmetric across the k_y axis, k_x range is calculated as, $-k_y \tan \theta_{\max} \leq k_x \leq k_y \tan \theta_{\max}$. The trapezoidal data interpolated onto this k_x range results in a uniformly sampled rectangular grid in k_y and k_x as depicted by the k_x interpolated values of Fig. **??**. *Care must be taken in the chosen interpolation routine. The interpolation of the symmetric data set must yield a symmetric*

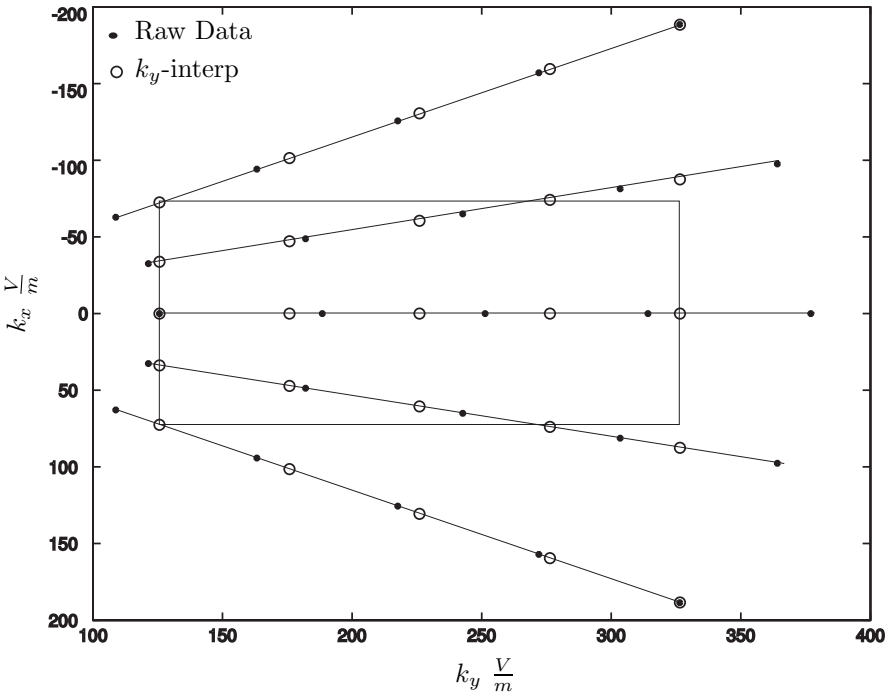

Figure 5.3: The 'keystone' cartesian converted frequency/azimuth data is interpolated onto a trapezoidal grid, uniformly sampled in k_y. The k_y range is determined by the fully inscribed rectangular grid.

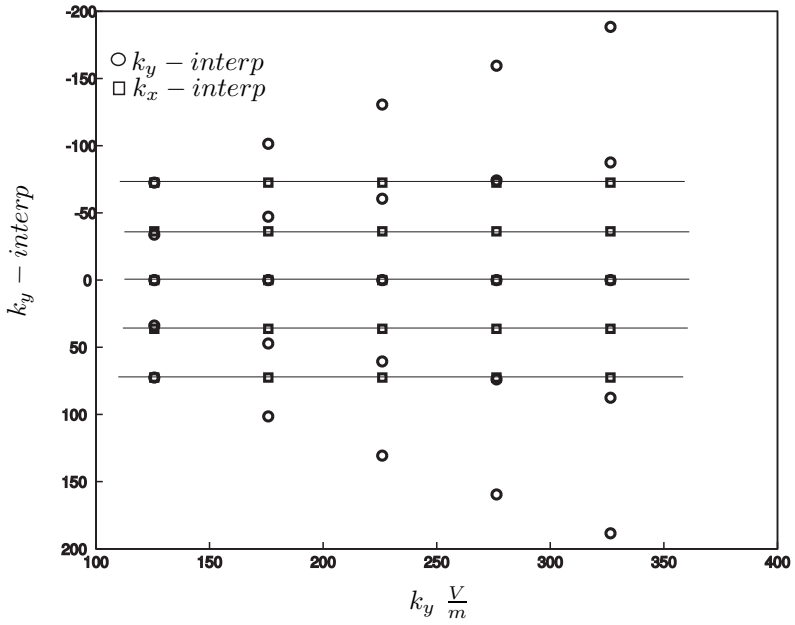

Figure 5.4: The k_y uniformly sampled trapezoidal data is interpolated onto a rectangular grid, uniformly sampled in k_x. This interpolation results in a uniformly sampled rectangular grid completely inscribed in the original keystone data. This uniformly sampled rectangular grid satisfies the rectangular DFT requirement.

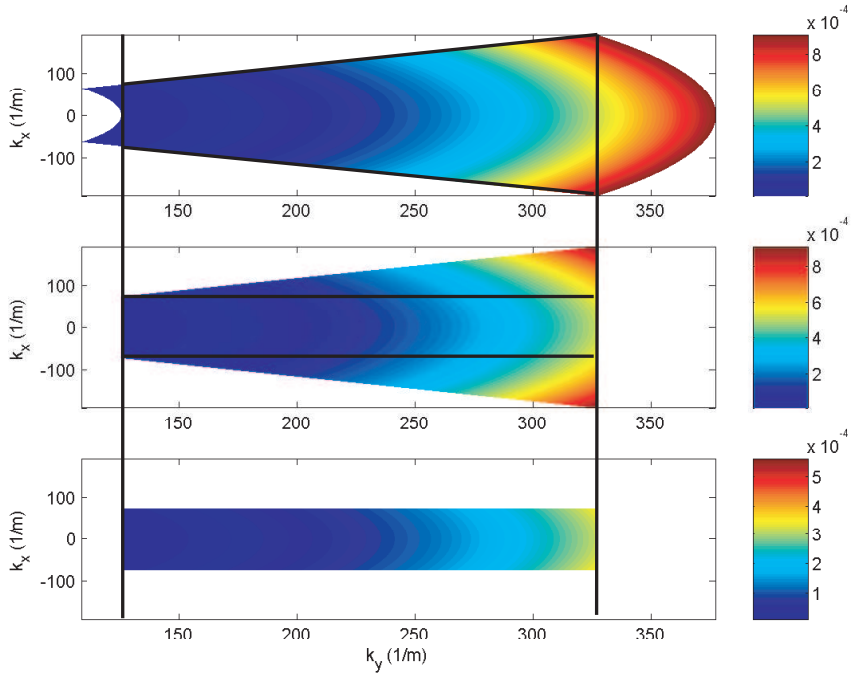

Figure 5.5: Since, the In-phase and Quadrature data is complex, care must be taken in the interpolation process. Original data subsets must result from the original interpolated magnitude and phase data. As the process progresses from top to bottom: The top represents the raw polar data converted to k cartesian values. The raw data is interpolated in the k_y dimension resulting in a raw data subset. Then the data is interpolated in the k_x dimension resulting in a raw and k_y data subset. If the data is not a subset, the original data is under sampled or the interpolation program does not work for this application.

data subset after interpolation. Notice the one-dimensional interpolations in k_y and k_x in Fig. 5.5 results in a symmetric data subsets of raw and k_y interpolated data, respectively

The interpolation steps are outlined in Fig. 5.5 showing that for each step of interpolation, the interpolated region contains the magnitude and phase data as the interpolated region overlayed onto the original data. Since the data represented by k_y and k_x is complex, the interpolation for the data within these new ranges was performed on the magnitude and phase vectors separately. After interpolation the terms were recombined forming the interpolated complex data. This uniform rectangular sampling prepares the data for a rectangular DFT.

5.2 Discrete Fourier Transform

This section discusses effects of using the DFT on finite sampled data and the DFT's role for the imaging process. The interpolation of Section 5.1 prepares the IQ data for a two-dimensional rectangular DFT which is required by Trapezoidal ISAR to transform from the propagation domain to the spatial domain. The kernel

$$\vec{r} \quad = \quad \frac{2\pi f}{c} \sin(\theta)\, \vec{k}_x + \frac{2\pi f}{c} \cos(\theta)\, \vec{k}_y \tag{5.3}$$

is necessary for Trapezoidal ISAR and defines the propagation to spatial domain transform pair of Section 2.3. The Fourier transform is defined for two-dimensional infinite sampling. However, ISAR data is limited in both dimensions. Therefore, the Fourier responses are made up of two-dimensional sinc functions, whose mainlobe width is equivalent to the resolution in each dimension. Additionally, each response has sidelobes that extend beyond the mainlobe in both dimensions.

Sidelobes interact with other sidelobes and target responses. These interactions increase or degrade the true responses due to constructive and destructive interference. Therefore, minimizing the sidelobe magnitudes avoids false scattering responses in the image. Windowing is applied to lower sidelobe levels caused by spectral leakage from limited sampling. The DFT takes advantage of doppler shifts resulting between the azimuth and frequency sampling when the other is held constant. The DFT results in impulse responses identifying scattering centers relative to the spatial transform. These responses must then be related to the downrange and cross-range extents.

5.3 Imaging

This section defines how the DFT impulse responses and the sampling rates are related to the spatial domain downrange and cross-range extents. The imaging extents are defined by the effective frequency and azimuth ranges. Without interpolation, the extents are dependent upon the original ranges and sampling rates. However, interpolation redefines the frequency and/or azimuth

ranges usable by the rectangular grid. Figure 5.6 shows that interpolated ranges and sampling

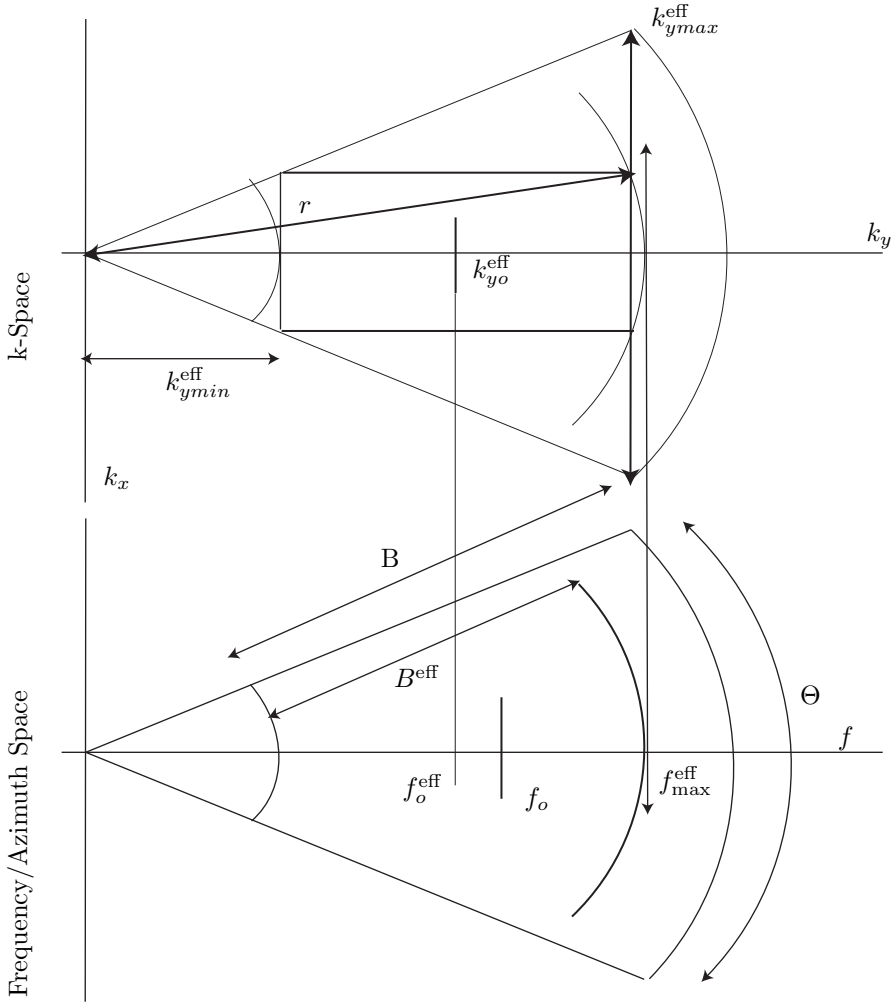

Figure 5.6: The cross-range and downrange extents are dependent upon the resampled increments in effective bandwidth and aperture limited by the k-space rectangular grid inscribed in the frequency/azimuth space keystone. When the resampling in k-space is accomplished. These k-space limitations can be mapped back to the original frequency/azimuth data using the kernel of Eqn. 5.3. If the frequency/azimuth ranges do not contain the same bandwidth and azimuth, then the target extents and resolution are redefined in this process.

rates redefine the bandwidth and azimuthal rotation. Therefore, the image's spatial extents are redefined based on

$$k_y^{\text{eff}} = 2\pi \frac{f^{\text{eff}}}{c} \left(m^{-1}\right) \tag{5.4}$$

and

$$k_x^{\text{eff}} \quad = \quad 2r \tan \frac{\Theta}{2} \ \left(m^{-1}\right) \ , \tag{5.5}$$

where the rectangular grid boundaries redefine the limitations on bandwidth and k_y and k_x coordinates. These limitations are referred to as effective bandwidth B^{eff}, effective k_y-coordinate k_y^{eff}, and effective k_x-coordinate k_x^{eff}. Additionally, r is the propagation range and $\frac{\Theta}{2}$ is the angle to the maximum cross-range extent at the effective center frequency f_o^{eff}, Fig. 5.6. The spatial domain maximum extents are calculated from k-space extents by [12]

$$D_y \quad = \quad 2\pi \frac{N_y}{\Delta k_y^{\text{eff}}} \tag{5.6}$$

and

$$D_x \quad = \quad 2\pi \frac{N_x}{\Delta k_x^{\text{eff}}} \ , \tag{5.7}$$

where N_y and N_x are the number of k_y^{eff} and k_x^{eff} samples, respectively. Additionally, Δk_y^{eff} and Δk_y^{eff} are the respective sample increments. However, because the IQ data originated from NF illumination, which was approximated by spherical illumination, direct extent application to the imaged data results in a spatially distorted image as seen in Fig. 5.7. Therefore, the imaged data must be resampled onto a spatially NF corrected grid [21].

5.4 NF Correction

This section derives the concepts used to correct the spatial imaging extents for the effects of NF propagation. The effects of NF propagation on image data are illustrated and a NF correction is then applied correcting for the cross-range distortion. However, an additional correction is necessary to correct for the downrange NF affects which are approximated by spherical propagation. These

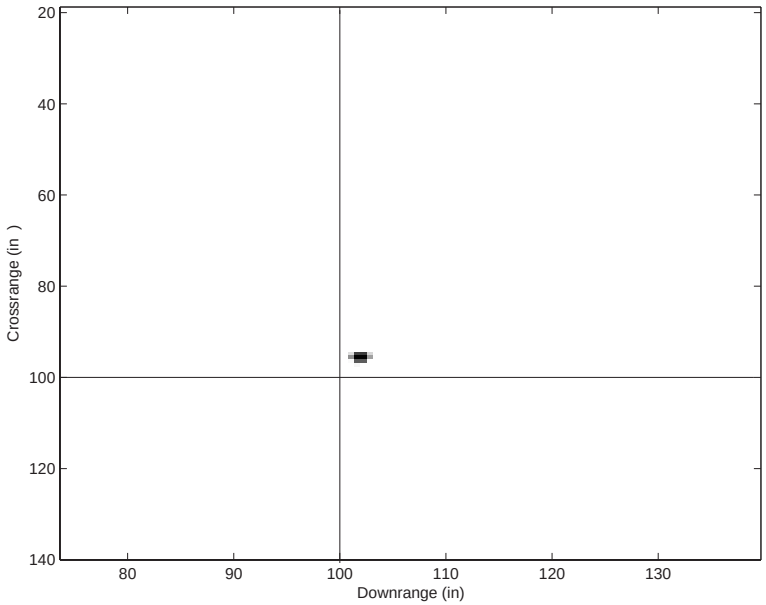

Figure 5.7: Imaging the near-field discrete Fourier transformed data results in a spatially distorted image. A scattering center located at 100" in downrange and cross-range is imaged several inches from its real location. This distortion occurs because spherical waves propagating off the downrange axis take longer to reach the same downrange location as the waves aligned with the downrange axis.

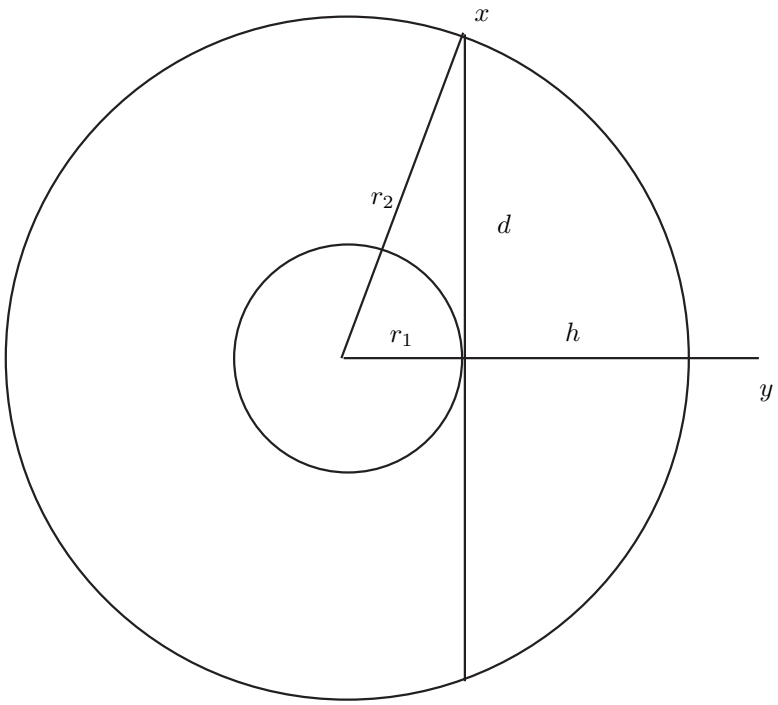

Figure 5.8: Spherical propagation across a target extent d located at downrange position y requires a distance r_1 to reach the target's center. However, the wave must propagate a distance r_2 to reach the target's extent. Therefore, the true downrange distance is the same as the target's center. However, the perceived downrange distance is $r_1 + h$ resulting in a distorted spatial location.

corrections result in a scattering center map that is accurate within the ISAR process resolution.

The NF correction is based on the spherical propagation approximation. A spherical wave propagating in a downrange direction results in a different propagation range for each cross-range location x at a specific downrange location y. Figure 5.8 shows that for a fixed downrange location each cross-range location across a spherically propagating wave results in a different propagation distance which distorts the true downrange location.

The rectangular DFT is dependent upon phase to determine the scattering point locations in downrange and cross-range. Equation (4.6) shows that the electromagnetic field's phase is dependent upon propagation range. Therefore, spherical propagation across the target's extent results in a DFT perceived range further than the actual range. Additionally, the cross-range position is dependent upon the rotational phase shift. Therefore, a scattering center's rotation

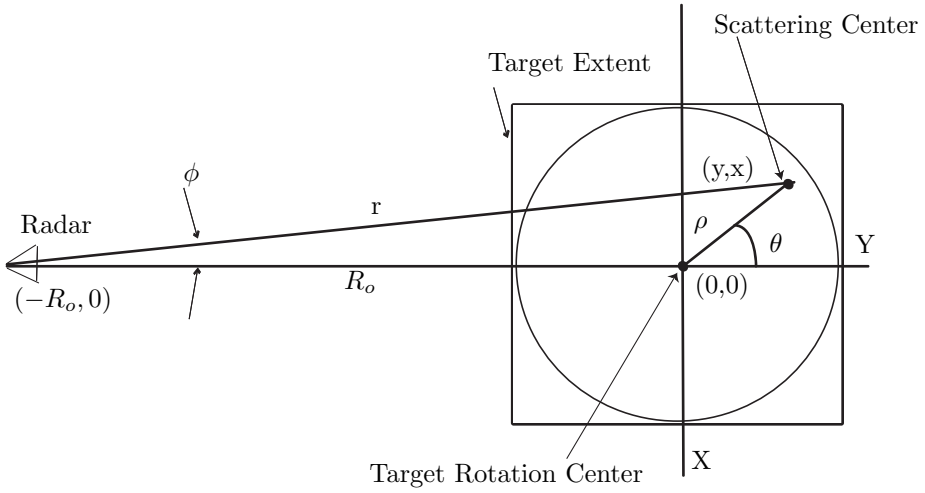

Figure 5.9: A simple target/radar relationship within a measurement facility. The target's rotation center is located downrange from the radar and is the measurement spatial center. The target's reflective point or scattering center is located a distance ρ, from rotation center and is defined as the scattering center's rotation radius. The cross-range and downrange scattering center positions are related to the rotational radius and azimuthal direction from the target rotation center.

from the radar's line-of-sight also results in an additional phase shift induced by the spherical propagation. Cross-range and downrange locations must be corrected for these effects to establish the scattering center's true position.

5.4.1 Near-Field Cross-range Correction [21]. The cross-range position is corrected by looking at the original geometry, Fig. 5.9. The ISAR measurements are taken based on azimuthal increments θ. The cross-range doppler shift s measured by the radar is dependent upon the change

in the propagation distance r with respect to the azimuthal increment [21]

$$s = \frac{dr}{d\theta} . \tag{5.8}$$

The propagation distance is expressed with respect to the measurement geometry's known terms, target to rotation center R_o, rotation radius ρ, and azimuthal increments as

$$r = \left(R_o^2 + 2R_o\rho\sin\theta + \rho^2\right)^{\frac{1}{2}} . \tag{5.9}$$

Using Eqn. (5.8) on the propagation relationship in Eqn. (5.9), the doppler shift is calculated as,

$$s = \frac{R_o\rho\cos\theta}{(R_o^2 + 2R_o\rho\sin\theta + \rho^2)^{\frac{1}{2}}} . \tag{5.10}$$

Important to note is that Eqn. (5.10) is true for FF propagation. In the limit as the measurement distance R_o approaches infinity, the doppler quantity approaches $\rho\cos\theta$. From the measurement geometry of Fig. 5.9, $\rho\cos\theta$ defines the true cross-range position x with respect to the target rotation center. Therefore, using Eqn.(5.9) and solving Eqn. (5.10) for x in terms of s results in

$$x = s\left(\frac{r}{R_o}\right) . \tag{5.11}$$

Equation (5.11) provides the correction factor needed for establishing the resampled extent of x in terms of measurement and propagation distance [21]. In cases where $r < R_o$, the cross-range extent is resampled onto a smaller range extent. However, as r increases and exceeds R_o, the resampled cross-range extent is greater than the original extent range and requires extrapolation outside the original data set as shown in Fig. 5.10. The NF ISAR STG uses a computational minimum as the extrapolation value to avoid division by zero in resampling the cross-range extent.

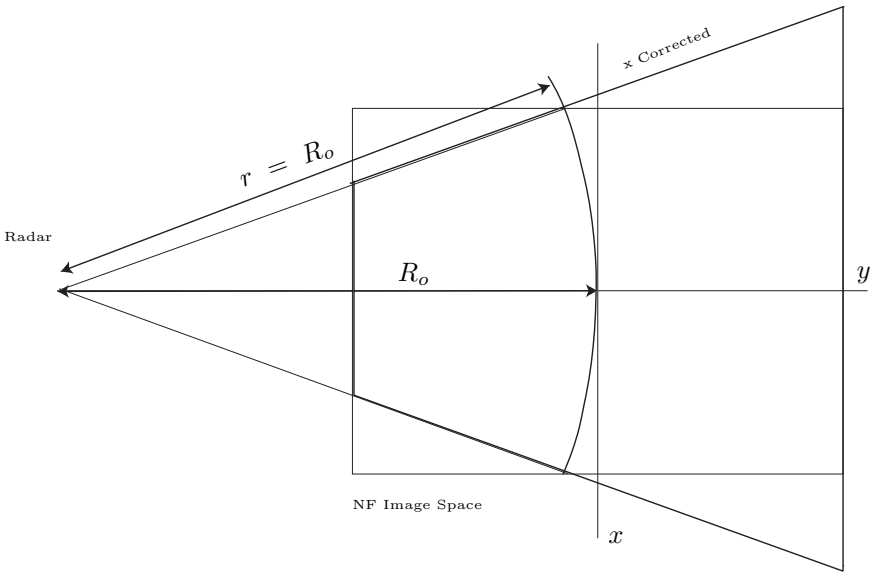

Figure 5.10: The original cross-range and downrange extents are defined by the rectangular boundary. Cross-range extent correction redefines a trapezoidal boundary. This compression and expansion in the boundary results from shorter and longer, respectively, propagation distances, r, with respect to, R_o. The curved contour is points where $r = R_o$. At these points the original cross-range extent is equal to the new cross-range extent.

Therefore, utilizing the geometry in Fig. 5.9 the downrange component y is

$$y = \left(r^2 - x^2\right)^{\frac{1}{2}} - R_o \ , \tag{5.12}$$

where r and x are now corrected for the cross-range changes. Equation (5.12) corrects the downrange extent for the corrected cross-range extent. However, the image is still spatially distorted in downrange due to spherical propagation.

5.4.2 Near-Field Downrange Correction. The additional downrange correction for the approximated spherical propagation is based on the spherical propagation relationships used in the FF requirement development [13]. Using this development and the geometry of Fig. 5.7, the additional propagation distance needed to reach the target extents for spherical propagation h is

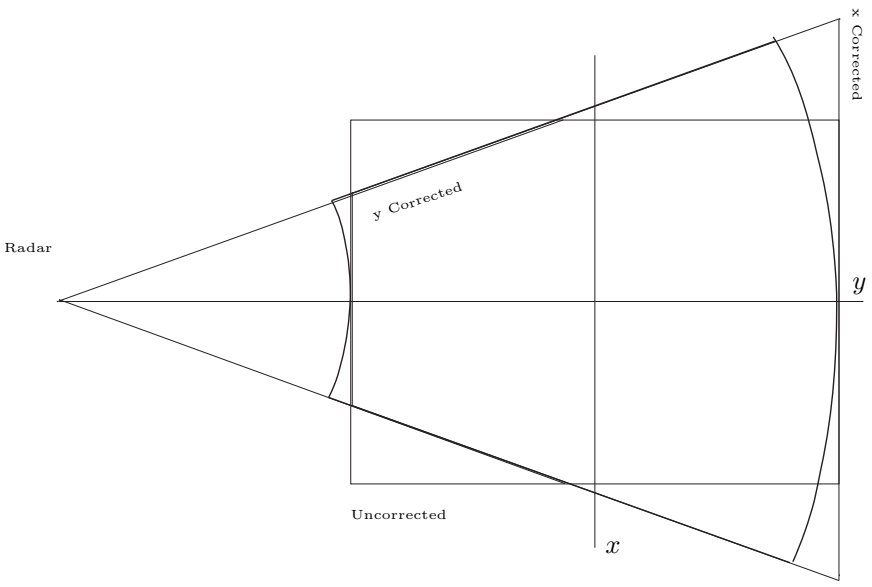

Figure 5.11: The original cross-range and downrange extents are defined by the rectangular boundary. Cross-range extent correction redefines a trapezoidal boundary. Further downrange correction results in the keystone shaped boundary, which corrects for the perceived longer propagation ranges as the scattering center moves further in cross-range.

calculated as

$$h = \frac{d^2}{8r} . \tag{5.13}$$

Since the spherical propagation is longer to cross-range positions than downrange locations, Eqn. (5.13) must be subtracted from the corrected downrange component of Eqn. (5.12) resulting in a true downrange location of

$$y = \left(r^2 - x^2\right)^{\frac{1}{2}} - R_o - \frac{4x^2}{8r} , \tag{5.14}$$

where x is the cross-range scattering center location and represents half the corresponding cross-range extent d. Equation (5.14) results in a decreasing downrange image extent with an increasing cross-range component as shown in Fig. 5.11. Corrections to the cross-range and downrange extents result in an image whose true location is identified within the ISAR resolution. The scattering

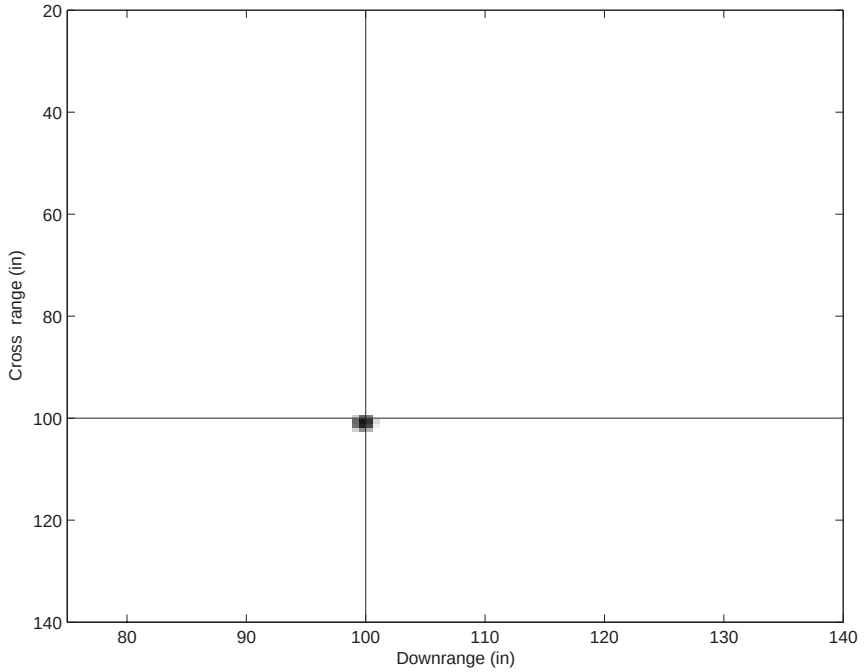

Figure 5.12: Resampling the image to spherical wave corrected extents aligns the scattering center to within the ISAR resolution.

center located at 100" in downrange and cross-range is corrected from Fig. 5.7 and results in a scattering map image within the resolution of the ISAR process as shown in Fig. 5.12. Additionally, a scattering group is imaged in Fig. 5.13 showing that without corrections the scattering center locations are dependent upon the propagation distance and are shifted further downrange. Additionally, the perceived cross-range locations transition from out to within the true cross-range location as the propagation distance increases. This distortion results from using Eqn. (4.7) whose phase, because of its reference to the target rotation center, becomes more negative as the propagation range increases. Transition points where the cross-range location is correct occur where the propagation range is equal to the reference range R_o. Additionally, the perceived downrange location increases with increasing cross-range extent. This increased perceived downrange location results from an increasing propagation range as cross-range extent increases. However, if the image is corrected as shown in Fig. 5.14 then the scattering centers are imaged in the true positions. *This*

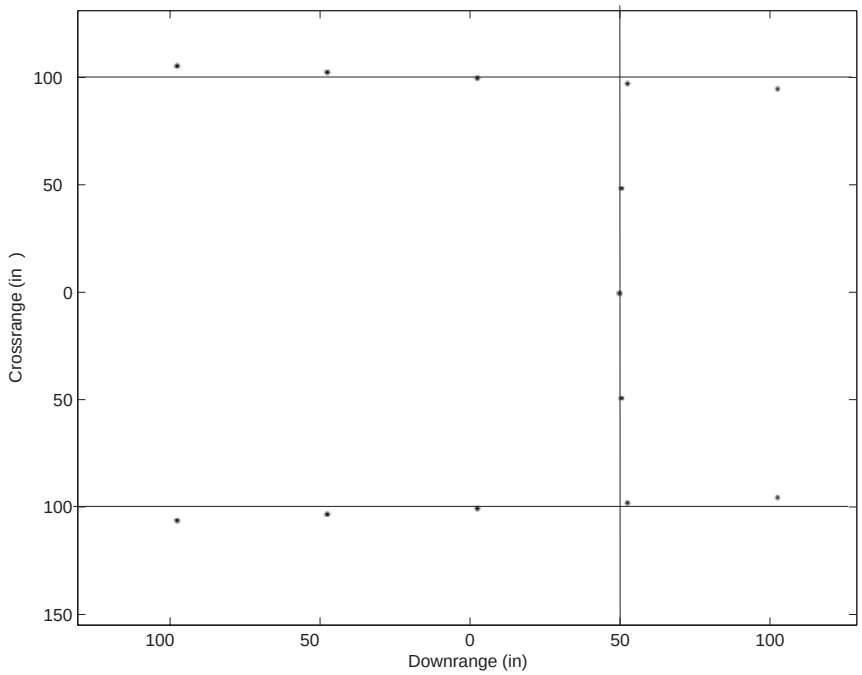

Figure 5.13: Failure to apply cross-range and downrange correction on a scattering center group results in a spatially distorted image. As scattering centers extend further from the radar the phase, as seen in Eqn. (4.7), becomes more negative and the scattering centers are compressed toward the imaging center with increasing propagation range. However, scattering centers located further in cross-range extent require longer propagation ranges. Therefore, the scattering centers perceived further downrange as propagation range increases.

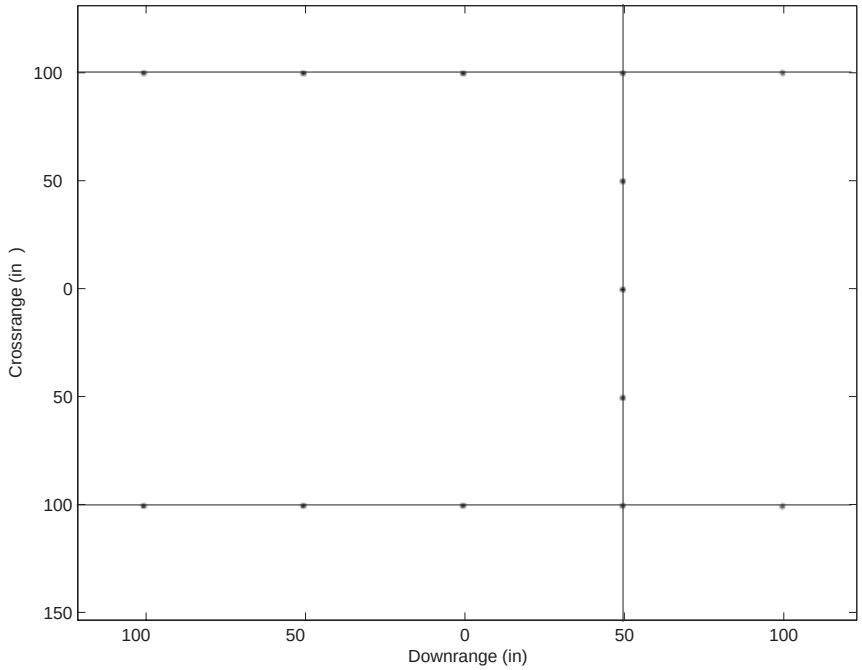

Figure 5.14: Cross-range and downrange correction on a scattering center group show all quadrant are spatially corrected.

correction algorithm is accurate utilizing the $-j2k(r-R_o)$ *convention of Eqn.* (4.7). *If* $+j2k(r-R_o)$ *were used then the correction would actually increase the distortion in the image.*

5.5 Summary

This chapter establishes the NFFFT simulated NF ISAR process of Fig. 4.2. It shows the dependence of Trapezoidal ISAR on uniformly sampled rectangular data which requires the conversion and interpolation of polar formatted frequency/azimuth data. Additionally, imaging the NF IQ data resulted in spatially distorted scattering maps. NF correction resulted in spatially accurate scattering maps limited by the ISAR process resolution. This process does not complete the NFFFT process of Fig. 4.2. However, it provides a foundation for accurate mapping necessary to characterize FF RCS using NF measurements.

VI. Conclusion

The increased need for low observable aircraft requires an efficient and inexpensive method for on-site Far-Field (FF) Radar Cross-Section (RCS) measurement. Conducting these measurements in a Near-Field (NF) monostatic facility at the end of a production line results in significant savings for manufacturers and acquisition programs. Additionally, aircraft are processed much quicker by eliminating the transportation to and the scheduling of subcontracted FF ranges. However, NF measurements are not directly extendable to a FF RCS. Wave propagation is incomplete and scattering interactions are unaccounted for in NF measurements. Therefore, a Near-Field to Far-Field Transformation (NFFFT) must be developed for large target NF measurements. This process begins by developing a NF corrected Inverse Synthetic Aperture Radar (ISAR) process which creates an accurate scattering center map.

Establishing an accurate scattering center map is the foundation for the NFFFT characterization of large target FF RCS. However, the phase study of Appendix G showed that direct NF ISAR application to aircraft size targets is well under sampled within the limited rotational fidelity. Therefore, the real measurement environment was avoided to synthetically increase the fidelity and eliminate noise to produce data that is a function of illumination and scattering only. Therefore, a NF Synthetic Target Generator (STG) is developed to create In-phase and Quadrature (IQ) data needed for the ISAR process. This data is generated by approximating a target as a group of isotropic scattering centers. These scattering centers are illuminated by a continuous wave radar using a pyramidal horn aperture. This aperture is used to approximate the illumination and gain pattern. However, the losses in the system are only based on the individual scattering center reflection coefficients and electromagnetic wave propagation decay. The propagation decay is approximated by a NF isotropic scattering of uniform spherical waves. To account for losses due to possible material parameters, a reflection coefficient is added to induce magnitude losses and phase shifts. These approximations result in NF IQ data generated from radar illumination and isotropic scattering points on a target.

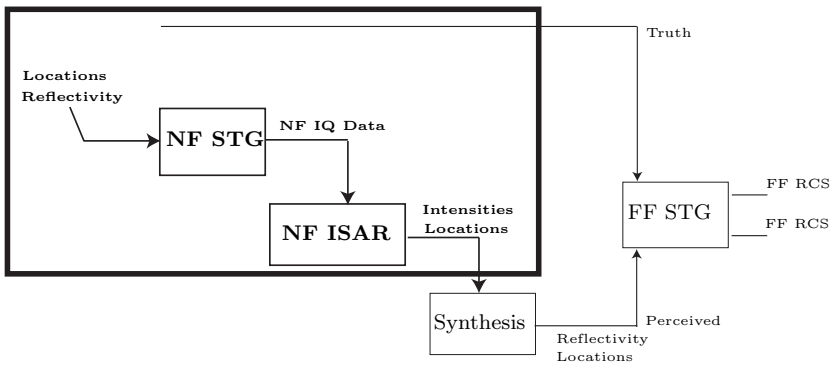

Figure 6.1: The primary focus in this Near-Field to Far-Field Transformation is on developing a spatially accurate NF ISAR image. This focuses on the NF STG and ISAR process. The entire process is describe by starting with the two ISAR Synthetic Target Generators (STGs) that take real scattering center locations and reflectivities and create FF and NF IQ Data. The FF IQ data is considered truth data. The NF IQ Data is imaged by an ISAR code, mapping maximum intensity spatial locations. These complex intensities extracted by scattering center synthesis provide spatial locations and relative phases. These locations and complex amplitudes are passed through a FF STG producing a FF RCS. This FF RCS is compared to the true FF RCS generated from the real locations.

The IQ data is used in an ISAR process to generate an image that defines a target by its response function which is dependent upon the scattering points and measurement properties. The response is determined by a rectangular Discrete Fourier Transform (DFT), which converts the data from frequency/azimuth sampling to spatial sampling. This conversion allows the scattering centers to be related to specific spatial locations within the imaging space. However, ISAR's direct application to this data creates a spatially distorted image. This distortion results from NF effects in the measurement environment. Therefore, the image is resampled onto a spatial grid which is corrected for NF effects. This correction results in the accurate representation of scattering points within the ISAR resolution. An accurate scattering point map is the basis for the full NFFFT process shown in Fig. 6.1. In order to complete this process, scattering center synthesis and

FF illumination must be conducted. The following items represent possible follow-on approaches to scattering center synthesis:

- Scattering centers must be extracted from the NF corrected ISAR image and weighted for magnitude and phase. These scattering centers are illuminated using a FF STG to create FF IQ data. This data is used to calculate frequency/azimuth dependent RCS values. These values are compared to the true scattering center parameters as an iterative process to determine appropriate corrections needed.
- Error analysis determining synthesis accuracy necessary to guarantee RCS correlation within a specified tolerance.
- Develop and/or implement an ISAR process which utilizes data insertion or other technique to accommodate the limitations in large target rotational fidelity.
- Develop and implement a more detailed radar model which utilizes noise and eliminates some approximations with real parameters.
- Apply the synthetic ISAR process to real radar measured IQ data of known simple scattering geometries.
- Apply the synthetic ISAR process to real radar measured IQ data of known complex scattering geometries.
- Apply the synthetic ISAR process to real radar measured IQ data of unknown scattering geometries and compare to real FF data.

The complete NFFFT process creates an inexpensive and efficient measurement environment for aircraft manufacturing companies. The NFFFT implementation results in a faster delivery of low observable systems to war-fighters at a lower cost.

Appendix A. Temporal Radar Signal Development

A phase reference point is required to process Radar Cross-Section (RCS) measurement signals coherently and is established at the measurement area center. The measurement area accommodates a 360° target rotation where the target's extents, length and width, are centered in the measurement area, Fig. A.1. A simple radar signal processing example as described by [12], is used and related to this measurement geometry. A radar's transmitted signal described by,

$$s(t) = b(t)\cos(w_o t), \tag{A.1}$$

where $\cos(w_o t)$ represents a continuous wave signal operating at a carrier frequency, w_o, that is pulse modulated by $b(t)$, an envelope function with a time interval defining the signal pulse width. An example of $b(t)$ is a raised cosine pulse,

$$b(t) = \frac{1}{2}\left[1+\cos\left(\frac{2\pi}{\tau_b}t\right)\right], \tag{A.2}$$

where τ_b is the pulse width. The envelope function's purpose is amplitude modulation within the interval, τ_b, limiting the range from the measurement center. By limiting the pulse width, reflections induced outside this time interval are not received. As the signal returns from the target, the signal is described as,

$$s_b = A|g(y)|\cos\{\omega_o[t-\tau_o-\tau(y)]+\angle g(y)\}\, b[t-\tau_o-\tau(y)], \tag{A.3}$$

or in complex form as[1],

$$s_b(t) = Ab[t-\tau_o-\tau(y)]\,\mathbf{Re}\left\{g(y)\,e^{j\omega_o[t-\tau_o-\tau(y)]}\right\}, \tag{A.4}$$

[1]By using the identity $e^{j\theta}=\cos\theta+j\sin\theta$

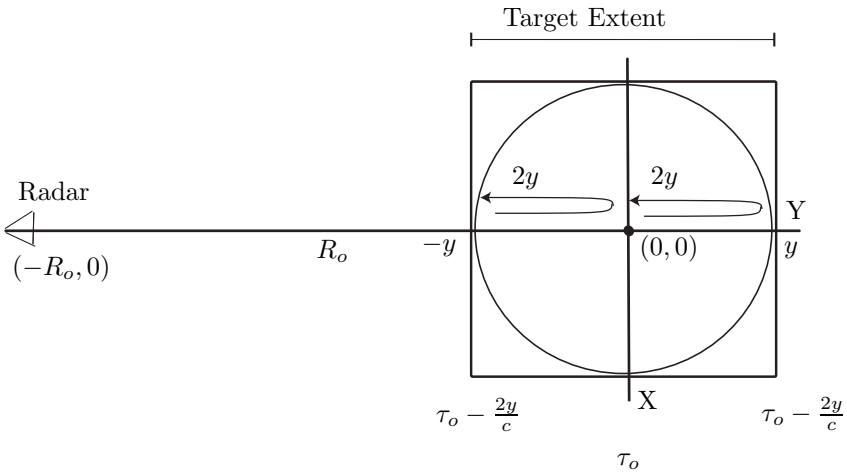

Figure A.1: Downrange spatial extent is referenced to the measurement area center. Since, the radar is monostatic the signal must traverse the radar to target path twice. Therefore, the downrange extents are defined based on the 2-way propagation referenced to the measurement area center.

where A is a scaling factor accounting for gains and losses due to antenna, radar, spherical spreading, and propagation path. The target reflectivity, $g(y)$, is a real or complex value. The return signal's magnitude and phase relates the signal energy reflected from individual target region points and the corresponding signal phase change. The signal delay, Eqn. (A.3) and Eqn. (A.4), is based on round-trip propagation from a single point within the target extent, whose temporal distance is described by, $\tau_o + \tau(y)$. This delay is the propagation time to the measurement center, τ_o, summed with the measurement center to the downrange target location propagation time, τ_y. These relationships are defined as

$$\tau_o = 2\frac{y_o}{c} \tag{A.5}$$

and

$$\tau(y) = 2\frac{y}{c}, \tag{A.6}$$

where c is the speed of light and y_o is the spatial distance downrange from the radar to the measurement center. However, multiple scatterers existing in a real measurement environment require *coherent* integration in the downrange and cross-range directions [12]. Therefore, to account for this integration, Eqn. (A.3) is written as,

$$s_b(t) = A\mathbf{Re}\left\{\int_{-y}^{y} g(y)\, e^{j\omega_o[t-\tau_o-\tau(y)]} b[t-\tau_o-\tau(y)]\, dy\right\}, \tag{A.7}$$

where $\pm\ y$ describes the spatial distance across the downrange extent. In order to determine the delay time in Eqn. (A.4), the downrange extent propagation time and the pulse delay must be considered. Since the delays are referenced to the measurement center, the return signal is described on a time interval of

$$\tau_o - \frac{\tau(y)}{2} - \frac{\tau_b}{2} \leq t \leq \tau_o + \frac{\tau(y)}{2} + \frac{\tau_b}{2}. \tag{A.8}$$

From the delay interval, Eqn. (A.8), it is desired to have a small pulse width, τ_b. If $\tau_b \ll \tau(y)$, then τ_b becomes negligible and the time interval defines the measurement area's downrange extent. Therefore, downrange target locations are identified within this extent.

Appendix B. Far-Field Approximation

As an electromagnetic wave propagates isotropically, the spatial distance, h, across the target extent decreases as the propagation distance, r, increases. This difference, h, is determined from the electromagnetic wave's propagation characteristics.

$$\vec{E} \quad = \quad \vec{p}Ae^{\left(-j\vec{k}\cdot\vec{r}\right)} \tag{B.1}$$

is a basic wave equation where $\vec{p}$ is the electric field polarization vector, A is the magnitude $\propto \frac{V}{m}$, $\vec{k}$ is the propagation vector, and $\vec{r}$ is the radar to reflection point vector [1]. The exponential term, $\left(-j\vec{k}\cdot\vec{r}\right)$, provides phase information for the wave. Assuming both vectors are aligned in the same direction, the dot product results in vector magnitude scalar multiplication, kr (where k is the wave number describing the wave phase relative to wavelength, $k = \frac{2\pi}{\lambda}$, and wavelength, $\lambda = \frac{c}{f}$, f is frequency, and c is the speed of light). Using the geometry of Fig. B.1, the distance h is calculated as,

$$h \simeq \frac{d^2}{8r} \ , \tag{B.2}$$

where d is the target extent [13]. Notice, for $r \to \infty$, $h \to 0$ and the wave becomes planar across the target extent, Fig. B.2. Since planar waves are not practical with real measurements, a target extent phase tolerance is defined for a far-field approximation. The far-field approximation is defined by the acceptable phase tolerance considered as a negligible target extent phase variance. An arbitrary, but commonly used target extent phase tolerance is $\frac{\pi}{8}$ [13]. Setting $kh \ = \ \frac{\pi}{8}$ and solving for the required far-field RCS measurement distance, r, in Eqn. (B.2),

$$r \quad = \quad 2\frac{d^2}{\lambda} \ . \tag{B.3}$$

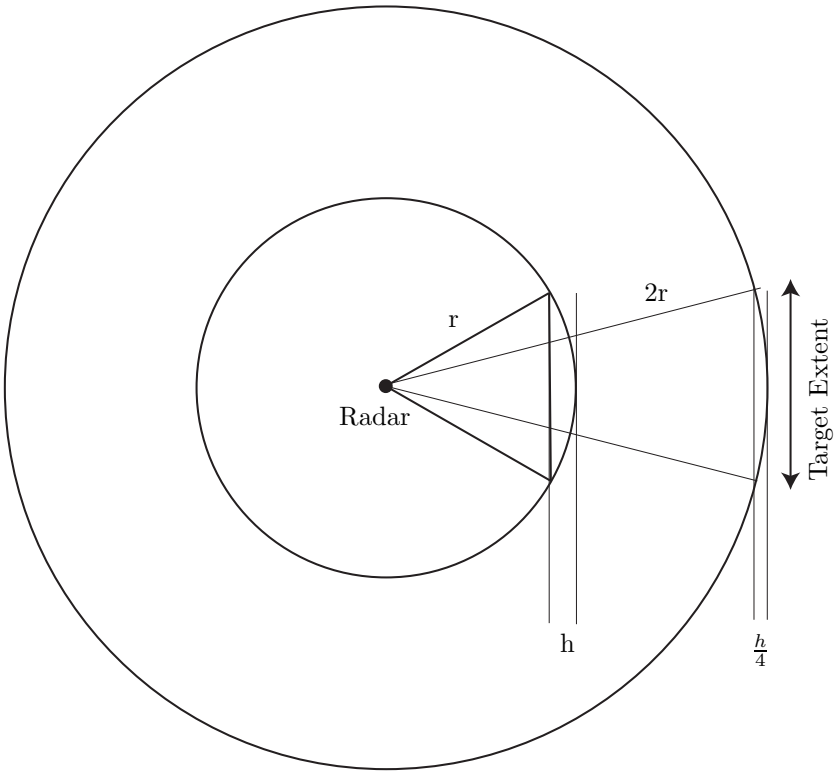

Figure B.1: The far-field approximation is arbitrary and dependent upon the target extent phase difference tolerable for a specific application. As an electromagnetic wave propagates the phase variance, kh, across the target extent decreases as the propagation radius, r, increases.

At this measurement distance the FF approximations are made. First the propagating waves are assumed planar, Fig. B.2. Therefore, every point on the wave front is in phase and strike the target extent at the same time. Additionally, as $r \to \infty$ the separation angle between the target extents, as seen by the radar, become very small. Therefore, the small angle approximation can also be made, where, $\cos\theta = 1$ and $\sin\theta = \theta$. This becomes critical for larger targets, Appendix C. As scattering center separation increases, the required propagation radius increases to achieve the same phase separation.

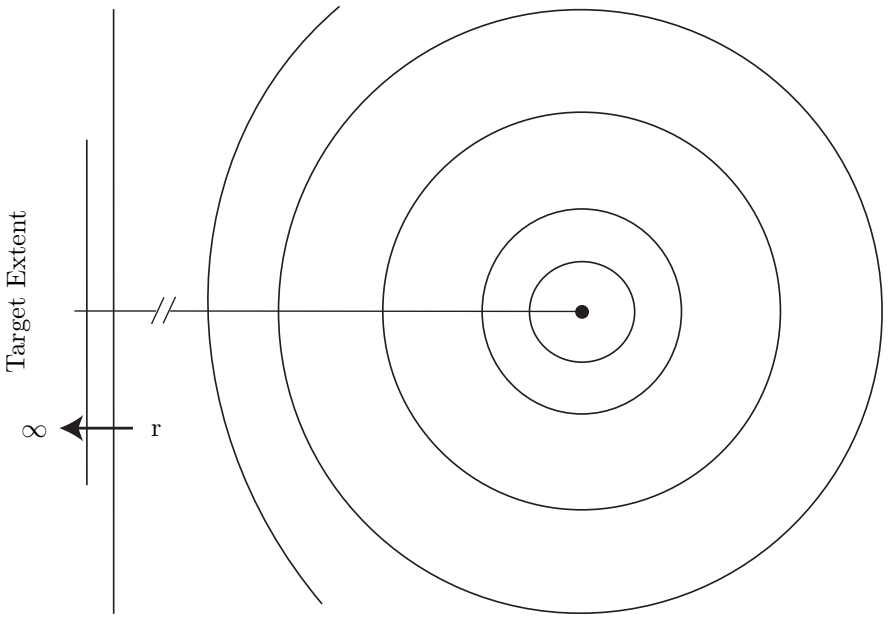

Figure B.2: The far-field approximation is based on the propagating wave being locally planar, where locally defines the spherical arc extent illuminating the target. Therefore, every point on this wave front is considered in phase.

Appendix C. Coherence

Multiple signals propagating from different locations cause a phase delay between waves equivalent to kr, where $k = \frac{2\pi}{\lambda}$ is the wave number and r is the distance separating the scattering center and the target location, Fig. C.1. Therefore, summing these signals noncoherently, neglecting the electromagnetic field's phase term,

$$\vec{E} = \vec{p}Ae^{\left(-j\vec{k}\cdot\vec{r}\right)} , \tag{C.1}$$

where A is the electromagnetic field's amplitude proportional to $\frac{V}{m}$, accounts only for the RCS magnitudes. However, signals out of phase interfere constructively and destructively depending upon the phase difference. Constructive interference results in a combined magnitude greater than any individual signal contribution at the same point in time. Similarly, destructive interference results in a magnitude lower than the strongest contributing signal. An example, Fig. C.2, takes two identical sine waves, $s1$ and $s2$, and sums them coherently, $Csum$, when $s2$ is shifted by 30^o. A noncoherenct sum, assuming the signals are in phase, $NCsum$, results significant magnitude and phase differences. Additionally, a shift approaching π results in purely destructive interference and the magnitude is zero. Therefore, the determination to sum signals coherently or noncoherently would depend upon the application and the tolerance defining the FF approximation, Appendix B.

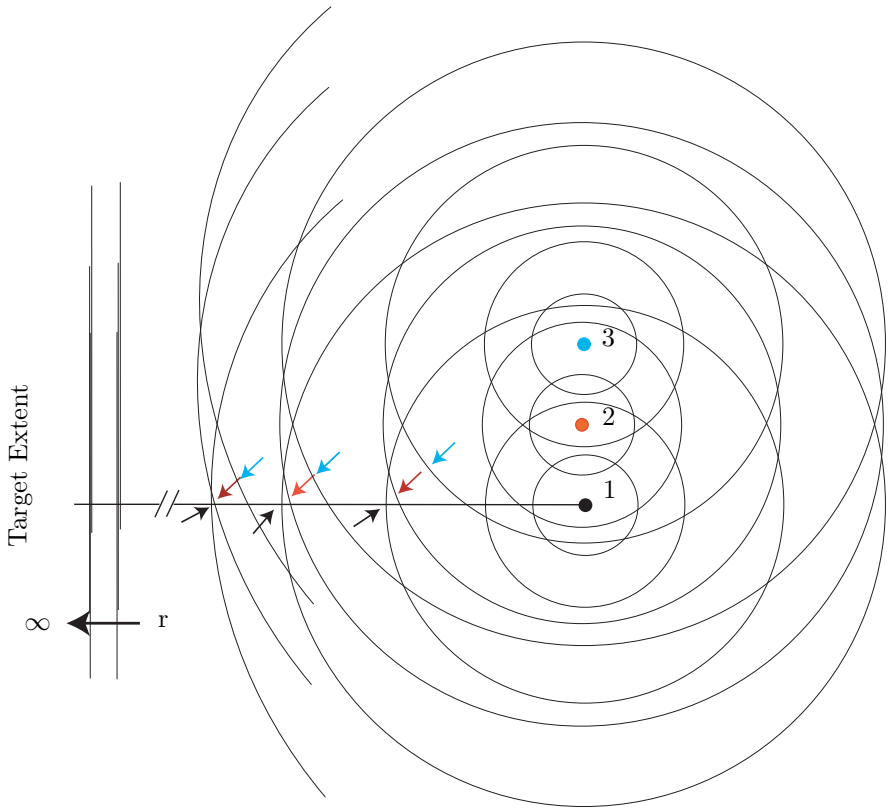

Figure C.1: Point scatterers radiate isotropically and reach far-field requirements within a minimal propagation radius. Although for group scatterers, a separation between scatterers requirers a increase in propagation radius to achieve a zero phase variation. The separation in phase indicated by the arrows decreases as the wave fronts propagate toward infinity and at infinity the phase difference is zero.

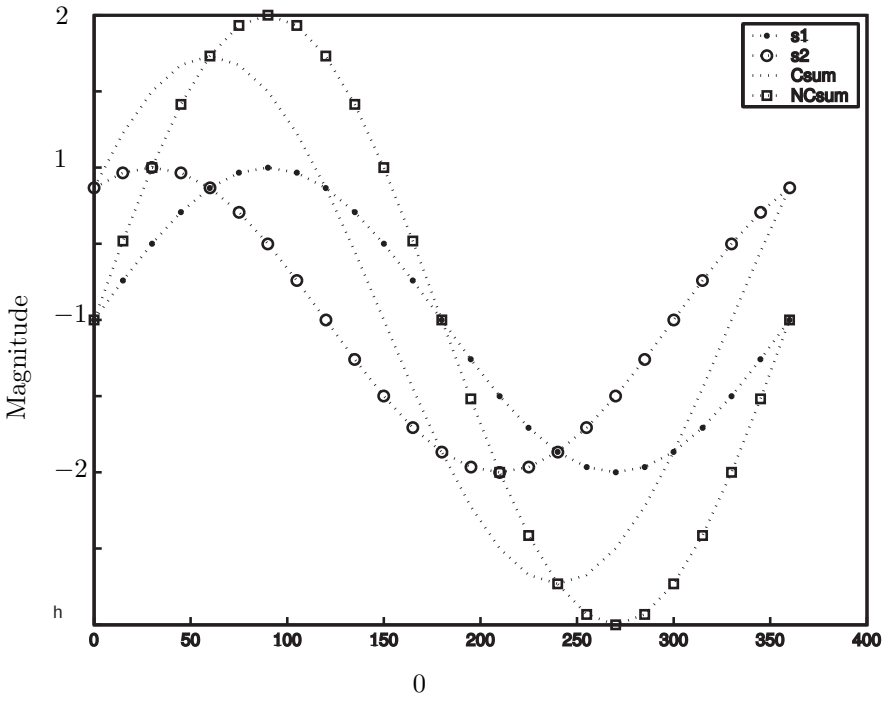

Figure C.2: Contributions from the propagation of multiple reflections in the same direction results in the sum of those signals. Two signals having equal magnitude and a 30^o phase difference interfere constructively and destructively. Coherently summing utilizes the relative phases ($Csum$). Notice the constructive and destructive nature over a period of interaction. Non-coherent summing assumes equal phases ($NCsum$). Therefore, the resulting signal amplitude is twice the amplitude of s1. NCsum has a different magnitude but it also has a different phase than the coherent sum.

Appendix D. In-phase and Quadrature RCS

A transmitted radar signal described by,

$$s(t) \quad = \quad b(t)\cos(w_o t) \ , \tag{D.1}$$

where $\cos(w_o t)$ represents a continuous wave signal operating at a carrier frequency, w_o, that is pulse modulated by $b(t)$ (an envelope function with a time interval defining the signal pulse width). The transmitted signal strikes an object and propagates back to the radar. The signal is processed by the radar, as depicted in Fig. D.1. The received signal,

$$s_b(t) \quad = \quad Ab\left[t-\tau_o-\tau(y)\right]\mathbf{Re}\left\{g(y)\,e^{j\omega_o[t-\tau_o-\tau(y)]}\right\} \ , \tag{D.2}$$

is the transmitted signal, Eqn. (D.1), scaled and delayed by $[\tau_o+\tau(y)]$ (the propagation times to the measurement center and downrange extent referenced to the measurement center, respectively). Mixing the signal with the in-phase carrier term, $\mathbf{Re}\ \left[e^{j\omega_o(t-\tau_o)}\right]$, and utilizing the fact that $\mathbf{Re}\left(e^{j\theta}\right)$ retains only the cosine term,

$$\vec{s}_{bI}(t) \quad = \quad A\int_{-y}^{y} g(y)\cos(\alpha)\cos(\beta)\,b(\alpha)\,dy \ , \tag{D.3}$$

where $\alpha \ = \ \omega_o\left[t-\tau_o-\tau(y)\right]$ and $\beta \ = \ \omega_o\left[t-\tau_o\right]$. Utilizing a trigonometric identity[1] , Eqn. (D.3) becomes,

$$\vec{s}_{bI}(t) \quad = \quad \frac{A}{2}\mathbf{Re}\int_{-y}^{y} g(y)\cos(\alpha-\beta)\,b(\alpha)\,\delta y \ + \ \frac{A}{2}\mathbf{Re}\int_{-y}^{y} g(y)\cos(\alpha+\beta)\,b(\alpha)\,\delta y \ . \tag{D.4}$$

[1] $\cos(A)\cos(B)=\frac{1}{2}\left[\cos(A-B)+cos(A+B)\right]$

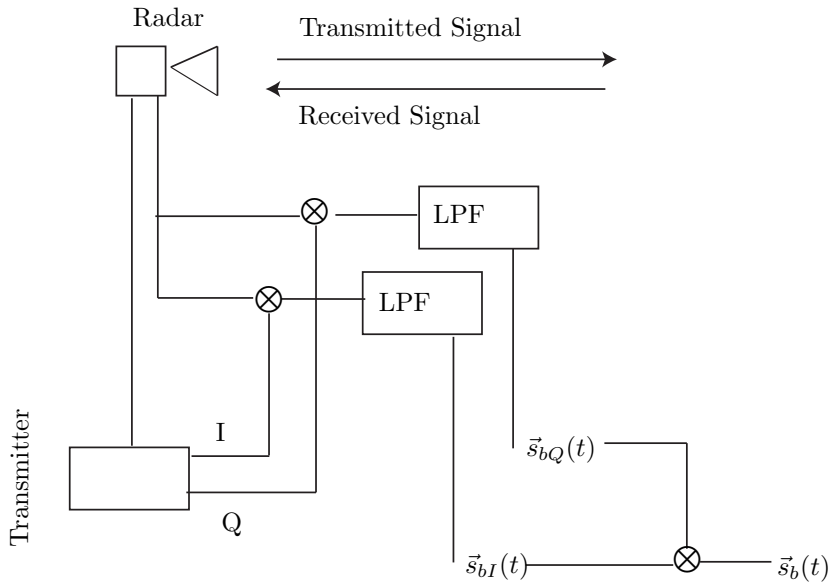

Figure D.1: A radar transmits a signal and receives a signal reflected from a target. The transmitter also separately transmits the In-phase and Quadrature, (IQ), reference signals to separate mixers and are mixed with the return signal. The return signal IQ portions are filtered out separately by the low pass filter and recombined to form the full return signal.

In complex form Eqn. (D.4) is written as,

$$\vec{s}_{bI}(t) = \frac{A}{2}\mathbf{Re}\int_{-y}^{y} g(y)\, e^{[j\omega_o(\alpha-\beta)]} b(\alpha)\, \delta y + \frac{A}{2}\mathbf{Re}\int_{-y}^{y} g(y)\, e^{[j\omega_o(\alpha+\beta)]} b(\alpha)\, \delta\ y\ . \quad \text{(D.5)}$$

Recognizing that $\alpha - \beta = -\omega_o \tau(y)$ and $\alpha + \beta = -\omega_o [2t - 2\tau_o - \tau(y)]$, the summation term is centered on twice the carrier frequency. Therefore, when the signal is passed through a low pass filter this term is filtered out and Eqn. (D.5) is written as,

$$\vec{s}_{bI}(t) = \frac{A}{2}\mathbf{Re}\int_{-y}^{y} g(y)\, e^{[j\omega_o(\alpha-\beta)]} b(\alpha)\, \delta y\ . \quad \text{(D.6)}$$

A similar process is used to show that the mixed and filtered quadrature term is written as,

$$\vec{s}_{bQ}(t) = \frac{A}{2}\mathbf{Im}\int_{-y}^{y} g(y)\, e^{[j\omega_o(\alpha-\beta)]} b(\alpha)\, \delta y. \quad \text{(D.7)}$$

The final equation after mixing, filtering, recombining the in-phase and quadrature terms, and changing the integration limits, with respect to the pulse width, results in,

$$\vec{s}_b\left(t+\tau_o\right) \quad = \quad \frac{A}{2}\int_{\frac{-\tau_p}{2}}^{\frac{\tau_p}{2}} g\left(y\right) e^{\left(-j\omega_o\tau\right)} b\left(t-\tau\right)\delta\tau \ . \tag{D.8}$$

This signal represents the returned sample for one frequency sweep and one azimuth. RCS measurements require multiple process iterations to perform data post processing.

Appendix E. Radar Gain

Large target Radar Cross-Section (RCS) measurements in compact ranges require very wide beamwidths to avoid more than a half-power drop in gain across a target's extent [27]. This beamwidth is calculated based on the illumination distance, R_o, that captures the full cross-range target extent throughout its rotation, Fig. E. The Half-Power BeamWidth (HPBW) is approximated using,

$$\Psi = 0.88\frac{\lambda}{d}\ rad, \tag{E.1}$$

where d is the aperture dimension and λ is the wavelength [24]. As a result, a decrease in beam width, requires a decrease in the aperture's electrical size, $\frac{\lambda}{d}$. Therefore, either the frequency (where $f = \frac{c}{\lambda}$ and c is the speed of light) or aperture size must decrease in order to increase the beamwidth. Since the frequency band is dependent upon the RCS measurement application, it is considered a fixed value. Therefore, the aperture's dimension, parallel to the measurement plane, must decrease to increase the beamwidth. Increasing the beamwidth spreads the energy concentration over a larger surface area and the decrease in aperture size decreases the capture area for the reflected energy. For a rectangular aperture the gain is approximated by,

$$G = 4\pi\frac{A_{eff}}{\lambda^2}\ , \tag{E.2}$$

where A_{eff} is the aperture's effective capture area. The effective aperture area is smaller than the physical aperture area due to losses within the aperture [2]. Therefore, as the aperture area decreases the gain decreases.

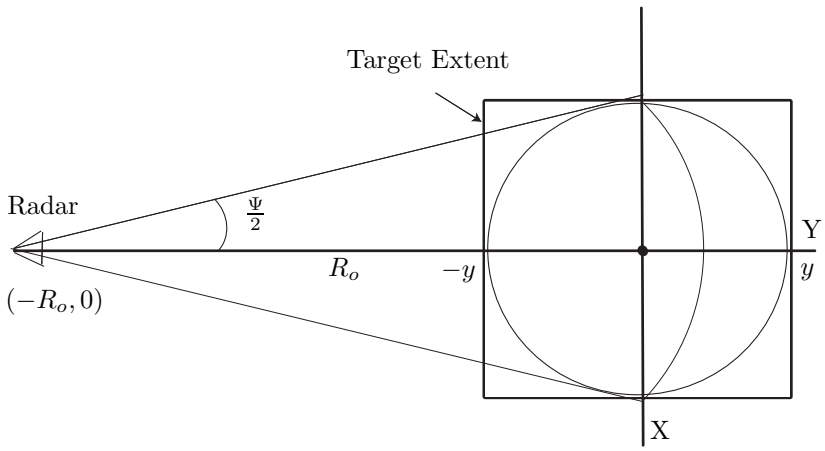

Figure E.1: Geometry for RCS measurement radar aperture design: For large target RCS measurements, it is desired to have a half power beam width equivalent or less than the target extent. This requires a very wide fan beam.

Appendix F. Cross-Range and Downrange Extents

The k-space polar to rectangular geometric conversion affects the cross-range and downrange imaging extents [12]. The chosen rectangular interpolation geometry establishes boundaries which can nullify data collected outside the rectangular grid. Using a completely inscribed rectangular grid, Fig. F.1, the frequency and azimuth extremum are no longer used for interpolation. Therefore, the effective bandwidth, B^{eff}, exists on an interval defined by the lowest and highest frequencies bounded by the rectangular grid. The maximum frequency is determined from the intersecting k_y and k_x maximum coordinates bounded by the rectangular grid. The maximum k-space rectangular grid coordinates are calculated using,

$$k_{ymax}^{eff} = \frac{4\pi f_{max}^{eff}}{c} \cos\left(\frac{\Theta}{2}\right) \tag{F.1}$$

and

$$k_{xmax}^{eff} = \frac{4\pi f_{min}^{eff}}{c} \sin\left(\frac{\Theta}{2}\right) \tag{F.2}$$

where c is the speed of light, f_{max}^{eff} and f_{min}^{eff} are the highest and lowest effective frequencies and $\frac{\Theta}{2}$ is the half angle traversed by the aperture. The rectangular grid's maximum frequency is calculated by combining Eqn. (F.1) and

$$\vec{r} = \frac{2\pi f}{c} \sin(\theta)\, \vec{k_x} + \frac{2\pi f}{c} \cos(\theta)\, \vec{k_y} \; . \tag{F.3}$$

from Section. 2.3, where $\vec{k_y}$ and $\vec{k_x}$ are the cartesian propagation vectors and whose effective magnitudes, limited by the rectangular geometries, are k_x^{eff} and k_y^{eff}. Solving for f, where $f = f_{max}^{eff}$, when $\frac{\Theta}{2} = 0$,

$$f_{max}^{eff} = \frac{k_{ymax}^{eff} c}{4\pi} \; . \tag{F.4}$$

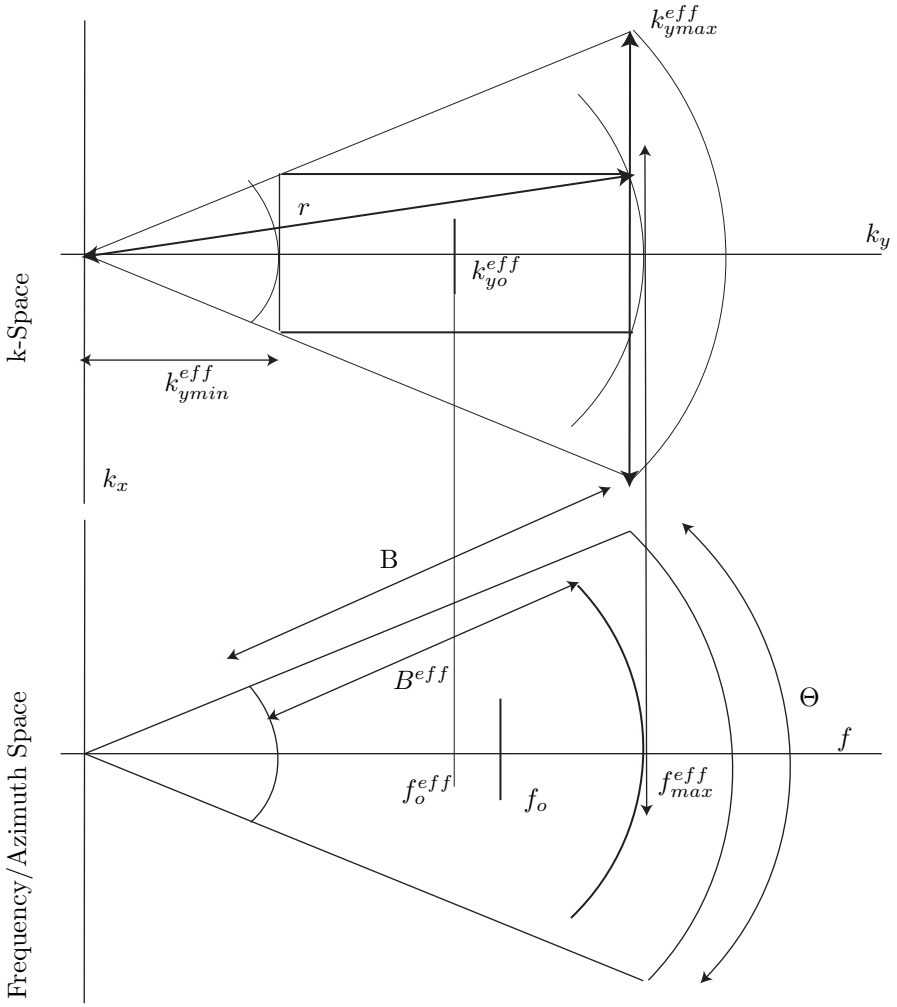

Figure F.1: The cross-range and downrange extents are dependent upon the resampled increments in effective bandwidth and aperture limited by the k-space rectangular grid inscribed in the frequency/azimuth space keystone.

Since the minimum frequency, f_{min}, remained unchanged, the rectangular grid's effective bandwidth is defined by $B^{eff} = f_{max}^{eff} - f_{min}$, with an effective center frequency, $f_o^{eff} = f_{min} + \frac{B^{eff}}{2}$. The downrange extent and cross-range extents in k-space are [12],

$$k_y^{eff} = 4\pi \frac{B^{eff}}{c} \ \left(m^{-1}\right) \tag{F.5}$$

and

$$k_x^{eff} \quad = \quad 2r \tan \frac{\Theta}{2} \ \left(m^{-1}\right) \tag{F.6}$$

where r is the magnitude of Eqn. (F.3) and $\frac{\Theta}{2}$ is the angle of maximum cross-range extent at the effective center frequency, Fig. F. These spatial domain maximum extents are calculated from k-space extents by [12],

$$D_y \quad = \quad 2\pi \frac{N_y}{\Delta k_y^{eff}} \tag{F.7}$$

and

$$D_x \quad = \quad 2\pi \frac{N_x}{\Delta k_x^{eff}} \ . \tag{F.8}$$

Appendix G. Phase

A sampling rate phase progression study is necessary to avoid aliasing in Inverse Synthetic Aperture Radar (ISAR) images. This aliasing induces ISAR imageable downrange and cross-range extent limitations. These extents are related to phase progression though wavenumber, $k = \frac{2\pi}{\lambda}$. The wavelength, $\lambda = \frac{c}{f}$ (where f is frequency and c is the speed of light), defines the propagation distance required for an electromagnetic wave to propagate through a 2π cycle. Also, the phase reference at the target's rotation center and the target's downrange extent, $2y$, described in Section 2.1.2, determine the required electromagnetic wave's propagation distance. Therefore, the maximum two-way propagation is twice the target's downrange extent from its rotation center, Fig. G.1. Therefore, the number of cycles in the propagation distance is, $N_c = 2yk$. According to Nyquist at least two samples per cycle are needed to accurately represent a sine wave, resulting in a minimum sample number, $N = 2N_c$. However, the sampling application may require more than the minimum sample number. Therefore, a phase tolerance, P_t is established and the total frequency samples required are,

$$N = \frac{4\pi y}{\lambda P_t}. \tag{G.1}$$

As an example, a $45' \; x \; 60'$ aircraft illuminated at 18 GHz would result in an electromagnetic wave propagating downrange through approximately 549 cycles from rotation center to the downrange extent, Fig. G.1. Therefore, satisfying the minimum Nyquist criteria, $P_t = \pi$, requires approximately 1100 samples. Overlaying frequency samples and resultant extents show the target extent can not be imaged if the Nyquist criteria is not met, Fig. G.2. However, as sampling rates are increased the downrange extent increases and the aircraft is completely imageable without aliasing, Fig. G.3. Additionally, if a smaller phase tolerance is desired then more samples are required to image the same downrange extent. Similarly, this process is applied to the cross-range extent. However, the cross-range extent is dependent upon the azimuthal increment.

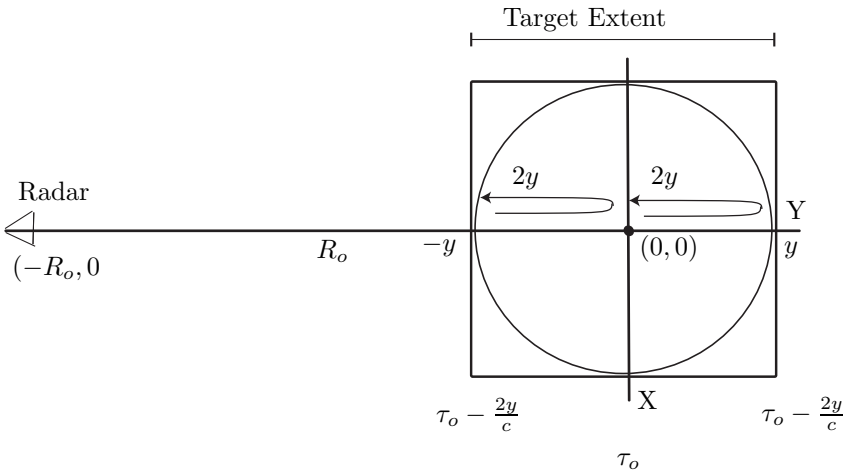

Figure G.1: Downrange spatial extent is referenced to the target's rotation center. Since, the radar is monstatic, the signal must traverse the radar to target path twice. Therefore, the downrange extents are defined based on the 2-way propagation referenced to the rotation center.

Nyquist testing in the cross-range extent requires a propagating phase study dependent upon change in illumination distance, Δr, through each azimuthal increment, $\Delta\theta$, Fig. G.4. By calculating Δr for each initial location within the target's spatial extent and its azimuthally dependent incremental location. The spatial propagation relationship with k is used to determine the cycles per sample. Since each azimuthal increment results in a different Δr, the maximum Δr for each scattering center over its azimuthal rotation, Θ, determines its Nyquist limit. From the geometry of Fig. G.4, r is calculated from the scattering center's downrange and cross-range locations, Y and X , respectively, at each azimuthal increment, and $r = \sqrt{Y^2 + X^2}$. Therefore, $N_c = 2k\Delta r_{max}$ for each scattering center location rotated over the full azimuth (Θ) incremented by θ. The Nyquist

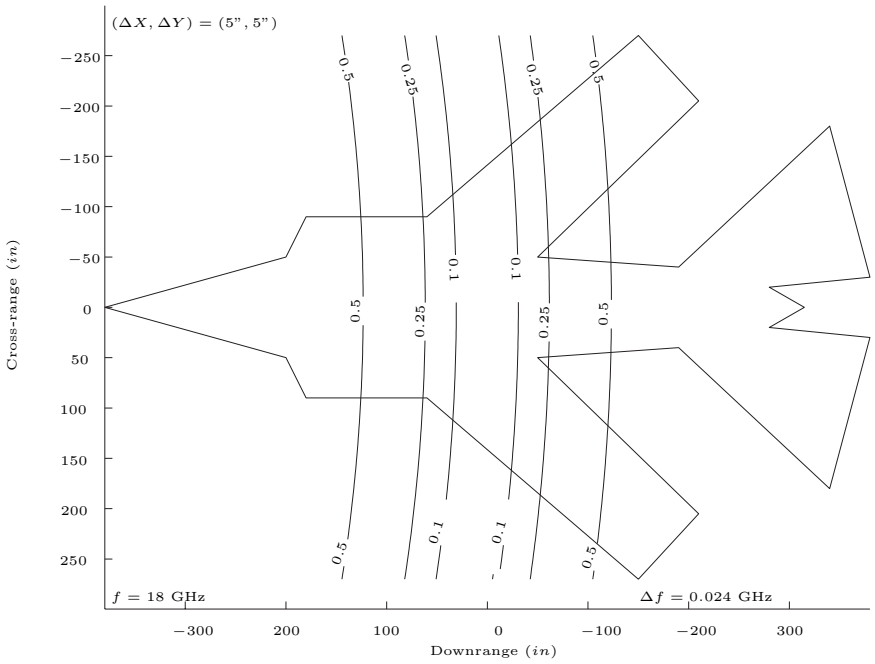

Figure G.2: Nyquist sampling determines the downrange imageable extent without aliasing. Therefore, the number of cycles per frequency sample can not exceed 0.5. The contours represent cycles per 0.024 GHz frequency increment at a max frequency, $f = 18$ GHz. Since, the 0.5 contours do not circumscribe the entire target, this example is not sampled finely enough to satisfy the Nyquist criteria over the full aircraft extent.

criteria requires, $N = 2N_c$ and if a smaller phase tolerance is required,

$$N = \frac{4\pi\Delta r_{max}}{\lambda P_t} . \tag{G.2}$$

Similar to the frequency example, contour overlays onto the target's spatial extent indicate the imageable limitations for under sampled data, Fig. G.5. As the sampling is increased the imageable extent is increased until the target extents fall within the contours representing the desired phase tolerance, Fig. G.6. In order to meet the Nyquist sampling requirements, both frequency and azimuth must be sampled finely enough to avoid aliasing in ISAR images. Therefore, overlaying the frequency and azimuth contour plots show the imageable boundaries, which avoid aliasing, Fig. G.7.

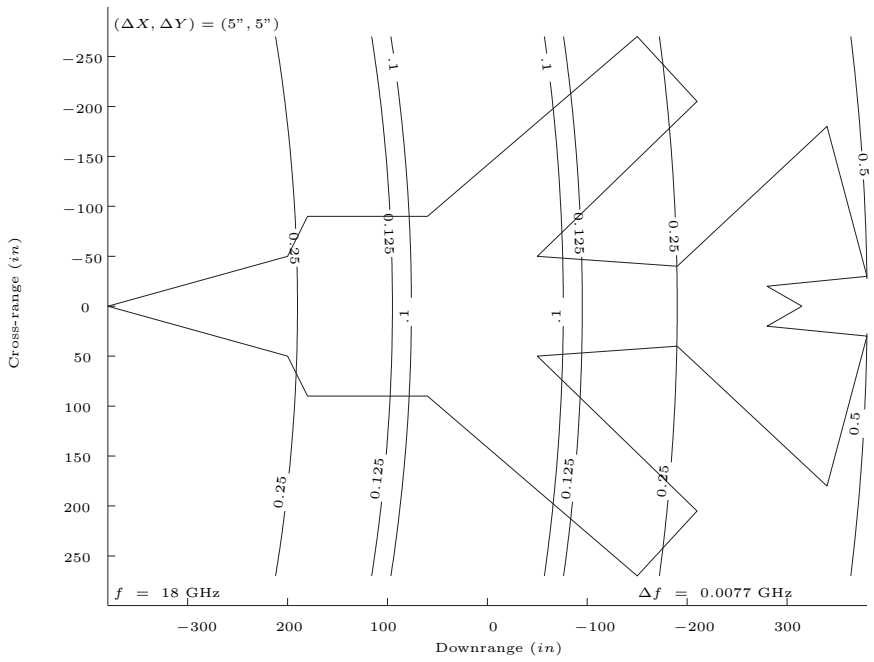

Figure G.3: Nyquist sampling determines the downrange imageable extent without aliasing. Therefore, the number of cycles per frequency sample can not exceed 0.5. The contours represent cycles per 0.0077 GHz frequency increment at a max frequency, $f = 18$ GHz. Since the contours fully circumscribe the target this example is sampled finely enough to satisfy the Nyquist criteria over the full aircraft extent.

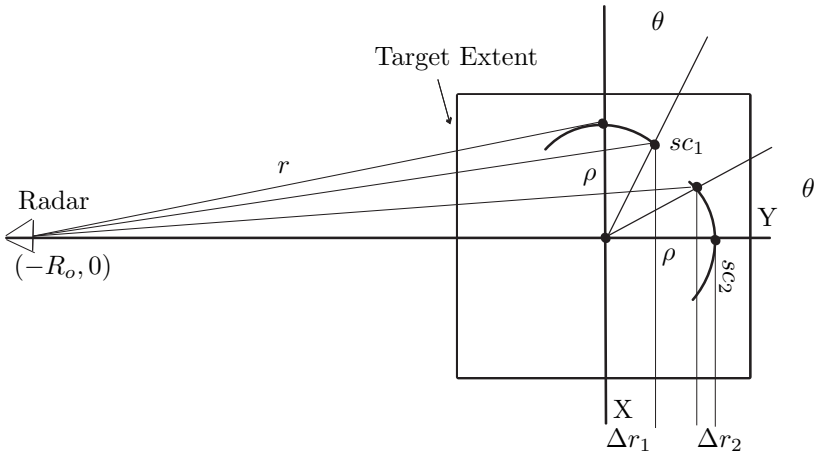

Figure G.4: The target's rotational geometry is described by isolating a single target reflection point, scattering center. Rotating through azimuthal increments, θ, each scattering center exhibits different changes in propagation distance, Δr, dependent upon the spatial locations and azimuthal increments.

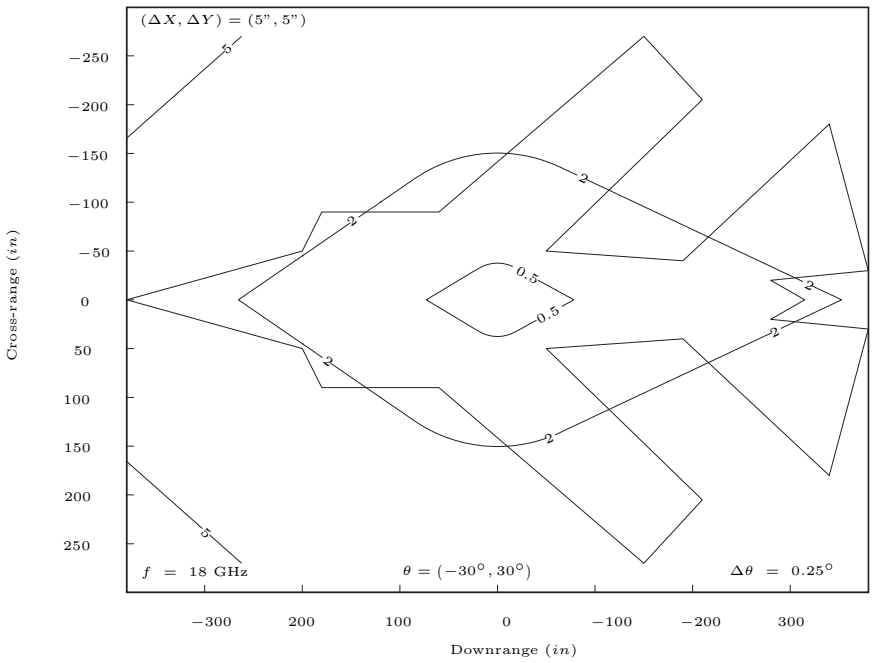

Figure G.5: Nyquist sampling requirements are dependent upon scattering center spatial location, rotation azimuth, and frequency. Fixing frequency and defining the azimuth and azimuth increment, contours are plotted which identify the cycle maximums a scattering center traverses through that aperture. In order to meet Nyquist requirements the scattering center does not exceed more than 0.5 cycles per azimuthal increment. Since the 0.5 contour does not fully circumscribe the target, this example is not sampled finely enough to satisfy the Nyquist criteria over the full aircraft extent.

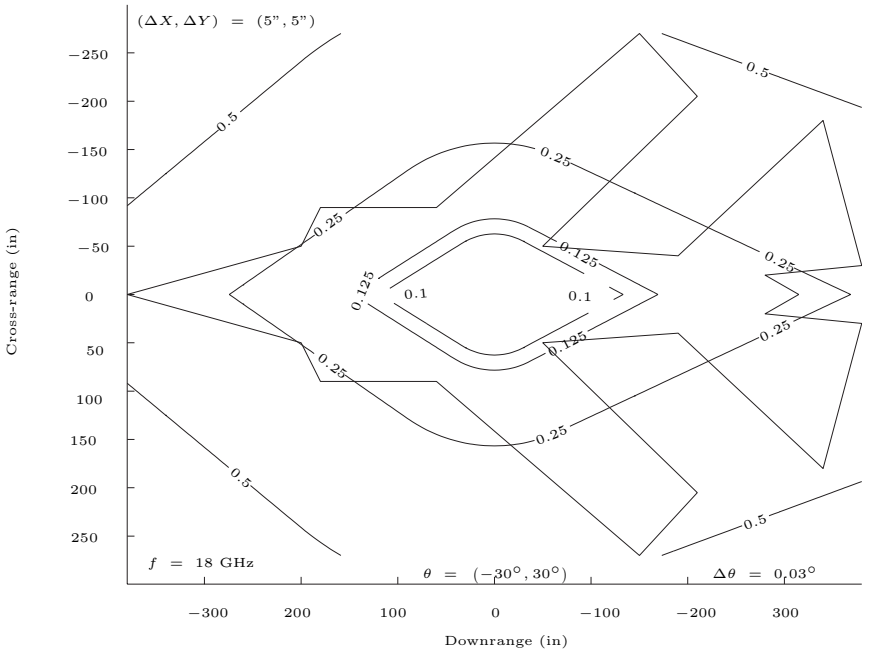

Figure G.6: Nyquist sampling requirements are dependent upon scattering center spatial location, rotation azimuth, and frequency. Fixing frequency and defining the azimuth and azimuth increment, contours are plotted which identify the cycle maximums a scattering center traverses through that aperture. In order to meet Nyquist requirements the scattering center does not exceed more than 0.5 cycles per azimuthal increment. Since the 0.5 contour fully circumscribes the target, this example is sampled finely enough to satisfy the Nyquist criteria over the full aircraft extent.

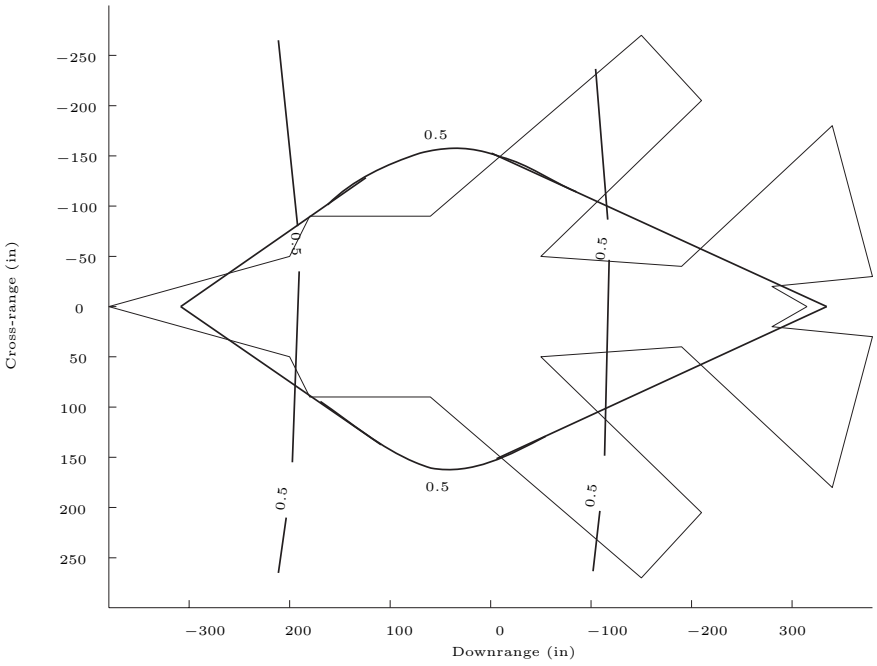

Figure G.7: Overlaying the frequency and azimuth sampling contours identifies the maximum imageable target boundaries without aliasing.

Bibliography

1. Balanis C. *Advanced Engineering Electromagnetics*. Wiley, 1989.

2. Balanis C. *Antenna Theory Analysis and Design* (second Edition). New York: Wiley, 1997.

3. Bhalla R. and Ling H. "Near-Field Signature Prediction Using Far-Field Scattering Centers Extracted From the Shooting and Bouncing Ray Technique," *IEEE Antennas and Propagation*, *48*:337–338 (2000).

4. Bhatia A., Vasistha P., and Shejwar R. "On the Estimation of Far-Field RCS from Monostatic Near-Field Data." *Proceedings of the 2003 Antennas Measurement Techniques Association (AMTA) Symposium*. 258–262. October 2003.

5. Brandwood D. *Fourier Transforms in Radar and Signal Processing*. Norwood, MA: Artech, 2003.

6. Brown W. and Fredricks R. "Range Doppler Imaging with Motion Through Resolution Cells." *IEEE Transactions on Aerospace and Electronic Systems*. 98–102. January 1969.

7. Chang D.-C. and Tsai M.-C. "Far Field RCS Prediction By Near Field RCS Measurement." *Proceedings of the IEEE Antennas And Propagation Society International Symposium*. 106–109, Vol. 1. June 2002.

8. Chen V. and Ling H. "Near-Field Signature Prediction Using Far-Field Scattering Centers Extracted From the Shooting and Bouncing Ray Technique," *IEEE Antennas and Propagation*, *16*:337–338 (2000).

9. Choi I. and Kim H. "Two-Dimensional Evolutionary Programming-Based CLEAN," *IEEE Aerospace and Electronic Systems*, *39*:373–382 (2003).

10. Giray M. and Mishra S. "A Hybrid Approach for 2-D RCS Imaging." *Antennas and Propagation Society International Symposium, 1992. AP-S. 1992 Digest. Held in Conjunction with: URSI Radio Science Meeting and Nuclear EMP Meeting., IEEE*. 1126–1129. July 1992.

11. Hurst M. and Mittra R. "Scattering Center Analysis Via Prony's Method," *IEEE Antennas and Propagation [legacy, pre - 1988]*, *35*:986–988 (1987).

12. Jakowatz C. V., Wahl D. E., Eichel P. H., Ghiglia D. C., and Thompson P. A. *Spotlight-Mode Synthetic Aperture Radar: A Signal Processing Approach*. Norwell, MA: Kluwer Academic Publishers, 1996.

13. Knott E. F., Shaeffer J. F., and T.Tuley M. *Radar Cross Section* (second Edition). Norwood, Ma: Artech House, 1993.

14. LaHaie I., LeBaron E., and Burns J. "Far Field Radar Cross-Section (RCS) Predictions from Planar Near Field Measurements." *Proceedings of the 1992 Digest. Held in Conjunction with: URSI Radio Science Meeting and Nuclear EMP Meeting*. 1542–1545, Vol 3. July 1992.

15. LaHaie I., Ricoy M., LeBaron E., Burns J., Stach J., and Fliss G. *Spherical Near Field to Far Field Radar Cross Section Transformation Techniques: Phase II*. Final Technical Report, P.O. Box 134001, Ann Arbor, MI 48113-4001: ERIM, February 1997.

16. Lamb B. "Approximation of Far-Field Illumination Conditions Through Transformation of Near-Field RCS Data." *Radar Conference, 1991., Proceedings of the 1991 IEEE National*. 152–155. Mar 1991.

17. Li H.-J. and Huang G.-T. "Evaluation Of Far-Field Pattern From Near-Field Measurement Using A Near-Field Imaging Technique," *IEEE Antennas and Propagation Society Symposium 1991 Digest*, *3*:1462–1465 (1991).

18. Li Q., Rothwell E., Chen K., Nyquist D., Ross J., and Bebermeyer R. "Determination of Radar Target Scattering Center Transfer Functions from Measured Data," *IEEE Antennas and Propagation Society Symposium 1994. AP-S. Digest*, *3*:2006–2009 (1994).

19. Marr R., Hansen T., Lammers U., McGahan R., and Tanigawa T. "Far-field Bistatic RCS From Near-field Measurements." *Proceedings of the 2003 Antennas Measurement Techniques Association (AMTA) Symposium*. 388–393. October 2003.

20. Melin J. "Measuring Radar Cross Section at Short Distance." *IEEE Transactions on Antennas and Propagation*. 991–996. August 1987.

21. Mensa D. L. *High Resolution Radar Cross-Section Imaging*. Norwood, MA: Artech, 1991.

22. Oppenheim A. and Schafer R. *Discrete-Time Signal Processing*. Englewood Cliffs, NJ: Prentice Hall, 1989.

23. Ricoy M., LeBaron E., Aberegg K., and Fliss G. *Spherical Near Field to Far Field Radar Cross Section Transformation Techniques: Phase III*. Final Technical Report, P.O. Box 134001, Ann Arbor, MI 48113-4001: ERIM, May 1997.

24. Skolnik M. I. *Introduction to Radar Systems* (Third Edition). 1221 Avenue of the Americas, New York, NY 10020: McGraw-Hill, Inc., 2001. ISBN: 0072909803.

25. Tsao J. and Steinberg B. "Reduction of Sidelobe and Speckle Artifacts in Microwave Imaging: The ClEAN Technique." *IEEE Transaction on Antennas and Propagation*. 543–556. April 1988.

26. Wehner D. R. *High-Resolution Radar* (Second Edition). Norwood, MA: Artech House, 1995.

27. Welsh B. M. and Link J. N. "Accuracy Criteria for Radar Cross Section Measurements of Targets Consisting of Multiple Independent Scatterers." *IEEE Transactions on Antennas and Propagation*. 1587–1593. November 1988.

REPORT DOCUMENTATION PAGE

Form Approved
OMB No. 074-0188

1. REPORT DATE *(DD-MM-YYYY)*	2. REPORT TYPE	3. DATES COVERED *(From – To)*
08-06-2004	**Master's Thesis**	Jan 2004 – Jun 2004

4. TITLE AND SUBTITLE

UTILIZING NEAR-FIELD MEASUREMENTS TO CHARACTERIZE FAR-FIELD RADAR SIGNATURES

5a. CONTRACT NUMBER

5b. GRANT NUMBER

5c. PROGRAM ELEMENT NUMBER

6. AUTHOR(S)

Watkins, John R., Captain, USAF

5d. PROJECT NUMBER
If funded, enter ENR #

5e. TASK NUMBER

5f. WORK UNIT NUMBER

7. PERFORMING ORGANIZATION NAMES(S) AND ADDRESS(S)

Air Force Institute of Technology
Graduate School of Engineering and Management (AFIT/EN)
2950 Hobson Way
WPAFB OH 45433-7765

8. PERFORMING ORGANIZATION REPORT NUMBER

AFIT/GE/ENG/04-24

9. SPONSORING/MONITORING AGENCY NAME(S) AND ADDRESS(ES)

ASC/YFAAE
Attn: Mr. Carl Conklin
2725 C Street
WPAFB OH 45433-7424 DSN: 785-9683

10. SPONSOR/MONITOR'S ACRONYM(S)

11. SPONSOR/MONITOR'S REPORT NUMBER(S)

12. DISTRIBUTION/AVAILABILITY STATEMENT

APPROVED FOR PUBLIC RELEASE; DISTRIBUTION UNLIMITED.

13. SUPPLEMENTARY NOTES

14. ABSTRACT

The increased need for stealth aircraft requires an on-site Far-Field (FF) Radar Cross-Section (RCS) measurement process. Conducting these measurements in on-site Near-Field (NF) monostatic facilities results in significant savings for manufacturers and acquisition programs. However, NF measurements are not directly extended to a FF RCS. Therefore, a large target Near-Field to Far-Field Transformation (NFFFT) is needed for RCS measurements. One approach requires an Inverse Synthetic Aperture Radar (ISAR) process to create accurate scattering maps.

The focus of this work is the development of accurate NF scattering maps generated by a monostatic ISAR process. As a first look, the process is isolated to a simulated environment to avoid the uncontrollable effects of real measurement environments. The simulation begins with a NF Synthetic Target Generator which approximates a target using scattering centers illuminated by spherical electromagnetic waves to approximating NF scattering. The resulting NF In-phase and Quadrature data is used in a 'Trapezoidal' ISAR process to create spatially distorted images that are accurately corrected within the ISAR process resolution using a newly developed NF correction. The resulting spatially accurate ISAR images do not complete the NFFFT. However, accurate scattering maps are essential for process development.

15. SUBJECT TERMS

Far-Field, Near-Field, Radar Cross Section, Monostatic, Inverse Synthetic Aperture Radar, Near-Field to Far-Field Transformation, Synthetic Target Generator, Near-Field Correction, Trapezoidal Inverse Synthetic Aperture Radar, Scattering Centers, Spherical Wave Approximation, Isotropic Radiators.

16. SECURITY CLASSIFICATION OF:			17. LIMITATION OF ABSTRACT	18. NUMBER OF PAGES	19a. NAME OF RESPONSIBLE PERSON
REPORT	ABSTRACT	c. THIS PAGE			Maj. Todd Hale
U	U	U	UU	112	19b. TELEPHONE NUMBER *(Include area code)* (937) 255-3636 ext 4369

Standard Form 298 (Rev: 8-98)
Prescribed by ANSI Std. Z39-18